CERN-AB-2007-064-ABP

CARE-Conf-07-007-HHH
CARE/ELAN document-2007-006
EUROTEV-Report-2007-060

20 August 2007

Joint CARE-ELAN, CARE-HHH-APD, and EUROTEV-WP3 Workshop on

Electron Cloud Clearing

- Electron Cloud Effects and Technological Consequences

"ECL2"

CERN, Geneva, Switzerland, 1 - 2 March, 2007

PROCEEDINGS

Editors :
F. Caspers
W. Scandale
D. Schulte
F. Zimmermann

GENEVA
2007

Abstract

This report contains the Proceedings of the joint CARE-HHH-APD, CARE-ELAN, and EUROTEV-WP3 Mini-Workshop on 'Electron Cloud Clearing — Electron Cloud and Technical Consequences', "ECL2", held at CERN in Geneva, Switzerland, 1-2 March 2007[1)].

The ECL2 workshop explored novel technological remedies against electron-cloud formation in an accelerator beam pipe. A primary motivation for the workshop was the expected harmful electron-cloud effects in the upgraded LHC injectors and in future linear colliders, as well as recent beam observations in operating facilities like ANKA, CESR, KEKB, RHIC, and SPS. The solutions discussed at ECL2 included enamel-based clearing electrodes, slotted vacuum chambers, NEG coating, and grooves. Several of the proposed cures were assessed in terms of their clearing efficiency and the associated beam impedance. The workshop also reviewed new simulation tools like the 3D electron-ion build-up 'Faktor2', modeling assumptions, analytical calculations, beam experiments, and laboratory measurements. Several open questions could be identified. The workshop reinforced inter-laboratory collaboration on electron-cloud suppression, and it concluded with a discussion of the next steps to be taken.

[1)] The ECL2 workshop was sponsored and supported by the European Community-Research Infrastructure Activity under the FP6 "Structuring the European Research Area" programme (CARE, contract number RII3-CT-2003-506395; and EUROTeV, contract number RIDS-011899).

Preface

The joint CARE-HHH-APD, CARE-ELAN, and EUROTEV-WP3 Mini-Workshop on 'Electron Cloud Clearing — Electron Cloud and Technical Consequences', "ECL2", was held at CERN, Geneva, Switzerland, from 1 to 2 March 2007 (see http://care-hhh.web.cern.ch/CARE-HHH/ECL2/). The workshop was sponsored by the three European accelerator networks CARE-HHH-APD, CARE-ELAN, and EUROTEV-WP3. It was attended by 35 participants from 16 institutions in Europe, Asia, and the Americas, including 3 representatives from the German enamel industry. The workshop scope and programme had been drafted by the ECL2 Organizing Committee, comprising Fritz Caspers (CERN), Oleg Malyshev (ASTeV/Cockcroft), Mauro Pivi (SLAC), Walter Scandale (CERN), Daniel Schulte (CERN), Rainer Wanzenberg (DESY), and Frank Zimmermann (CERN).

ECL2 addressed all methods for suppressing the electron build up, such as reducing the primary or secondary electron yields, modifying the electron dynamics, and changing some beam parameters. The workshop did not discuss beam instabilities or beam stabilization in presence of an electron cloud.

The workshop started with a tour of the CERN NEG coating facility. The presentations and discussions were structured in eight (six) sessions spanning over the full two days. A primary topic of the ECL2 workshop was the quasi-continuous electron cloud clearing electrode, based on an insulating enamel layer. Further topics discussed were other types of clearing electrodes, NEG coating, grooved surfaces, slotted beam pipes, clearing efficiencies, beam measurements, and impedance issues.

The main motivation for the ECL2 workshop was the recent realization that the electron cloud may constitute a serious limitation for upgraded LHC injectors, in particular for the PS2 and the enhanced SPS. For the latter two, Marco Venturini presented updated electron-cloud build-up predictions from Miguel Furman, considering various LHC injector upgrade scenarios, while Giovanni Rumolo discussed the implications for beam stability in the new SPS. Proceeding in parallel to the CARE-HHH LHC upgrade studies, the electron-cloud task force in Work Package 3 of the EUROTeV linear-collider network is developing solutions against electron cloud build up for ILC and CLIC. A new simulation code, Faktor2, was written for this purpose by Warner Bruns. Warner has also identified a novel and intriguing solution for suppressing the electron cloud, namely a slotted or gridded beam pipe.

When comparing the potential of different solutions, a number of aspects need to be considered, such as modeling, prototypes, beam experiments, suppression efficiency, impedance, vacuum issues, implications and cost. An attempt was made to cover all these points at the ECL2 workshop.

At ECL2, the optimum configuration of clearing electrodes was investigated, their impedance for different layouts estimated by two independent programs, GdfidL and HFSS, respectively, and the clearing efficiency explored in simulations. A traveling-wave resonant ring was assembled at CERN for testing an enamel chamber equipped with an electrode. Some of the relevant enamel properties, such as SEY and PEY, still need to be measured, but so far no fundamental problem has been found. Experience with different types of clearing electrodes at other accelerators like CERN AA, CERN EPA, CERN SPS and DAΦNE was surveyed.

Another novel idea, which was suggested by Fritz Caspers during the workshop, is the use of electretes, which are permanently charged or self-charging materials. Electretes might allow

for an in-situ upgrade of the LHC and the SPS. More "classical" techniques, previously proposed for suppressing electron build up, include coating with a thin TiZrV NEG layer or with TiN, and grooved surfaces. Some or all of these techniques are being vigorously tested experimentally with beam at SLAC, KEK, Cornell, ESRF, and CERN. Results and further plans from all these studies were presented at ECL2. The simulated beneficial effect of grooves was also discussed in presentations by Marco Venturini and Warner Bruns. An interesting observation was reported by Sara Casalbuoni from ANKA at FZ Karlsruhe, where the measured heat load in a cold superconducting in-vacuum undulator and the coincident pressure rise indicate the possible presence of an electron cloud at cold temperature and with an electron beam. Some clear signals for an electron cloud occurring with an electron beam are also seen at CESR.

Presentations by Ubaldo Iriso, Theo Demma, Oleg Malyshev, Gisela Pöplau, and Aleksandar Markovic, addressed simplified faster electron-cloud simulations, predictions of electron-instability simulations for an LHC injector upgrade, and the vacuum design of the ILC damping ring.

The discussion session focused on a number of open questions, related to (1) the proper modeling of the electron cloud, including the effect of the beam field on secondary and primary emission, the effect of an external magnetic field, the role of ions, the handling of grooves, and the validity of the assumed surface parameters; (2) enamel, in particular its secondary and primary emission yields, impedance, long-term stability, detailed studies of suppression efficiency, possibility of retrofitting an existing operational beam pipe with enamel coating; (3) other schemes, like air-baked copper, injection of radicals, and permanent electric fields in the form of electretes; (4) grooves, especially procedures for in-situ grooving; and (5) a comparison of NEG vs TiN coating, in view of long-term stability, self-activation, and heat. Arguments in favor of, or against, clearing electrodes and NEG coating were collected and compared.

Further information on the workshop can be accessed from its home web site,
http://care-hhh.web.cern.ch/CARE-HHH/ECL2/ .

The ECL2 workshop was organized in eight (six) plenary sessions, covering (1) overview and simulations, (2) technological solutions [I+II], (3) simulation code development, simulation results, and analytical treatments, (4) beam measurements [I+II], (5) impedance issues, and (6) studies, designs and plans. In addition, a tour of the CERN NEG coating laboratory for interested ECL2 participants took place on the evening of 28 February, prior to the workshop, under the expert guidance of Paolo Chiggiato.

The proceedings are structured according to the six plenary sessions:

- Session 1: Overview and Simulations
  (convener D. Schulte).
- Sessions 2: Technological Solutions I+II
  (conveners F. Caspers and M. Pivi).
- Session 3: Simulation Code Development, Simulation Results, and Analytical Treatments
  (convener M. Venturini).
- Sessions 4: Beam Measurements I+II
  (conveners W. Fischer and G. Arduini).
- Session 5: Impedance Issues
  (convener E. Jensen).
- Session 6: Studies, Designs and Plans
  (convener F. Zimmermann).

These proceedings have been published in paper and electronic form. The paper copy is in black and white; the electronic version contains colour pictures. Electronic copies can be retrieved through:
`http://care-hhh.web.cern.ch/CARE-HHH/ECL2/Proceedings`

The compilation of these proceedings would not have been possible without the help of the conveners and speakers. The organizational support by the workshop secretary Muriel Macchi is also gratefully acknowledged. In particular, we would like to thank all the participants for their stimulating contributions and lively discussions.

The ECL2 workshop was sponsored and supported by the European Community-Research Infrastructure Activity under the FP6 "Structuring the European Research Area" programme (CARE, contract number RII3-CT-2003-506395).

The ECL2 proceedings are dedicated to the memory of Francesco Ruggiero (1957-2007), who has been instrumental in setting up and directing the electron cloud research program at CERN.

Geneva, 17 August 2007

F. Caspers, W. Scandale, D. Schulte, F. Zimmermann

Contents

[1] A paper was not submitted to the proceedings. However, the slides presented are available in electronic form at *http://care-hhh.web.cern.ch/CARE-HHH/ECL2*.
[2] These results were presented by M. Venturini.

[1] A paper was not submitted to the proceedings. However, the slides presented are available in electronic form at *http://care-hhh.web.cern.ch/CARE-HHH/ECL2*.

[3] Slides presented during the discussion are available in electronic form at *http://care-hhh.web.cern.ch/CARE-HHH/ECL2*.

[3] Slides presented during the discussion are available in electronic form at *http://care-hhh.web.cern.ch/CARE-HHH/ECL2*.

ECLOUD in PS2, PS+, SPS+: AN UPDATE*

M. A. Furman,† Center for Beam Physics, Bldg. 71R0259, LBNL, CA 94720-8211, USA

Abstract

We present an update of our results for the electron-cloud build-up for several upgrades proposed for the LHC injectors. Specifically, we have re-examined our published results for the ecloud heat load [1] from the perspective of numerical convergence of the simulations vis-à-vis the integration time step Δt. We repeated most of the simulations with ever smaller values of Δt until we reached stable results, indicating numerical convergence; this was achieved at 200–500 slices per bunch, depending on the particular case. In all cases examined, the simulated heat load decreases monotonically, until the limit is reached, as Δt decreases in the range explored, hence the stable results are more favorable vis-à-vis the heat load than the previous ones. This is particularly true for a bunch spacing $t_b = 25$ ns.

SUMMARY AND RESULTS

All assumptions for the simulation, physical parameters and notation are described in [1], particularly Table I which we reproduce below. In this update we consider only the PS and SPS upgrades, not the LHC proper. We have not re-examined any cases with bunch spacing $t_b = 12.5$ ns. The only parameter that is varied here is the integration time step Δt; all other parameters remain as specified in [1]. In particular, we have examined the build-up of the ecloud only in a dipole bending magnet for each machine, at a magnetic field B corresponding to the specified beam energy E_b, for the first batch injected into an empty chamber (2 μs long, including the gap after the bunch train). We have not examined any other regions of the machine, nor any effects from the ecloud on the beam.

Figs. 1 and 2 show the approach to numerical convergence of the heat load for the PS50 and PS75, respectively, plotted as a function of peak SEY $\delta_{\max}$. Numerical convergence is clear at $N_k = 501$ for $t_b = 25$ ns, but is already apparent for $N_k = 201$ for $t_b = 50$ and 75 ns. Values of Δt are indicated for the largest value of N_k. For other values of N_k, Δt scales as $(N_k - 1)^{-1}$.

Fig. 3 shows a comparison of the heat load for the PS50, for copper vs. stainless steel chamber surface. The simulated results for copper are the same as those in Fig. 5 of Ref. 1, and were obtained with $N_k = 251$ kicks per bunch for $t_b = 25$ ns, and $N_k = 201$ for $t_b = 50$ ns (we did not verify that the copper results have converged). We recall that the labels "copper" and "stainless steel" refer here to a particular choice of model parameters we used for the secondary electron emission yield and emitted electron energy spectrum. Although these two sets of model parameters were extracted from various bench measurements, we do not know whether they correspond to the actual materials that are used, or will be used, in the actual vacuum chambers of the machines. Therefore, these secondary emission models would have to be validated by new measurements in order to confirm the clear advantage of copper over stainless steel seen in Fig. 3.

Fig. 4 shows the heat load, after convergence has been reached, for the cases PS50 and PS75. This should be compared with Fig. 4 of Ref. 1. Figs. 5, 6 and 7 present similar comparisons for various competing options considered for the SPS (to be compared with Figs. 6, 7 and 8 of Ref. 1, respectively). In general, there is no qualitative difference between the options except possibly at $t_b = 25$ ns.

DISCUSSION

In the range of values for the integration step size Δt we have explored ($\Delta t = (1 - 30) \times 10^{-11}$ s) we have seen that the simulated heat load decreases monotonically, until a limit is reached, as Δt decreases. We conclude that the previous results, while not accurate, at least had the value of representing an upper limit for the estimated heat load. The largest fractional decrease of the heat load is seen for $t_b = 25$ ns. The previously seen inverse relationship that the heat load has with the bunch spacing is maintained by the new results. In addition to the heat load, we have also computed other quantities such as electron density (global and close to the beam), ecloud average energy per electron, electron-wall impact energy, and electron flux at the chamber walls. A spreadsheet with all such results is available upon request.

ACKNOWLEDGMENTS

I am indebted to M. Venturini for presenting some of these results at the ECL2 workshop. I am grateful to F. Zimmermann for guidance and encouragement, and to NERSC for supercomputer support.

REFERENCES

[1] M. A. Furman, "ECLOUD in PS2, PS+, SPS+," Proc. CARE-HHH-APD Workshop *Towards a Roadmap for the Upgrade of the CERN and GSI Accelerator Complex* "LHC LUMI 2006," IFIC (Valencia, Spain), 16–20 October 2006, http://care-hhh.web.cern.ch/CARE-HHH/LUMI-06/default.html. Please look only at my publication in the proceedings; the preliminary results presented in my viewgraphs should not be taken into consideration.

* Work supported by the U.S. DOE under Contract No. DE-AC02-05CH11231 and by the US-LHC Accelerator Research Program (US-LARP).

† mafurman@lbl.gov

Table 1: Basic simulation input parameters.

Case	Our notation	E_b GeV	B T	(a, b) cm	N_b 10^{11}	t_b ns	(σ_x, σ_y) mm	σ_z cm	profile ...
PS2, 50 GeV extr.	PS50tb12p5	50	1.8	$(8, 4)$	2	12.5	$(1, 0.9)$	57.3	gauss.
	PS50tb25	50	1.8	$(8, 4)$	4	25	$(1, 0.9)$	93.5	gauss.
	PS50tb50	50	1.8	$(8, 4)$	5.4	50	$(1, 0.9)$	104	flat
	PS50tb75	50	1.8	$(8, 4)$	6.6	75	$(1, 0.9)$	104	flat
PS+, 75 GeV extr.	PS75tb12p5	75	2.7	$(8, 4)$	2	12.5	$(0.8, 0.8)$	50.5	gauss.
	PS75tb25	75	2.7	$(8, 4)$	4	25	$(0.8, 0.8)$	83.5	gauss.
	PS75tb50	75	2.7	$(8, 4)$	5.4	50	$(0.8, 0.8)$	92.3	flat
	PS75tb75	75	2.7	$(8, 4)$	6.6	75	$(0.8, 0.8)$	92.3	flat
SPS, 50 GeV inj.	SPS50tb12p5	50	0.225	$(7, 2.2)$	1.9	12.5	$(3.1, 1.6)$	14.3	gauss.
	SPS50tb25	50	0.225	$(7, 2.2)$	3.8	25	$(2.8, 1.6)$	23.4	gauss.
	SPS50tb50	50	0.225	$(7, 2.2)$	5.2	50	$(3, 1.6)$	26.1	flat
	SPS50tb75	50	0.225	$(7, 2.2)$	6.4	75	$(3, 1.6)$	26.1	flat
SPS, 75 GeV inj.	SPS75tb12p5	75	0.337	$(7, 2.2)$	1.9	12.5	$(2.4, 1.3)$	12.6	gauss.
	SPS75tb25	75	0.337	$(7, 2.2)$	3.8	25	$(2.1, 1.3)$	20.9	gauss.
	SPS75tb50	75	0.337	$(7, 2.2)$	5.2	50	$(2.3, 1.3)$	23.1	flat
	SPS75tb75	75	0.337	$(7, 2.2)$	6.4	75	$(2.3, 1.3)$	23.1	flat
SPS, 450 GeV extr.	SPS450tb12p5	450	2.025	$(7, 2.2)$	1.9	12.5	$(1.2, 0.9)$	12	gauss.
	SPS450tb25	450	2.025	$(7, 2.2)$	3.8	25	$(1, 0.5)$	12	gauss.
	SPS450tb50	450	2.025	$(7, 2.2)$	5.2	50	$(1, 0.5)$	15	flat
	SPS450tb75	450	2.025	$(7, 2.2)$	6.4	75	$(1, 0.5)$	15	flat
SPS+, 1 TeV extr.	SPS1000tb12p5	1000	4.5	$(6, 2)$	1.8	12.5	$(0.5, 0.4)$	12	gauss.
	SPS1000tb25	1000	4.5	$(6, 2)$	3.6	25	$(0.6, 0.4)$	12	gauss.
	SPS1000tb50	1000	4.5	$(6, 2)$	5.1	50	$(0.5, 0.4)$	15	flat
	SPS1000tb75	1000	4.5	$(6, 2)$	6.2	75	$(0.5, 0.4)$	15	flat
SPS+a, 50 GeV inj.	SPSpa50tb12p5	50	0.225	$(6, 2)$	1.9	12.5	$(3.1, 1.6)$	14.3	gauss.
	SPSpa50tb25	50	0.225	$(6, 2)$	3.8	25	$(2.8, 1.6)$	23.4	gauss.
	SPSpa50tb50	50	0.225	$(6, 2)$	5.2	50	$(3, 1.6)$	26.1	flat
	SPSpa50tb75	50	0.225	$(6, 2)$	6.4	75	$(3, 1.6)$	26.1	flat
SPS+b, 75 GeV inj.	SPSpb75tb12p5	75	0.337	$(6, 2)$	1.9	12.5	$(2.4, 1.3)$	12.6	gauss.
	SPSpb75tb25	75	0.337	$(6, 2)$	3.8	25	$(2.1, 1.3)$	20.9	gauss.
	SPSpb75tb50	75	0.337	$(6, 2)$	5.2	50	$(2.3, 1.3)$	23.1	flat
	SPSpb75tb75	75	0.337	$(6, 2)$	6.4	75	$(2.3, 1.3)$	23.1	flat
LHC nominal	LHCnom	7000	8.39	$(2.2, 1.8)$	1.15	25	$(0.3, 0.3)$	7.55	gauss.
LHC ultimate	LHCult	7000	8.39	$(2.2, 1.8)$	1.7	25	$(0.3, 0.3)$	7.55	gauss.
longer bunch	LHClb	7000	8.39	$(2.2, 1.8)$	6	75	$(0.3, 0.3)$	14.4	flat
longer bunch 2	LHClb2	7000	8.39	$(2.2, 1.8)$	4.9	50	$(0.3, 0.3)$	14.4	flat
same except gaussian	LHClb2g	7000	8.39	$(2.2, 1.8)$	4.9	50	$(0.3, 0.3)$	14.4	gauss.
shorter bunch	LHCsb	7000	8.39	$(2.2, 1.8)$	1.7	12.5	$(0.3, 0.3)$	3.78	gauss.

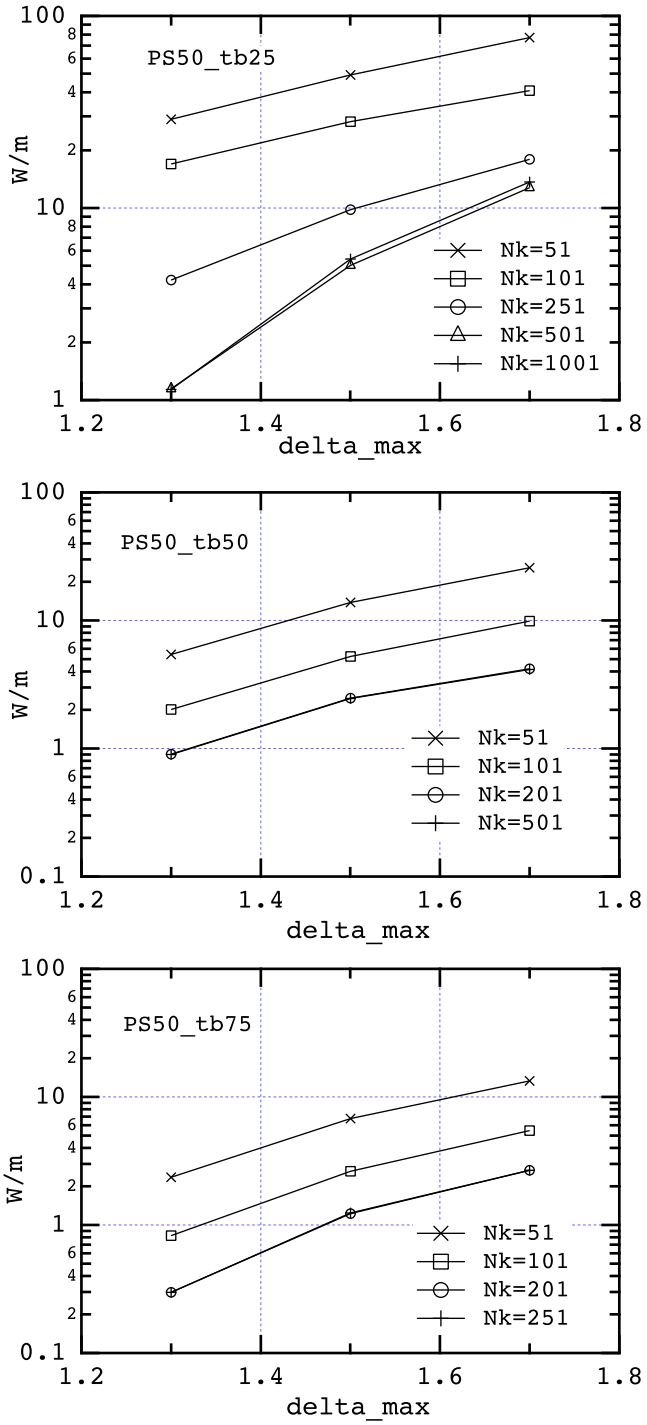

Figure 1: Simulated ecloud heat load vs. $\delta_{\max}$ for case PS50 ("PS2"), for $t_b = 25$ ns (top), $t_b = 50$ ns (center) and $t_b = 75$ ns (bottom), for various values of the number of kicks per bunch length N_k. For the highest value of N_k used, Δt has the values 1.56×10^{-11} s (top), 2.68×10^{-11} s (center) and 5.36×10^{-11} s (bottom).

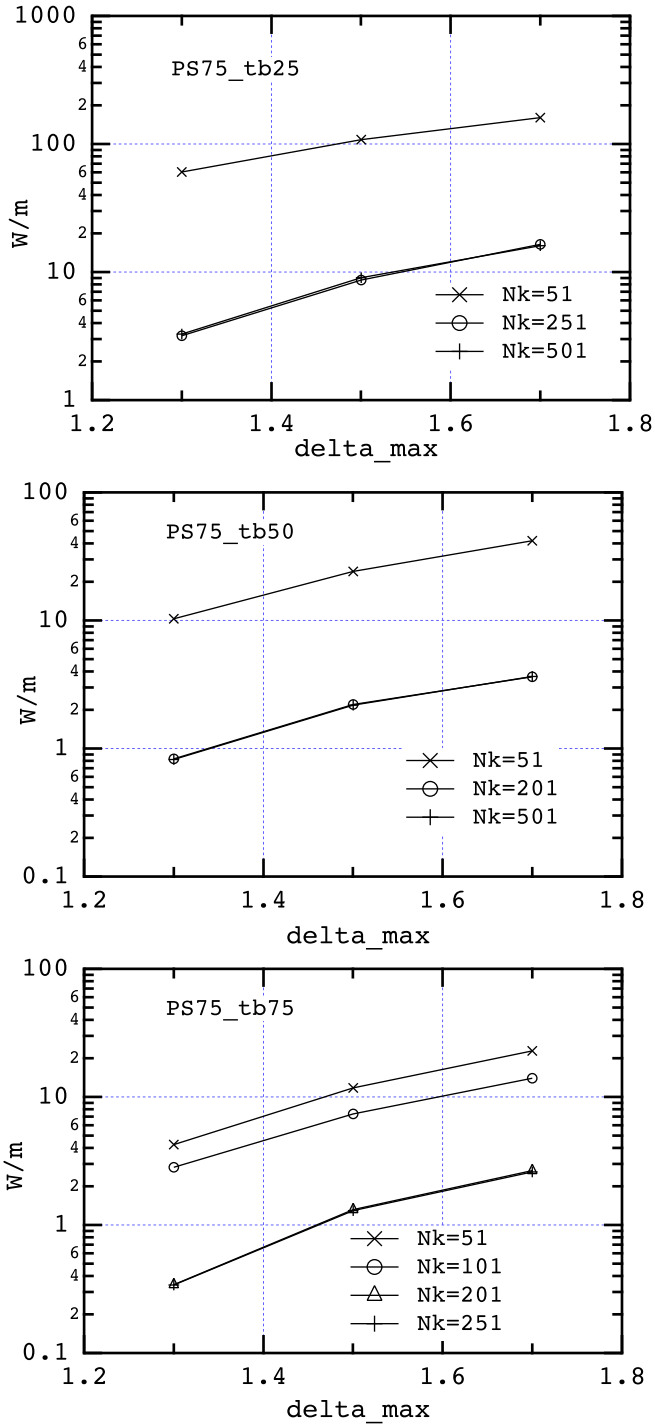

Figure 2: Simulated ecloud heat load vs. $\delta_{\max}$ for case PS75 ("PS+"), for $t_b = 25$ ns (top), $t_b = 50$ ns (center) and $t_b = 75$ ns (bottom), for various values of the number of kicks per bunch length N_k. For the highest value of N_k used, Δt has the values 2.79×10^{-11} s (top), 2.38×10^{-11} s (center) and 5.95×10^{-11} s (bottom).

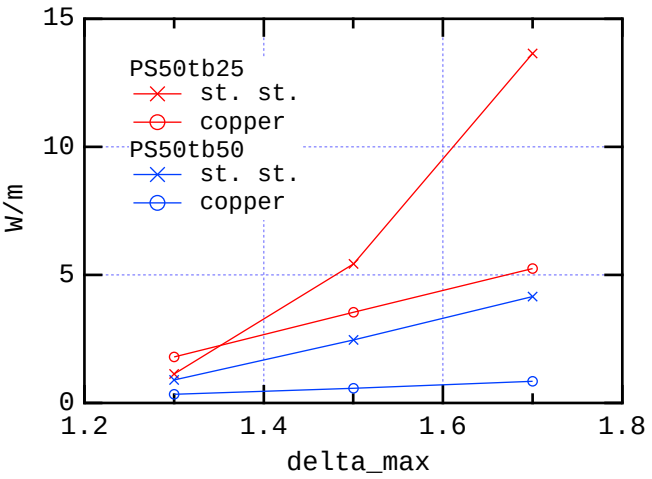

Figure 3: Simulated PS ecloud heat load vs. $\delta_{\max}$ for case PS50, for copper and stainless steel chamber. The basic difference in the calculation for the two cases is the secondary emission energy spectrum of the two metals.

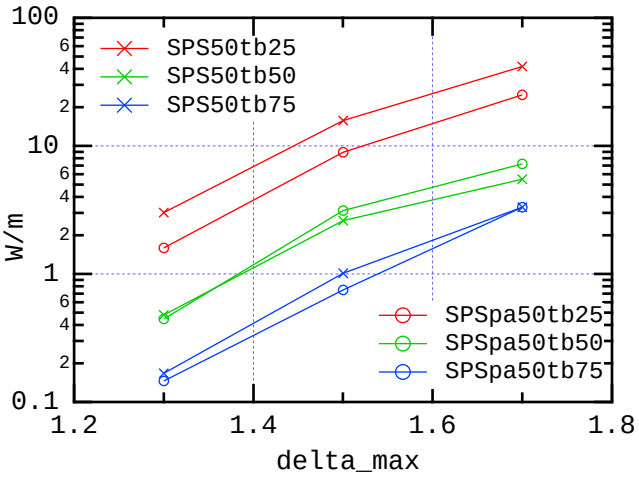

Figure 5: Simulated SPS ecloud heat load vs. $\delta_{\max}$ for cases SPS50 and SPSpa50. The only difference between the calculation for these two cases is the transverse chamber size (slightly smaller for the SPSpa50).

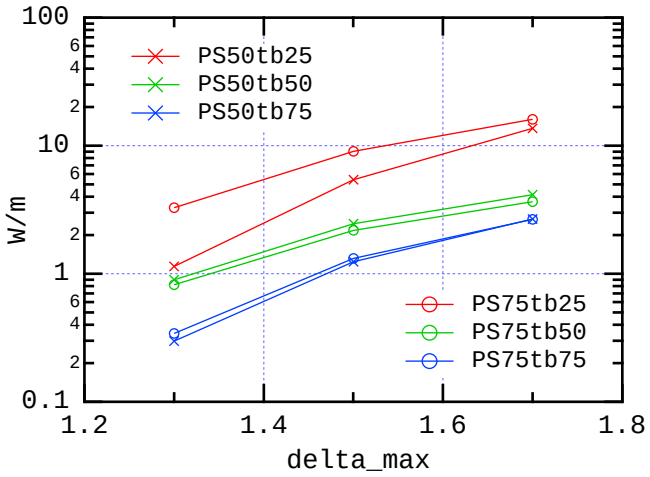

Figure 4: Simulated PS ecloud heat load vs. $\delta_{\max}$ for case PS50 and PS75 ("PS2" and "PS+" in "psplusetcparameters," respectively).

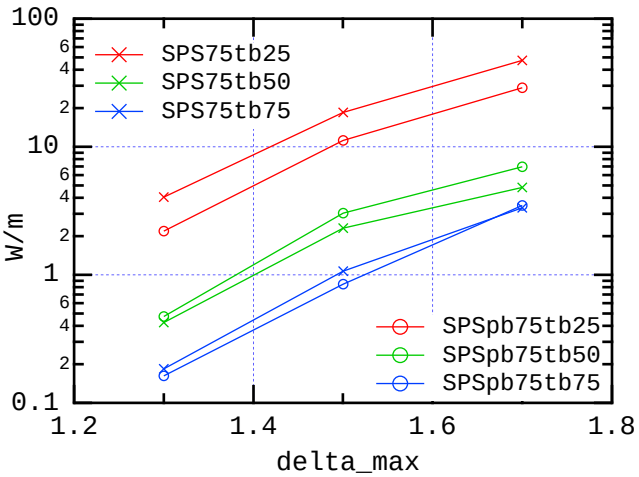

Figure 6: Simulated SPS ecloud heat load vs. $\delta_{\max}$ for cases SPS75 and SPSpb75. The only difference between the calculation for these two cases is the transverse chamber size (slightly smaller for the SPSpb75).

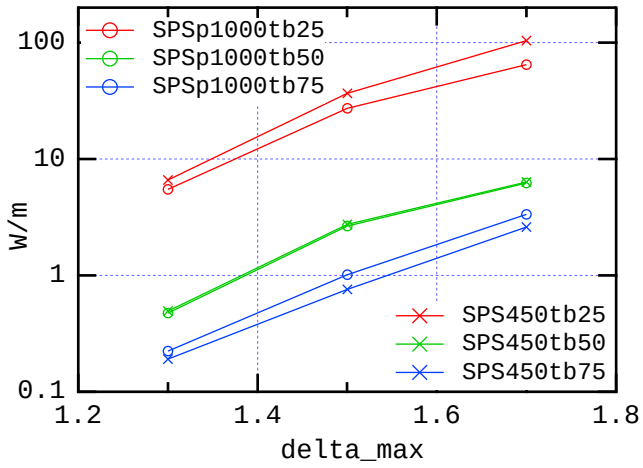

Figure 7: Simulated SPS ecloud heat load vs. $\delta_{\max}$ for $E_b = 450$ GeV and $E_b = 1$ TeV.

E-CLOUD BUILD-UP IN GROOVED CHAMBERS

M. Venturini*
LBNL, Berkeley CA 94720 , USA

Abstract

We simulate electron cloud build-up in a grooved vacuum chamber including the effect of space charge from the electrons. We identify conditions for e-cloud suppression and make contact with previous estimates of an effective secondary electron yield for grooved surfaces.

SUMMARY OF WORK

Corrugating the interior of a vacuum chamber with small grooves is one of the possible remedies currently investigated for suppressing the electron cloud accumulation in storage rings. Analytical and numerical modelling of the interaction of electrons with grooved surfaces have indicated the effectiveness of this technique and accelerator-based experiments to confirm these results are planned or already underway. Previous simulations [1, 2, 3] so far have generally aimed at determining an effective secondary electron yield (SEY) by considering a beam of monochromatic electrons (primary particles) impinging on the grooved surface and keeping track of the electrons (secondary particles) emerging from the groove regions – a setting typical of laboratory bench measurements where an effective SEY can easily be determined as a function of the energy of the primary electron beam. In the work described here we are interested in a direct characterization of the electron cloud build-up in the vacuum chamber of an operating accelerator in the presence of both the driving beam and space-charge from the electrons. This will be useful for a closer comparison between current e-cloud modelling and accelerator-based measurements.

We carried out our work by augmenting the current version of the code POSINST to include the option to follow the electron dynamics in the presence of grooves. Electron-surface collisions and secondary electron production following those collisions are modelled using the modules already built in POSINST [4]. At present we have a provision to simulate rectangular cross-section vacuum chambers with triangular grooves located on the top and bottom sides – closely reproducing the configuration a proposed e-cloud experiment at PEP-II. The steepness angle α of the triangular grooves as well their height (see Fig. 1) are input parameters controlled by the user. An option to include rounding of the groove tips has also been implemented. Space charge from the electrons is included in the model. However, at present the electric field lines are terminated on a hypothetical smooth surface immediately behind the grooves thus neglecting possible field enhancement by the groove tips.

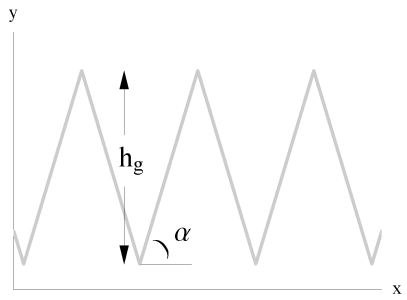

Figure 1: Triangular grooves (with sharp tips) are characterized by steepness angle α and height h_g.

We illustrate POSINST new features by showing an application to the ILC positron damping ring (DR), for which electron cloud is a very serious concern. There is wide consensus that the current baseline specifications for the ILC DRs can only be achieved if effective e-cloud suppression techniques can be developed beyond levels currently demonstrated. Failure of doing so could result in substantial increase in cost (*e.g.* the installation of an additional damping ring) or degradation of the collider performance [5].

Grooves reduce the effective SEY by increasing the probability that immediately after production secondary electrons may be rapidly reabsorbed through wall collisions and therefore prevented from contributing to multipacting. The effectiveness of the grooves strongly depends on the geometry. For triangular grooves the existence of a critical angle for effective suppression of the electron cloud can be clearly extracted from Fig. 2. The picture shows the maximum linear electron density accumulated during the single passage of a 111-positron bunch train through one of the ILC DR dipoles as a function of the triangular grooves steepness angle α. The bunch train is 0.68 μs long, for a 6.1 ns separation between bunches. The bunches have a population of 2×10^{10} and sizes $\sigma_x = 0.62$ mm, $\sigma_y = 8$ μm, $\sigma_z = 6$ mm (this is smaller than the current baseline value $\sigma_z = 9$ mm). The magnetic field in the dipoles is about 0.2 T. The calculation is for grooves height $h_g = 1$ mm and the model of SEY adopted was that of Al,

* mventurini@lbnl.gov

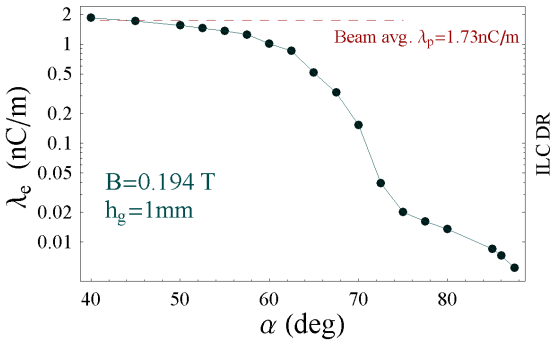

Figure 2: Maximum linear density of electrons accumulated during a passage of a train of positron bunches in a ILC damping ring dipole *vs.* steepness angle α of triangular grooves (with sharp edges). Al chamber with $\delta_{\max} = 1.75$.

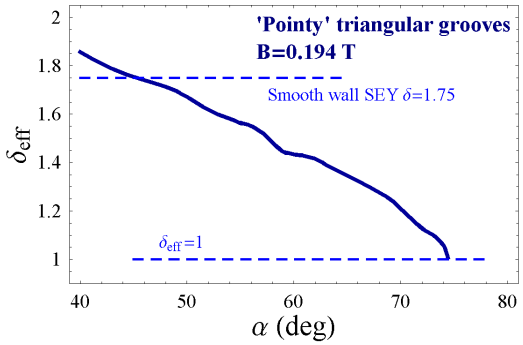

Figure 3: Effective SEY as a function of the steepness angle α as derived from the simulation of e-cloud build-up.

with maximum SEY set to $\delta_{\max} = 1.75$.

A drop in electron density by about two orders of magnitude compared to the smooth-chamber case is seen to occur for steepness angle α larger than $75°$. For shallower angles the electron accumulation is increasingly larger, approaching and in fact slightly overtaking the electron cloud density for a smooth surface when $\alpha < 45°$. This latter behavior is not implausible. It is a basic property of the model employed in the calculation that the SEY is minimum for electrons hitting the surface at a normal incidence. At a smaller α the grooves become ineffective at capturing the secondaries and the effective SEY may become larger if on average the primary electrons hit the surface off the local normal.

To make contact with previous studies we extracted an effective max SEY from our data by making comparison with the electron density we would obtain in a smooth chamber as we vary the value of $\delta_{\max}$ for the smooth surface. An effective yield corresponding to a given α is then defined as that $\delta_{\max}$ producing the same maximum e-cloud accumulation in a smooth chamber during the passage of the same train of positron bunches. The result is shown in Fig. 3 where the effective max. SEY is plotted as a function of the steepness angle α. The curve is reasonably smooth and again indicates $\alpha \simeq 75^o$ as the critical angle where the effective secondary yield crosses into values smaller than unity corresponding to effective electron cloud suppression.

Our results are substantially consistent with calculations reported in [1], where for the same groove geometry (and same maximum SEY for the smooth surfaces) an effective secondary yield as a function of energy is found to remain <1 for angles just above $\alpha \simeq 70°$. Both the present and Wang *et al.*'s findings are somewhat less pessimistic than those obtained by W. Bruns [3], which indicate that an angle $\alpha = 75°$ would still yield an effective SEY larger than unity; $\alpha = 75°$ was the largest steepness angle reported in [3] but a rough extrapolation from the data shown would appear to predict a noticeably larger critical angle for a SEY$<$1.

During discussions at the workshop it was mentioned that these discrepancies in the results could perhaps be ascribed to differences in the SEY model at low electron energies. While in the model used by W. Bruns $\delta(E)$ is unity at zero energy [6, 7] (and displays a local minimum at low energy) in the POSINST model (and possibly in L. Wang's calculations [1]), the same limit is $\delta(0) \simeq 0.5$ [4]. It is not unlikely that the capturing properties of the grooves may be sensitive to the details of the yield curve at small energy but we have yet to run simulations to test this supposition.

In further calculations we studied the dependence of the e-cloud suppression properties on groove height and rounding of the groove tips. The latter would be a desirable feature for taming the impact on the beam impedance caused by the grooves and to ease manufacturing tolerances. We found that rounding the tips could significantly decrease the efficacy of the grooves and should therefore be included in the modelling. More details will be reported elsewhere.

ACKNOWLEDGEMENTS

Assistance from M. Furman and M. Pivi and fruitful conversations with W. Bruns, R. Cimino, C. Celata and J-L. Vay are gratefully acknowledged. Work supported by the Department of Energy Contract no. DE-AC02-05CH11231

REFERENCES

[1] L. Wang *et al.* NIM-A **571** (2007) p. 588.

[2] G. Stupakov and M. Pivi, SLAC-TN-04-045, SLAC (2004).

[3] G. Rumolo and F. Zimmermann, "LC e-Cloud Activities at CERN", talk presented at the ILC-DR 2006 Workshop, Cornell (2006).

[4] M. A. Furman and M. T. F. Pivi, LBNL-49771, Phys Rev. ST-AB **5** 124404 (2003); and LBNL-52807.

[5] M. Pivi *et al.*, *Simulations of the Electron Cloud for Various Configurations of a Damping Ring* , EPAC06 proceedings (2006).

[6] R. Cimino *et al.*, PRL **93** 014801 (2004).

[7] G. Bellodi, CARE-HHH 2004 Proceedings (2004).

Experience with ion and dust clearing in the CERN AA and EPA

A.Poncet AT-MCS

1) Introduction

During the decade 1983-1993, an intense activity was devoted at CERN to understand and resolve detrimental trapped ion and dust particle effects in the CERN Antiproton Accumulator (AA) and to a lesser extent, in the Electron-Positron Accumulator (EPA). During the design and construction of the AA, the first storage ring built with a continuous DC beam of negative space charge, trapping of positive ions from ionization of the residual gas was anticipated and metallic clearing electrodes of conventional design were installed. The same was done for the EPA, built at about the same period, although the expected ion trapping effects on the beam were initially thought to be less detrimental.

As the two machines progressively ramped up in performance over the years, it became rapidly obvious that trapped species effects had been under estimated and the race to understand and solve the problems gained impetus as years past. All references to the work carried out during this period are to be found in the proceedings of the Cern Accelerator School held in Snekersten, Denmark in June 1999: report CERN 99-05, pages 194-200.
We shall simple outline the phenomenology in this brief account.

2) The CERN Antiproton Accumulator (AA)

In the AA, equipped with very sensitive and elaborate Schottky diagnostics, the beam neutralization could be measured to be less than 1% with the initially installed metallic clearing electrodes turned ON, see Fig. 1:

Figure 1 : AA neutralisation incoherent tune shift

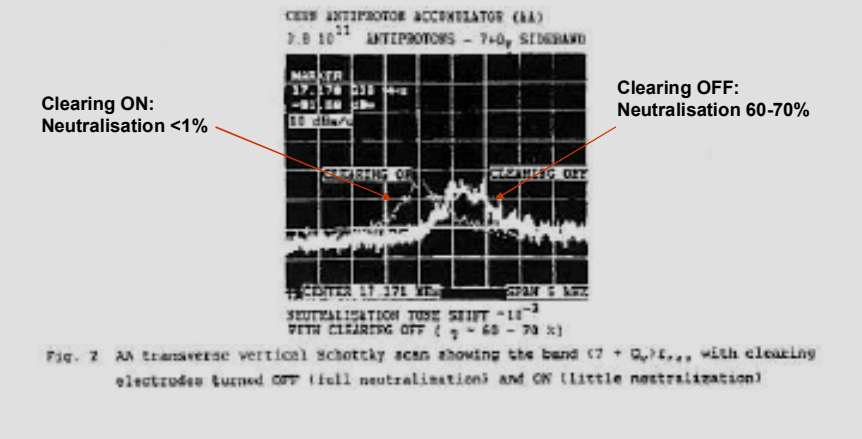

Fig. 2 AA transverse vertical Schottky scan showing the band $(7 + Q_y)f_{rev}$ with clearing electrodes turned OFF (full neutralisation) and ON (little neutralization)

However, as beam intensity ramped up over years, coherent (two beams) instabilities – dipolar and quadrupolar – appeared (see Figs. 2 and 3).

Figure 2 : Severe ion/pbar instability problems in AA
dipolar and quadrupolar
(coherent effect)

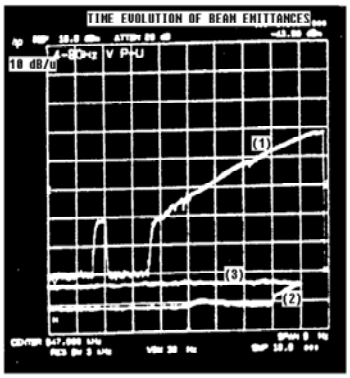

TRACE 1 : HORIZONTAL EMITTANCE (10 sec FULL SPAN)
TRACE 2 : " IDEM " (10 mn FULL SPAN)
TRACE 3 : VERTICAL EMITTANCE (10 mn FULL SPAN)

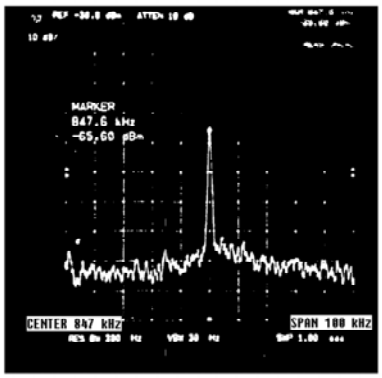

FREQUENCY SPECTRUM AROUND 847 kHz SHOWING THE COHERENT QUADRUPOLAR SIGNAL OF THE $(5-2Q_h)f_r$ MODE

1 st March 2007 ECL2 workshop 2
A.Poncet CERN CERN AA and EPA clearing systems

These instabilities did not generally cause beam losses but they represented a "heating" mechanism through sudden emittance "hiccups", giving an impassable bottom line for the emittance stochastic cooling systems.

Figure 3 : AA "bloody" phantoms !

Horizontal and Vertical emittances Versus time

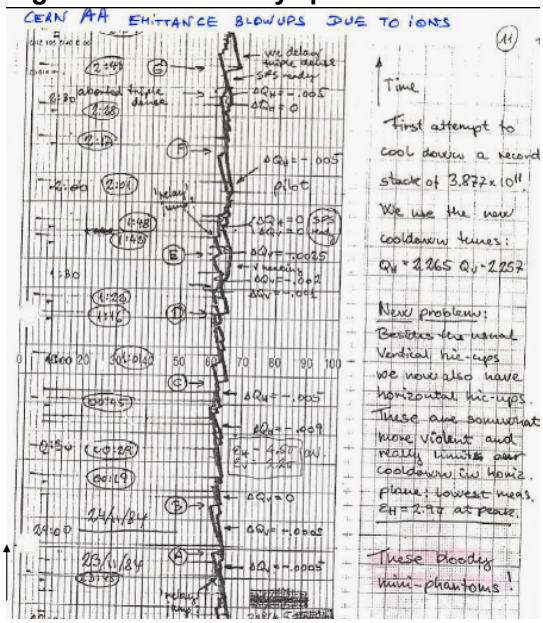

1 st March 2007 ECL2 workshop 4
A.Poncet CERN CERN AA and EPA clearing systems

In addition to these coherent heating "hiccups" phenomena, the AA in-depth comprehension effort showed that very high order non-linear resonances could be excited by residual ion neutralization pockets (resonances up to 17th order in the AA. Fig. 4).

Figure 4 : Excitation of HIGH order resonances by ion pockets (AA)
incoherent effect

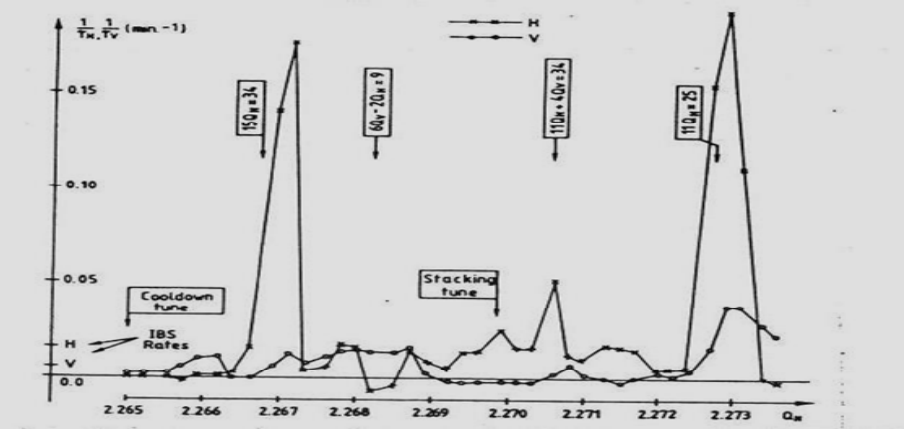

1 st March 2007 ECL2 workshop 5
A.Poncet CERN CERN AA and EPA clearing systems

It was shown that (for the AA) the driving terms of these resonances could exist with few neutralization pockets, with a possible very "peaky" transverse ion distribution, if the clearing field was insufficient to drive out ions or if beam longitudinal potential wells were left without clearing electrodes (Fig 6).

Figure 6 : Required clearing field to fully remove ions…caveat : transverse ion distribution is not (necessarily) a replica of the beam ! (P.Tavares)
(one must also take into account longitudinal drift velocities)

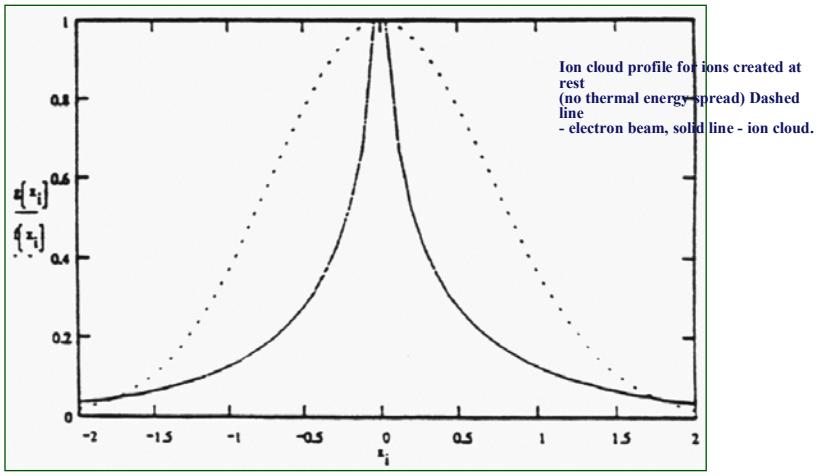

1 st March 2007 ECL2 workshop 14[33]
A.Poncet CERN CERN AA and EPA clearing systems

To complete the phenomenological picture of trapped species in the AA, dust particles detached from the vacuum chamber walls under the action of vibrations caused by the stochastic cooling shutters were found to be very detrimental for the beam. These so-called "phantoms" caused sudden emittance blow-ups and sometime beam loss (Fig. 7).

Figure 7 : CERN AA:effect of charged microparticles trapped into the beam

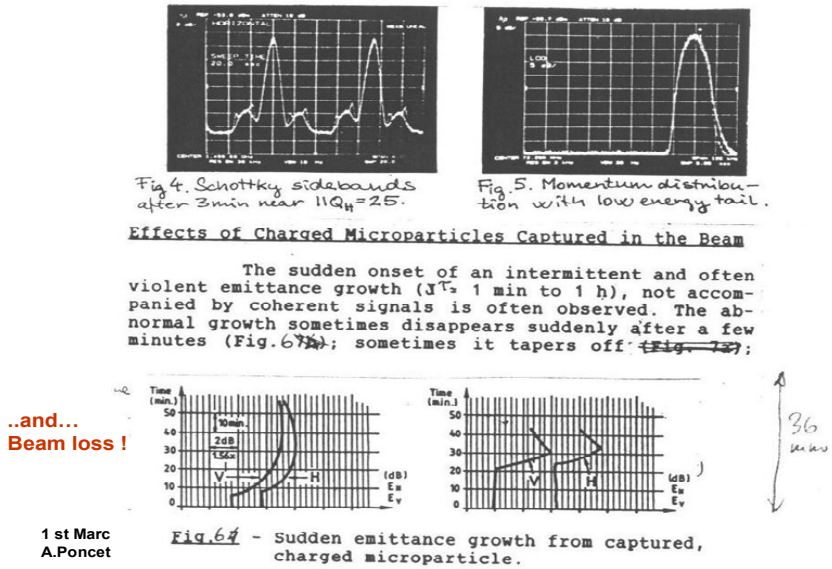

Due to beam low density when compared to electron beams (e.g. EPA), these micron size particles could stay for tens of minutes in the beam, being eventually dragged around the machine while trapped in the beam, by the beam longitudinal electric field, or particle drag forces.

Figure 8 : AA clearing system (after improvements)

Features: **-"quick" change from positive to negative adjustable DC voltage**
-individual measurement of clearing current (in picoamps)
-polarised BP PU's in quads
-continuous upgrade with resistively plated ceramics in LS and dipoles

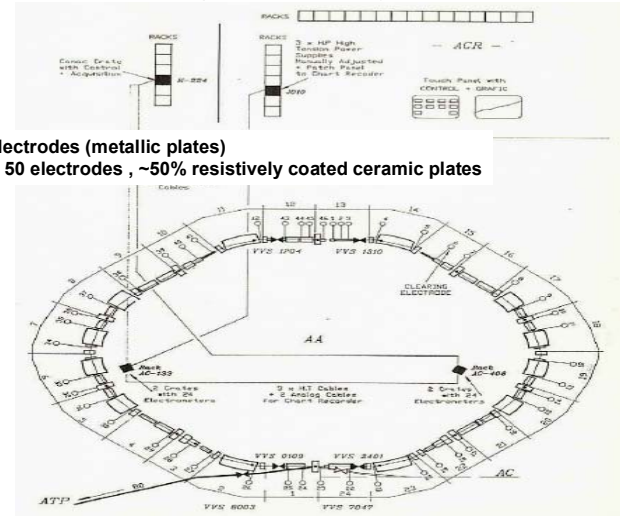

Initially : 20 electrodes (metallic plates)
At the end : > 50 electrodes , ~50% resistively coated ceramic plates

1 st March 2007 **ECL2 workshop** **8**
A.Poncet CERN **CERN AA and EPA clearing systems**

Much work was devoted to understand and control these effects; finally additional clearing electrodes and dynamic control of individual clearing fields permitted to alleviate the problems. Figures 8 and 9 illustrate the final clearing electrode system of the AA at the end of its life.

Figure 9 : AA clearing electrode control and acquisition of the clearing current (F.Pedersen)

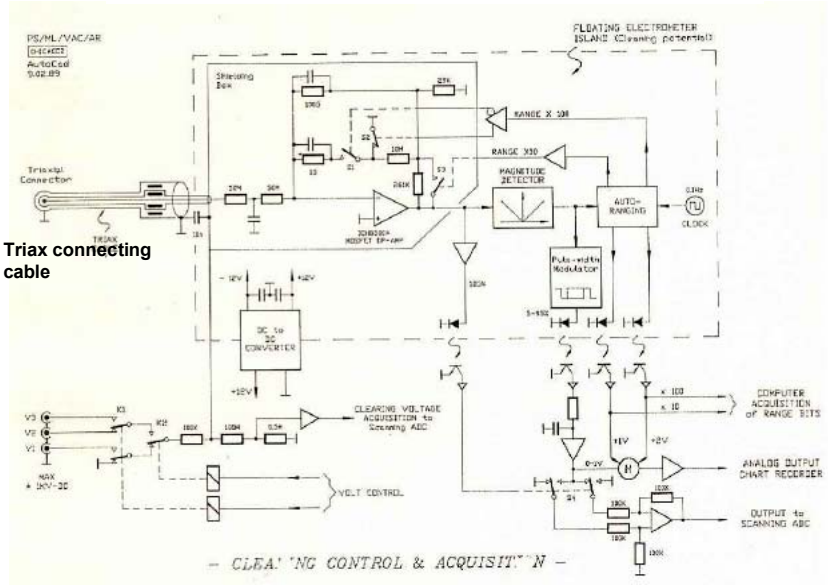

1 st March 2007 ECL2 workshop 9
A.Poncet CERN CERN AA and EPA clearing systems

From the initial 20 metallic electrodes DC powered in series, the machine ended up with more than 50 electrodes, half of them made of resistively-coated ceramic plates to reduce the coupling impedance with the beam. Additionally, all electrodes could be individually computer controlled from negative to positive adjustable voltages and the ion extracted current measured down to picoamps. Individual switching ON and OFF of the electrodes, or by reversing the applied voltage from negative to positive, allowed the modulation of the neutralization and therefore of the longitudinal beam potential. This permitted to drag around trapped dust particles to neighbouring extracting electrodes. Also ion current measurements gave useful information on the phenomenology of trapping, as for instance the position of residual pockets.

3) The CERN Electro-Positron Accumulator (EPA)

Much of what was learnt, diagnosed and solved concerning ion trapping was also applied to EPA, which, with its 8 consecutive bunches with close spacing was also prone to trapping. If clearing fields in EPA allowed to more than double the intensity stored in a cycle, like for AA residual ion pockets were always present, as seen by vertical and horizontal betatron motion coupling.

Figure 10 : "Button" EPA clearing electrodes

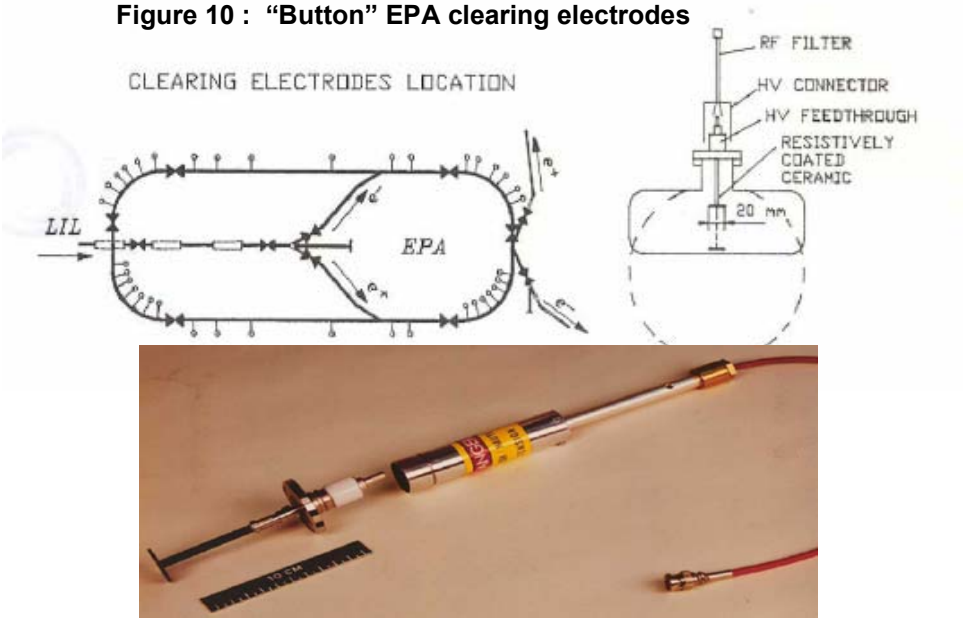

Although to a lesser extent than the AA, the EPA clearing system was for that reason continuously upgraded with additional ceramic-plated electrodes presenting a low coupling impedance (see Figures 10 and 11).

Figure 11 : Possible electrode drawback : coupling with the beam (from F.Caspers):

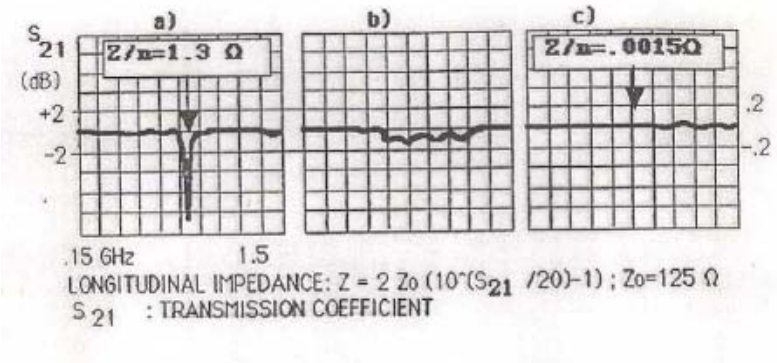

a) metallic electrode

b) Metallic electrode with RF filter

c) Ceramic electrode with resistive coating and RF filter

Extracted ion current measurements were also used to diagnose neutralization effects (Figs 12 and 13).

Figure 12 : EPA clearing current as function of clearing voltage

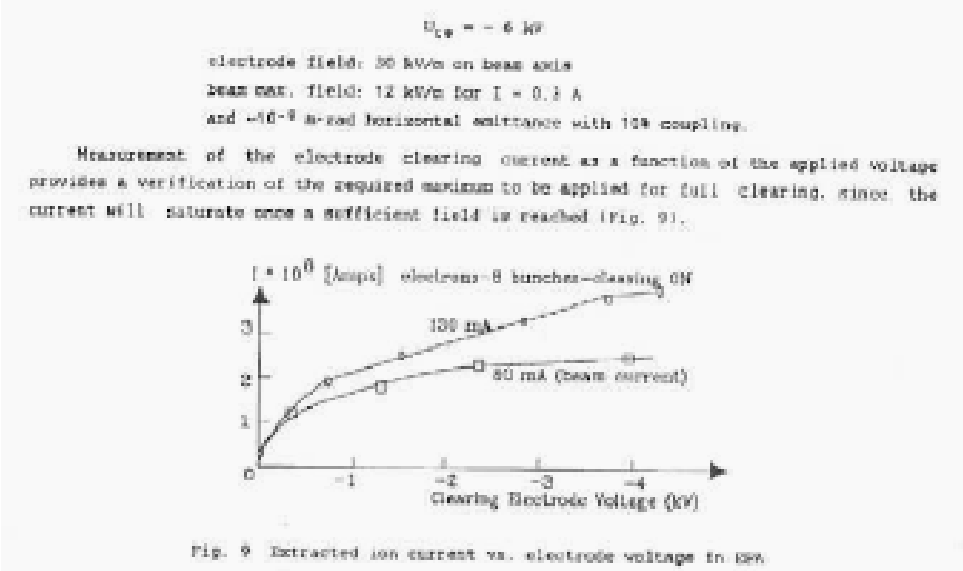

1 st March 2007 ECL2 workshop 15
A.Poncet CERN CERN AA and EPA clearing systems

Figure 13 :AA clearing currents as a function of DC clearing voltage

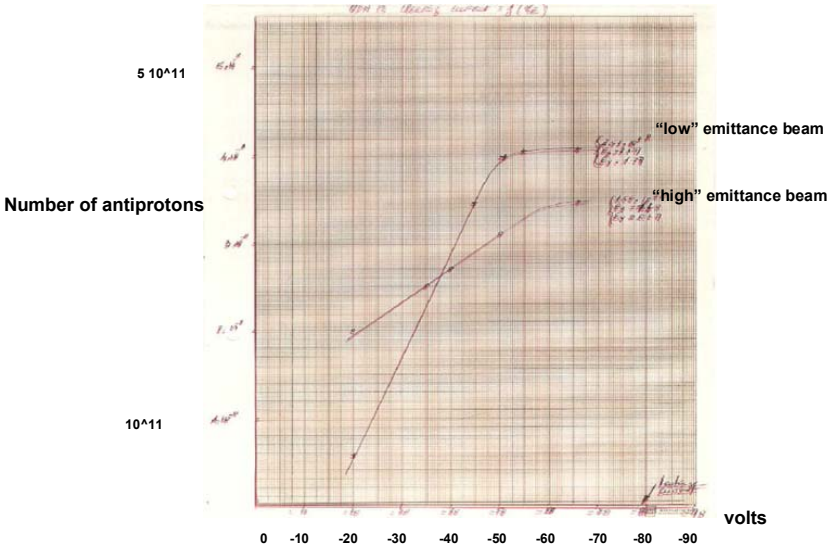

1 st March 2007 ECL2 workshop 16
A.Poncet CERN CERN AA and EPA clearing systems

Finally, for both machines, the adequate solution for residual detrimental ion effects was found in so-called beam shaking close to an (N-Q) frequency band, as close as possible to main ion transverse bounce frequencies (e.g. CO+). The spectacular positive effects of beam shaking (provided there were enough clearing electrodes switched ON !) are

illustrated in Fig. 14 (for the Fermilab Antiproton Accumulator) and Fig. 15 for the CERN EPA, where it is seen that shaking could be used to remove residual ions from the beam, and then suppressed, the beam staying clear of ions for minutes.

Figure 14 : Fermilab AA : effect on accumulation rate of shaking the beam (works only with clearing on)

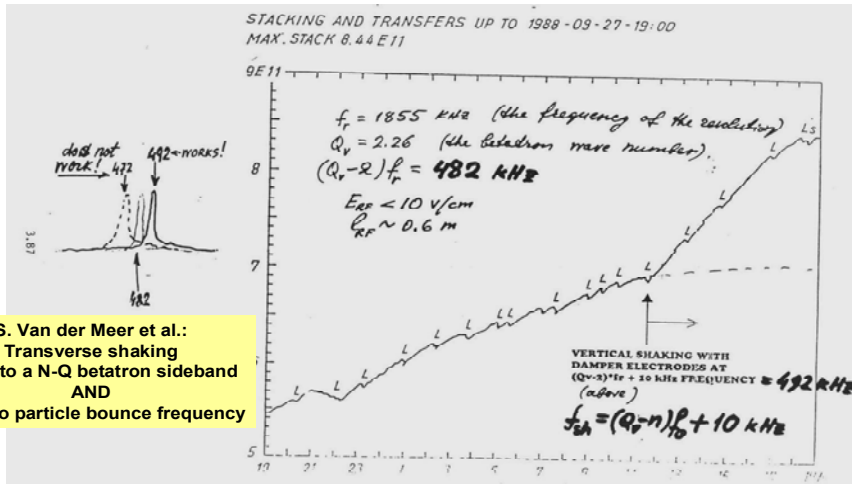

S. Van der Meer et al.:
Transverse shaking
Close to a N-Q betatron sideband
AND
Close to particle bounce frequency

Figure 15 : CERN EPA : effect of shaking the beam (works only with clearing ON)

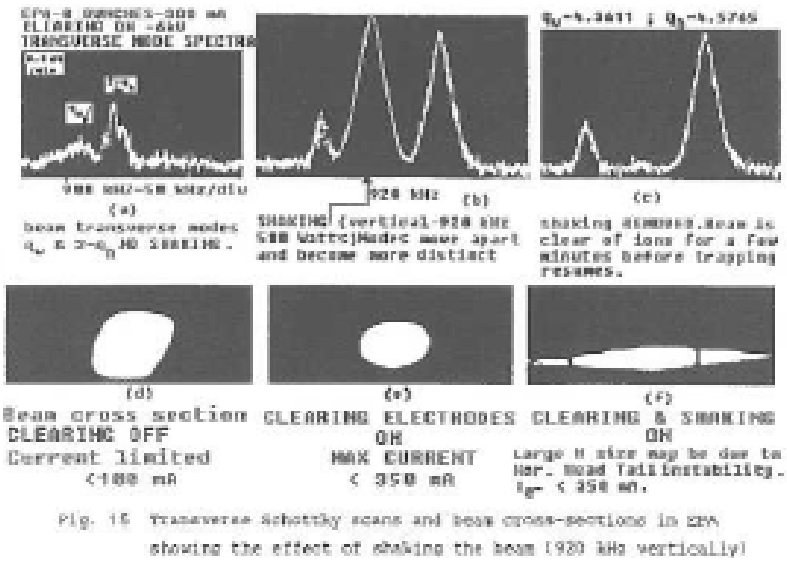

Fig. 15 Transverse Schottky scans and beam cross-sections in CERN showing the effect of shaking the beam (920 kHz vertically)

In conclusion, clearing electrodes of low impedance design, in large numbers and adequate clearing voltages proved to be essential for the performance of AA's and EPA. However, they turned out to be always insufficient to clear out all residual ion pockets, and beam shaking techniques had to be developed to finally solve all "phantoms".

VITREOUS ENAMEL A HIGHLY EFFECTIVE MATERIAL COMPOUND

J.C. Wendel, Wendel Email, Dillenburg, Germany
P. Hellmold, Univ. Clausthal-Zellerfeld, Germany

Abstract

Vitreous enamel is presented to be a highly effective material compound with designable properties. In general an enamel is a special glass, with a thermal expansion rate precisely adapted to it's substrate. It' s a bulk solid quenched from the melt – exhibiting a glass transition temperature. This is a general difference to amorphous materials deposited by sputtering or evaporation. This paper concentrates on the electrical properties and the adherence on the substrate.

ELECTRICAL PROPERTIES

Most of the glasses are electrical insulators. The specific electrical resistance of insulating enamels at room temperature is approximately 10^{12} Ωcm, which decreases to approximately 10^5 Ωcm at 400°C. Of course the isolating properties of the enamel depend of the thickness of the enamel layer. Especially for the dielectric strength this matters. The existence of semi conducting glasses is known since about forty years. They are used for photovoltaic application and xerography. These glasses show an electronic conductivity. It has been made good progress in understanding the mechanisms of ion and electron transport in glasses. Electronic conductivity is achieved when elements with more than one oxidation level (Fe, Mn in silicate boron- glasses, V in phosphate-glasses) are built in the glass [1]. In this case we find also a dependence from the oxygen partial pressure of the smelt.

Effect of composition elements

The Nernst-Einstein equation is giving a good description for the electrical conductivity: The diffusion rate is mainly determining the effect [2].

- Charge transport is mostly done by cations.
- Alkali metal ions have the highest diffusion rates.
- A glass free of network modifiers is having a low conductivity.
- BaO, SrO, PbO, CaO and SiO_2 decrease the conductivity due to the effect of polarisation and the blocking of channels.
- Na_2O, Li_2O, K_2O, Rb_2O and Cs_2O increase the conductivity approximately in the order of their appearance in the list (Na_2O most).
- The mixing of alkali oxides has a considerable effect.

Mixed alkali effect

One would expect a direct line between ionic conductivity and glass stoichiometry and would suggest that variations in conductivity are related to the presence of certain chemical entities in glass.

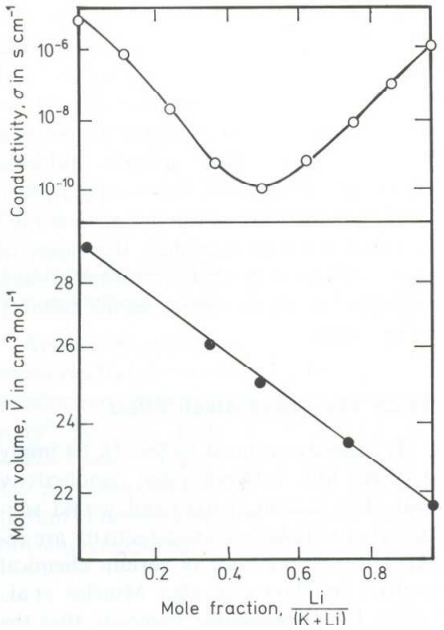

Figure 1: Conductivity and Molar volume in the system $(Li_2O/K_2O)*2SiO_2$ at 150°C [3].

But mixing of alkalis in enamel produces a pronounced minimum (4 orders of magnitude) in the conductivity. The effect is illustrated in the figure 1 for potassium-lithium-disilicate (conductivity vs. mole fraction). Physical properties like the molar volume do show the expected additive relationship.

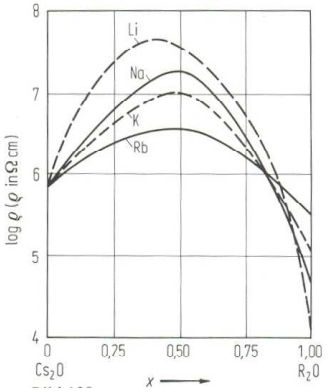

Figure 2: Specific electric resistance by substitution of Cs_2O in the glass 0,15 $(Cs,M)_2O*0,85\ SiO_2$ [4].

The effect is universal to all ion conducting glasses. Each type of alkali modifies the network structure to its own requirements : Li^+-ions create for themselves smaller sites than do K^+ ions. Therefore there can be no rapid "exchange of sites" between different alkali. Figure 2 shows the same effect for the specific resistance for a Caesium glass replacing Caesium by other ions. The substitution of Cs_2O in the glass 0,15 $(Cs,M)_2O$*0,85 SiO_2 by different alkali oxides leads to a maximum for the electric resistance at a molar fraction of approximately 0,5 [4].

The effect of temperature

In general the specific resistance decreases as the temperature increases, while the dielectric constant increases. The increase of the temperature doesn't have much influence on the polarisability of the ions, but the mobility of the ions increases very much which has an influence on the dielectric constant too [5].

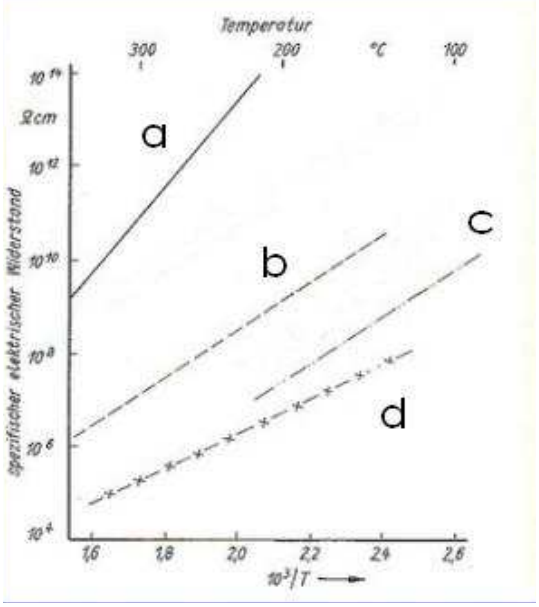

Figure 3: Temperature dependence of the specific electric resistance [6].

Figure 3 shows the temperature dependence of the specific electric resistance of different enamels: a PbO containing enamel free of alkali oxides (a), a conventional white line enamel (b), an enamel with a higher content of alkali oxide (c) and an antimony enamel (d) [6]. We find typical Arrhenius plots showing the extrinsic conductivity due to vibration of the network and opening of channels for the migration of the ions. In the case of water adsorption on the enamel surface a special surface conductivity may be found due to the formation of hydroxyl ions. A higher conductivity on the surface may be also due to the enrichment of alkali ions on the surface resulting from the process of smelting the enamel onto the substrate.

Mechanistic model

The cation mobility and the immobility of the anions can be intuitively understood by Figure 4. The Warren Biscoe version of the structure of an alkali silicate glass reduced to two dimensions shows the cations placed in "holes" inside the glass structure.

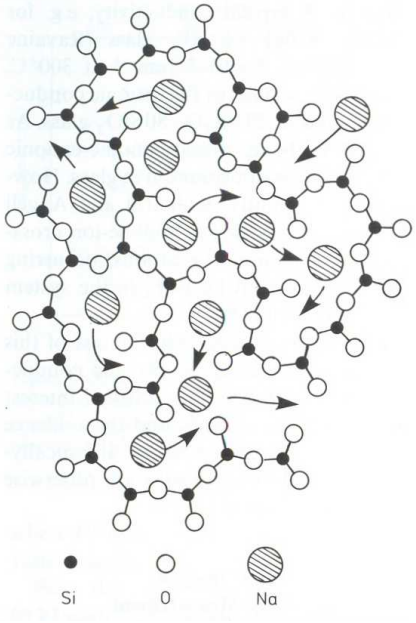

Figure 4: A schematic representation of the structure of an alkali silicate glass showing the possibilities of cationic motion [7].

The possibilities of localized and extended cationic motion within an anionic silicate framework is shown. The shape of the channels inside the silicate framework is largely predetermined by the partially broken (and usually modified) network.

Frequency dependence and Dissipation factor

The dielectric constant also depends from the applied frequency. This is easy to understand, as the cations may only follow the applied electric field at lower frequencies. Therefore the dielectric constant decreases with increasing frequency. The amount of energy consumed e.g. for the motion of the ions to build up an electrical current corresponds to tan δ - the dissipation factor. Just as the dielectric constant also the dissipation factor depends from the composition of the glass, temperature and frequency. Figure 5 is a schematic depiction of the theoretical addition of the different dissipation contributions [8]: Curve 1 describes the conduction losses. With decreasing temperature and increasing frequency the possibilities for the motion of the cations becomes lower and the conduction losses decrease. Curve 2 describes the relaxation losses: the ions may follow the applied field only with jumps over a small potential barrier – these losses appear mostly at low frequencies. At higher frequencies may appear a resonance with the natural oscillation of the ions. Big ions (curve 3) have a

slower natural oscillation therefore the resonance appears at lower frequencies. Finally the network may start to oscillate in larger areas, the result is a deformation which leads to the deformation losses (curve 4) which are expected mainly at lower temperatures. The full line results from the addition of all contributions.

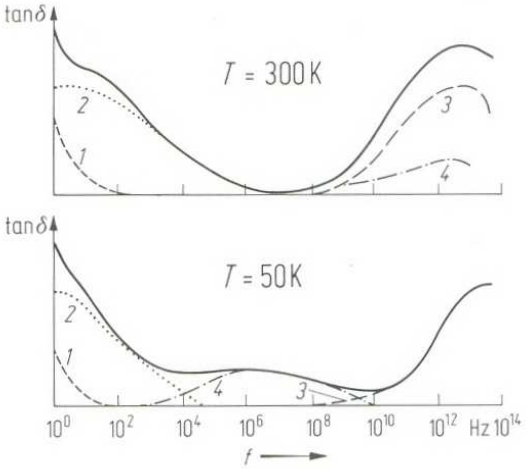

Figure 5: Schematic depiction of the variation of the dissipation factor with the frequency [8].

This theoretical approach doesn't have a scale on the axis of tan δ. To find a scale we compare with figure 6.

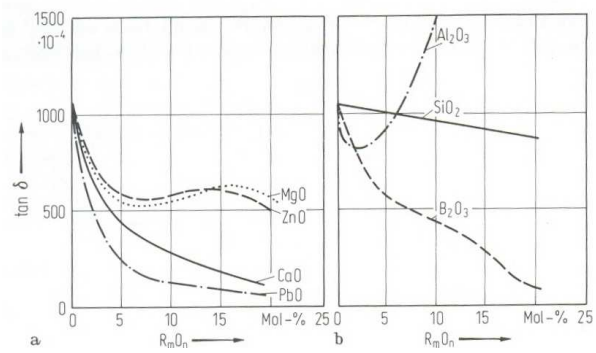

Figure 6: The influence of the chemical composition on the dissipation factor at a frequency of 1 kHz [9].

At low frequencies the mobility of the alkali ions is significant. With a decreasing content of alkali or an increase of boron oxide or calcium oxide in the $Na_2O*5SiO_2$ Glass the dissipation factor is decreasing [9]. The increase due to aluminium oxide is explained by the expansion of the network forming larger cycle structures which support the alkali ions with larger channels to move [5].

ADHERENCE ON IRON SUBSTRATES

A main point for the use of enamelled products is the adherence of the enamel on it's substrate. The enamel does not stick like a film on the surface, instead of that a chemical reaction between the substrate and the enamel occurs. So the adherence on iron substrates may be explained on the one hand by mechanical interlocking of the materials. Important factors are the roughness of the iron surface and an electrolytic corrosion which is mostly caused by a reduction of adhesive oxides (CoO or NiO) [10]. Figure 7 shows the thermodynamics for the most probable reactions which lead to metallic Cobalt – the reactions for NiO are similar. The reactions are calculated for wüstite ($Fe_{1-x}O$). The corresponding chemical reaction are pointed out simplified (FeO). It is obvious that the most probable reaction is the reduction by intermediate formed wüstite [11].

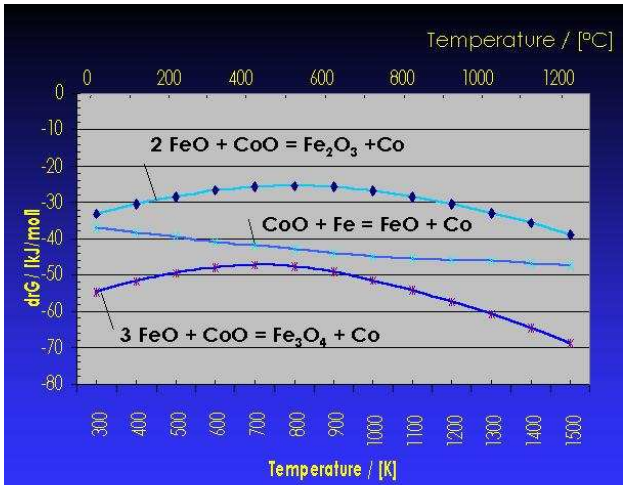

Figure 7: Free reaction enthalpies as a function of the temperature for CoO [11].

The presence of adhesive oxides is increasing very much the surface roughness of the iron. Dietzel explained the way of acting of the adhesive oxides and the surface roughening. Sometimes we find small particles of iron made by disproportion of wustite to magnetite and iron. These particles we find usually at the border iron/enamel. The cobalt film on the surface has a thickness of approx. 0,01 µm. The cathodic areas (without cobalt) are attacked selectively and so cavities are created. Figure 8 shows a schematic depiction of the galvanic process during enamelling of iron.

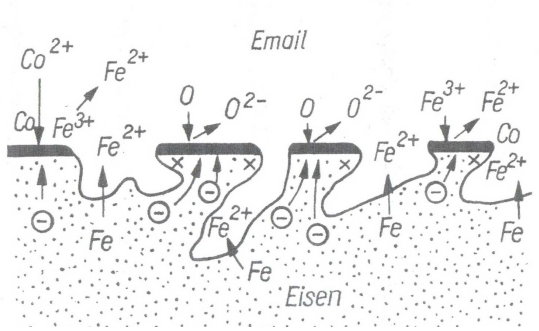

Figure 8: Schematic depiction of the galvanic process [12].

On the other hand a good adhesive iron oxide layer is needed [13]. The main phases should be magnetite which increases the adherence, hematite decreases the adherence. The thickness of the intermediate oxide layer is important [11]. Figure 9 shows the phase diagram (first kind) of the system Fe – Fe_2O_3. The areas for the stability of the three important iron oxides are shown.

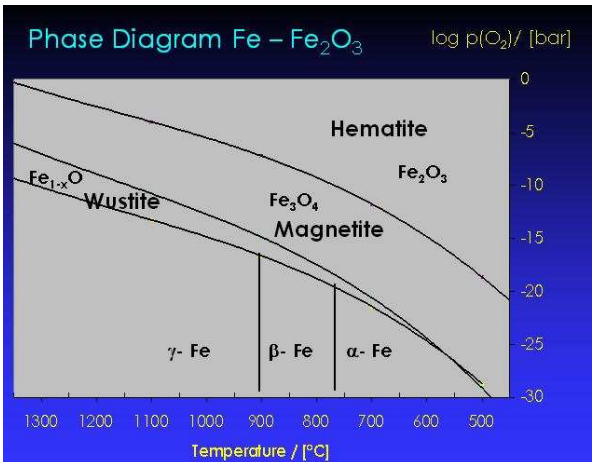

Figure 9: Phase diagram of the system Fe – Fe_2O_3 [11] – calculated with data from [14, 15].

The phase transformation from α-Fe (bcc) to β-Fe at 768°C is due to the Curie temperature. The transformation at 906°C from β-Fe to γ-Fe (fcc) is due to a change of the structure.

Thermal expansion rate

Another important point for a good adherence is the balance of the thermal expansion rates of the substrate and the enamel. Figure 10 shows the development of the tensions in the system metal/ enamel during cooling: starting with the temperature when the enamel becomes solid in the area of Tg (transformation area (+)) the enamel is first under tensile stress. The neutral point (T_N) is free of tension and below T_N compressive stress (-) is built up.

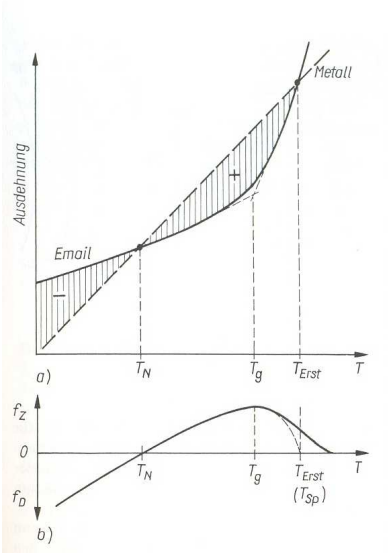

Figure 10: schematic depiction of the forming of stress in the system metal/ enamel during cooling [16].

DEVELOPMENT OF NEW ENAMELS

When a new enamel is designed various factors must be respected: The viscosity and the surface tension of the enamel must be corresponding to the working conditions of the enameller. The dilatation must be adapted to the substrate. The adherence must be moderated by a ground coat or adapted for a direct on enamel. The surface and the elasticity must be to the needs of the final user, just as the question if the enamel must be smooth, glossy or matt. The colour, the opacity, the amount of crystallization, electrical parameters as well as the chemical resistance to acids, alkaline and water may be designed to the wishes of the final user. Last but not least the slurry parameters must be adjusted to the needs of the enameller. The typical benefits are a very high resistance to heat or to cold, as well as a good adherence of the material compound and an excellent mechanical stability. Due to the fire polished surface there is a very good adherence of seals. Enamel shows a very low interaction with organic material and a perfect clean ability as well as perfect aging properties. The list of benefits is not complete – it's just a choice for the application for vacuum purposes.

REFERENCES

[1] M.D. Ingram, „Electrical Properties of Glasses“ in “Glasses and Amorphous Materials” ed. by J. Zarzycki Vol. 9 „Material Science and Technology“ VCH Weinheim 1991, 718.
[2] H. Scholze, “Glas – Natur, Struktur und Eigenschaften”, 2. Aufl. Springer Berlin 1977, 240.
[3] D.E. Day, J. Non-Cryst. Solids 21 (1976) 343.
[4] R.M. Hakim and D.R. Uhlmann, Physics Chem. Glasses 8 (1967) 174.
[5] H. Moore and R.C. de Silva, J. Soc. Glass Technol. 36 (1952) 5.
[6] A. Petzold and H. Pöschmann, “Email und Emailliertechnik” 2. Aufl. Dt. Verl. für Grundstoffindustrie 1992, 326.
[7] B.E, Warren, J. Am. Ceram. Soc. 24, (1941) 256.
[8] J.M. Stevels, Glastechn. Ber. 26 (1953) 227.
[9] D.W. Rinehart and J.J. Bonino, J. Amer. Ceram. Soc. 42 (1959) 107.
[10] A. Dietzel, Mitt. VDEfa 27 (1979) 6.
[11] J.C. Wendel, Mitt. DEV 53 (2005) 61.
[12] A. Dietzel, Sprechsaal 67 (1934) 265.
[13] A. Dietzel, Mitt. VDEfa 11 (1963) 71.
[14] L.S. Darken and R.W. Gurry, J. Amer. Chem. Soc. 67 (1945) 1398.
[15] L.S. Darken and R.W. Gurry, J. Amer. Chem. Soc. 68 (1946) 798.
[16] A. Petzold and H. Pöschmann, “Email und Emailliertechnik” 2. Aufl. Dt. Verl. für Grundstoffindustrie 1992, 65.

ECL2 Workshop
CERN
March 1st 2007

Eisenwerke Fried. Wilh. Düker GmbH & Co. KGaA
Laufach

F.-J. Behler, G. Nose, H. Kunkel

Industrial Enamel - Foundations, production, applications and CERN-tests

- Classification of Industrial Enamel rsp. glasslined technical equipment:
  „… enamelling used in processes in which physical and chemical stress are in a main consideration…“
- Basic features of glasslined technical equipment
- Enamel optimized design and different illustrative examples based on industrial enamelling
- Applications aside from the general known ones in plant construction of chemical industry
- ELC2 – first steps, open questions

Glasslined technical equipment as all-round material is firmly established between surface finishing materials fulfilling rather inferior demands and the special materials with to some extent very specific performance data particularly in the chemical and pharmaceutical industry but also for water supply systems and in special niches in general machine construction.

Depending upon the area of application enamel with its generally broad function profile can be adjusted to meet special demands. Whether for supplying potable water, textile chemicals or in the treatment of waste water, in soldering plant construction and in the pharmaceutical industry under the GMP conditions or to comply with hygienic design stipulations, enamel fulfils many and varied demands with different focal points by linking the structure material with the surface finish determining grades of enamel.

Enamelling itself, from the material technology point of view, is a clearly describable and controllable process. The physical and chemical relationships are known and generally offer a broad range of possibilities to optimally adjust the interrelationship between basic material and the surface determining enamel to the given load conditions. The mechanical limits of the material system are known and can be certainly calculated and any possible fear of "spontaneous flaking" results as a general rule through the lack of knowledge of these interrelationships.

Typical material properties

The term glasslined technical equipment can be seen to be analogue with industrial ceramic. It would appear sensible to differentiate between commercial enamel for every day use in the home or for jewellery, etc., because as far as glasslined technical equipment is concerned the technological demands put on the surface finish are in the foreground. As a consequence, this

term is applied for enamelling in processes in which physical and chemical stress conditions can be defined and the thus derived demands on the surface system are the main consideration.

The main typical material features of glasslined technical equipment:

- High resistance to corrosion attack, more especially in the case of acidic media even at higher processing temperatures.
-
- Color permanence, stable in presence of rain, snow, dust, heat, sunlight, oxidizing agents and corrosive fumes, unaffected by ultraviolet and infrared radiation
- Gloss, specular reflectance in a span of 50 up to 60°, extremely in a range of 10 to 85°
- Light reflectance, white enamels have a reflectance of ca. 75% to 80%
- Higher resistance to wear by abrasive media
- Surface smoothness (Fig. 1)
- Easy to clean with no tendency towards adhesion
- Biological and catalytic inert behaviour

The properties of the enamel are supported by appropriate sophisticated constructive designs which strengthen the positive properties and overcome existing limitations as far as possible.

Electrical and High Temperature properties

- Dielectric strenght, ranges from 200 to 500 V/mil (total thickness 4 – 6 mils), 16 – 20 kV/mm (Biscardi et al., J. Vac. Sci. Tech. A, 2000), increases with dense, decreases with bubble structure
- Dielectric constant, 6 to 12, sharp increase in the temperature range 120 to 150 °C, volume resistivity (at 400 cycl/s), 1013 to 1016 Ω/cm at rt, function of temperature
- Dissipation factor (at 400 cycl/s), 1 to 2 %, increases above 93 °C, decreases with increasing frequency
- Resistance to oxidation and corrosion, barrier to diffusion of oxygen, protective ability depends on temperature at which it starts to soften (ca. 200 °C below firing temp.)
- Thermal stability, firing-temp. steel enamelling: 750 – 950 °C, thermal stability ranges 450 – 650 °C
- Thermal shock resistance, typical steel enamelling over 200 °C

Physicochemical compound material

Enamel as such is outstanding when compared with other popular surface coatings and finishes such as wet paint, powder coating, lining with plastic, etc., inter alia by the given intensive physical and chemical connection with the basic material. This is marked by diffusion processes from the basic material towards the enamel and vice versa. Over and above this forms a real compounding layer of but a few but also to some tens of micrometers thick depending on the material system (Fig. 2).

Optimal morphology by releasing elements close to the surface and linking the substrate material in the enamel matrix is initially generated to develop the mechanical and physical connection.

The increased roughness by releasing the substrate surface in connection with the development of backcuts offers a large number of anchor points for micromechanical positive connection.

This mechanism is supplemented by generating integral pressure tension in the enamel in cooled state which contributes in the further stabilisation of the mechanical compound. However, if the stress in the enamel layer is too high, this can also lead to increased sensitivity towards impact where convex surface elements are concerned.

Enlargement of the specific surface supports the development of intermolecular bonding apart from this mechanical and physical bonding mechanism. Considerable effects are achieved through Valenz and Van-der-Waals bonding but nevertheless, metallic bonding in the bonding layer likewise plays a role in the iron-silicium-oxygen system.

Basic conditions for high quality

The quality of any enamel depends on a large number of pertinent parameters and periphery conditions. Of decisive significance is the metallurgical quality of the basic material, its microstructure the mechanical pre-treatment it has been subject to and its surface finish.

Only steels with restricted analysis can be given a high quality enamel finish. Carbon, sulphur and almost all metal accompanying elements must be limited. Clean ferritic microstructure in the periphery layer facilitates enamelling. Carbon inclusions make enamelling more difficult in the same way as micro faults which can act like hydrogen traps. This applies generally for enamelling iron foundry materials.

Thermal and mechanical preparation is subject to two main conditions. Clean, abrasive acting blasting material cleans, activates and enlarges the surface (Fig. 3). However, any contamination of the surface must be avoided after blasting.

From this one can see the demand for a very quick production sequence, i.e. pre-treatment, application of the enamel slick, drying and firing the enamel.

Chemical and physical sequences while the firing at 850 °C

During the firing operation different chemical and physical processes take place dependent on temperature and time. Initially the surface of the steel is oxidised further under the drying slick and is supported by the residual moisture of the dried slick. Water and hydrogen escape.

Afterwards the oxide layer is released step by step by increasing the temperature, yet again. The chemical adhesion action takes place during this step, this being responsible for the development of the bonding zone to achieve the mechanical anchor. To be also considered is that the enamel does not fuse at a defined temperature but the fusing process takes place within a fusing period because the different enamel components fuse at different temperatures.

The various components have a different effect on both the dissolving behaviour of the oxide coating and the viscosity of the melt. Iron oxide escapes in the over saturated enamel melt and leads to faults that cannot be repaired (such as copper heads, and burn through) should the absorpabilty of the enamel be over stressed as a result of too long or too hot firing. Faults can occur which are also restricted locally in the case of less uniform distribution of the enamel mass.

The described sequences and effects contribute to differences in the base enamel (initial or first and second layer on the component) and the top enamel layer (and the build up of the following layer is aimed at ensuring the overall layer thickness). In function the softer less resistant basic enamel is responsible for optimal bonding to the basic material. The harder, highly resistant top enamel layer bonds very well with the base enamel and ensures the desired surface creating properties of the overall compound.

Mastered technology, broad field of application

Glasslined technical equipmentling from the material theory point of view, is a clearly definable and controllable process. The physical and chemical interrelationships are known and generally offer a broad range of possible optimal adjustments for the interrelationship between the basic material and the surface determining enamel within the given limits of the given load conditions.

Apart from the traditional areas of application in chemical plant construction, pharmaceutical and water supply systems, glasslined technical equipmentling is gaining increasing significance in general plant and machine construction. Glasslined technical equipmentling is a first choice material system in all those applications where marked resistance towards aggressive media is to be assured in conjunction with the mechanical strength even in the case of high process temperatures.

First step in the field of UHV-application at CERN, definition of requirements and open questions

As a first step to check the applicability of enamel coating in the field of UHV a steel pipe (diameter 100 mm, 500 in length) has been coated with a 20 mm broad enamel-layer inside (see also Fig. 4). It will be tested in the next time at CERN. To get a better feeling of the needed properties a number of requirements of the enamel layer has to be discussed and screened:

- Geometry, thickness, wideness
- Surface, smoothness, cleanliness of the enamel-free area

- Electrical and UHV-features
- Design of connection, flanges
- Production.

Figures, legend:

Figure 1:
Glasslined technical equipment with extremely smooth surface finish in conjunction with high wear resistance to abrasive acting media and high resistance to corrosion.

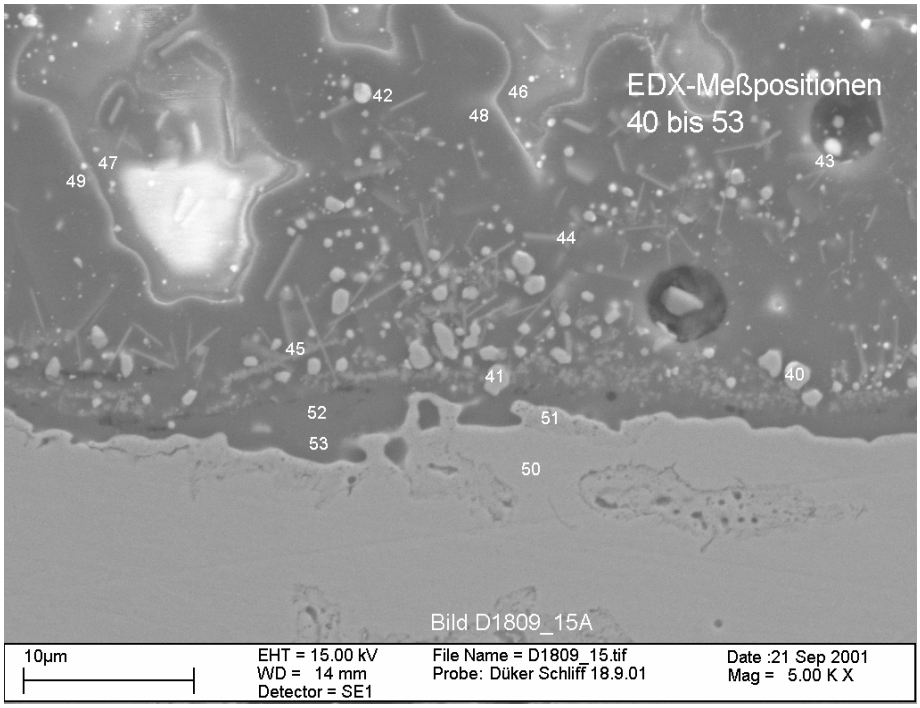

Figure 2:
Detail photograph of a compound layer enamel (in this case with grey cast iron (GGG) electron raster microscope photograph Fraunhofer-Institut ISC, Würzburg) in approx. 5000-fold magnification. Clearly visible is the (micro) roughness of the surface (bright to the bottom) with back cuts. Following to the top is a thinner homogeneous appearing seam about 2µm thick and the actual bonding layer afterwards clearly over 10 µm thick with different precipitations (ferrotitanium crystal in needle and pellet form) and inclusions.

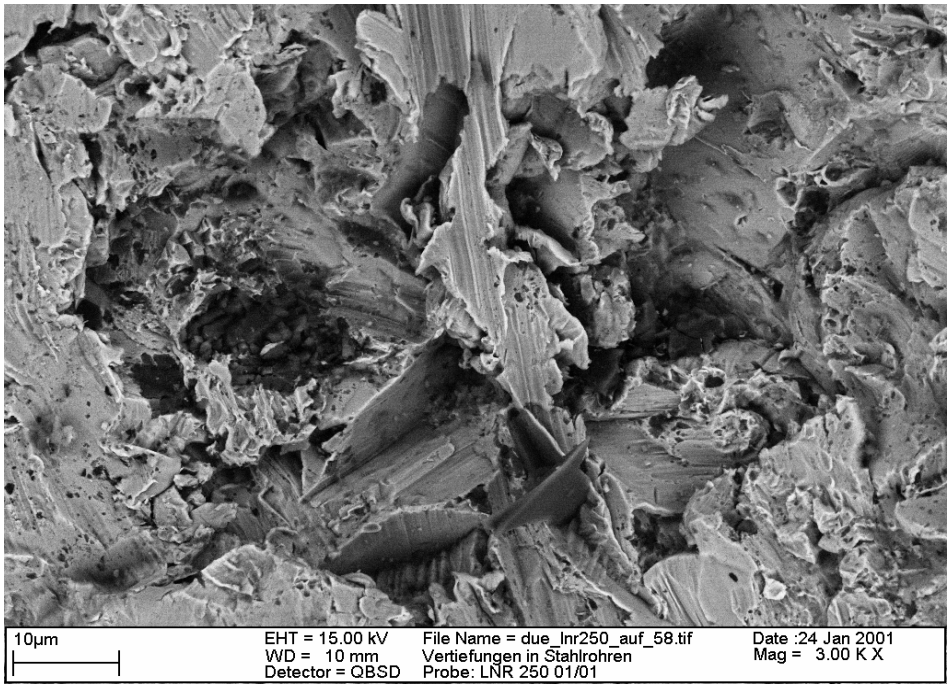

Figure 3:
Detail photograph of a corundum-blasted steel surface, approx. 3000-fold magnification (raster electron microscope photograph Fraunhofer-Institut ISC, Würzburg). The surface as a result of the blasting operation is clearly split and eroded. This finish offers an ideal surface for building up the material compound in the subsequent enamelling process.

Figure 4:
Prototype of a steel pipe (diameter 100 mm) coated with a 20 mm broad enamel-layer inside.

SEY AND CLEARING STUDIES AT KEKB

Y. Suetsugu, KEK, Japan

Abstract

Studies on the structure of beam ducts, the inner surfaces with a low secondary electron yield (SEY) and clearing electrodes have been continuously progressing at the KEK B-factory (KEKB), in order to mitigate the electron cloud effect. Copper beam ducts with ante-chambers were installed in the positron ring. Test chambers with TiN and NEG coatings were also installed in the ring, and the effect of those on the electron cloud was investigated. A rod-type clearing electrode with low beam impedance was proposed, and the RF properties were preliminarily evaluated.

INTRODUCTION

A great attention has been given to the electron cloud instability (ECI) in positron/proton accumulation rings, since it significantly affects the performance of accelerators. Various methods to cure the ECI have been investigated experimentally and theoretically. At KEK, the studies have been proceeding using the B-factory (KEKB), focused on the structure of beam ducts, inner surfaces with a low secondary electron yield (SEY) and clearing electrodes [1 - 7]. Copper beam ducts with ante-chambers were designed and manufactured for tests [3, 6, 7]. They were installed into the 3.5GeV positron ring (called as the Low Energy Ring, LER), and the effect on the electron cloud formation was investigated [4 - 7]. Test chambers with a TiN coating and a NEG coating were also installed in the LER, and the benefit of coatings with a low SEY to the electron cloud was studied, including the effect of photoelectrons. Furthermore, a rod-type clearing electrode with low beam impedance was proposed, and the RF properties were preliminarily evaluated using a simulation code. These recent results are reviewed here.

Fig. 1 Copper beam duct with two ante-chambers for tests.

#yusuke.suetsugu@kek.jp

BEAM DUCT WITH ANTE-CHAMBER

The beam duct consists of two channels, that is, a beam channel where a beam circulates, and an SR channels (ante-chambers) aside where the synchrotron radiation (SR) passes through [3]. By using the ante-chamber scheme, photoelectrons inside the beam channel, which could be a seed of the electron cloud, was expected to be reduced compared to that of a simple circular duct from a simulation.

Several kinds of copper beam ducts with ante-chambers have been manufactured, and installed into the KEKB LER. Copper (Oxygen Free Copper, OFC) was adopted for its high thermal strength and good radiation shielding property, considering a future high current operation [8, 9]. The inner diameter of the beam channel was 94 mm. The depth and the height of the ante-chamber were 65 mm and 15 mm, respectively. A copper beam duct with two ante-chambers is presented in Fig. 1, for example.

Beam ducts with one ante-chamber were installed in an arc section of LER. The photon density was about 8.5×10^{18} photons s^{-1} m^{-1} at a beam current of 1 A. The critical energy was 5.8 keV.

The number of electrons around the beam was measured by an electron monitor [10]. A reduction in the number of photoelectrons by one or two orders of magnitude compared to a simple circular duct was confirmed at a low-current region, less than 0.1 A, where the photoelectrons were dominant. The electron number at a high-current region, such as 1.5 A, was also smaller, but the reduction was only by a factor of 4. This is because the main component of the electrons at that region is the secondary electrons, which are generated in a multiplication process by highly-charged bunches. A typical behaviour of the measured electron current is presented in Fig.2, where the bunch spacing was 3.77 RF-

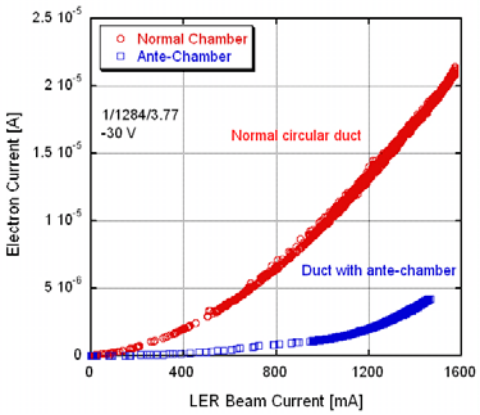

Fig. 2 Measured electron currents for a normal circular beam duct and a beam duct with ante-chamber (without coating).

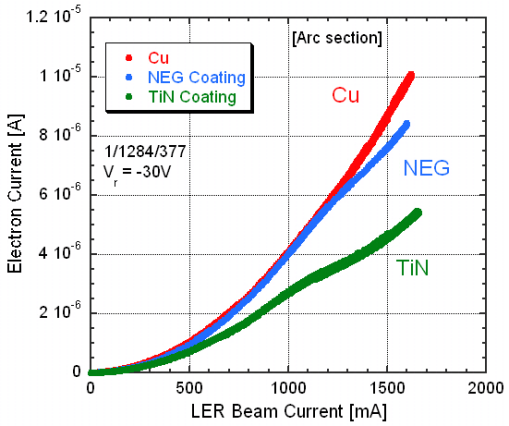

Fig. 3 Electron current for copper (Cu), NEG coating (NEG) and TiN coating (TiN) as a function of beam current measured at an arc section.

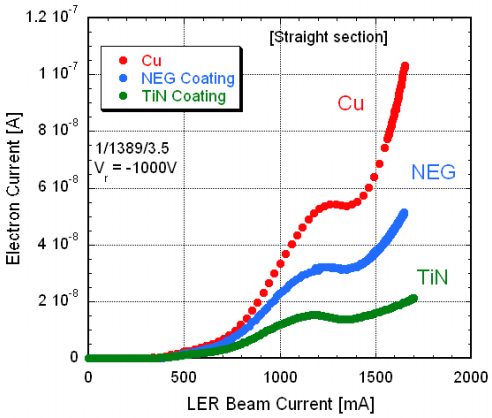

Fig. 4 Electron current for copper (Cu), NEG coating (NEG) and TiN coating (TiN) as a function of beam current measured at a straight section.

buckets in average, and the total bunch number was 1284 (1 RF-bucket = 2 ns). The repeller voltage of the electron monitor was -30 V. The beam duct with antechambers was found to be very effective to reduce the effect of photoelectrons.

Beam ducts with two ante-chambers, on the other hand, were installed at a wiggler section, where the SR hits the duct at both sides. The photon density was about 7.5×10^{17} photons m^{-1} s^{-1} at a beam current of 1 A. The similar results were obtained. The present circular beam ducts in a part of the wiggler section will be replaced to those with ante-chambers this year.

COATING WITH LOW SEY

To apply a surface with a low SEY to the inner surface of a beam duct is a promising way to suppress the electron cloud at a high beam current regime. Secondary electron and photoelectron yields (SEY and PEY) of a NEG coating and a TiN coating have been also studied using KEKB LER [4, 5]. Test chambers with the NEG and the TiN coating were first installed at an arc section of the KEKB positron ring. The test chambers have a simple circular cross section (ϕ94 mm). The thicknesses of the coatings were about one micro-metre. The number of electrons around a beam was measured up to a beam current of about 1.7 A, and compared with each other. The photon density was 6.5×10^{17} photons s^{-1} m^{-1} at a beam current of 1 A.

Figure 3 shows typical behaviours of the measured electron currents for the TiN-coated, NEG-coated and copper chambers, where the bunch spacing was 3.77 RF-buckets in average, and the total bunch number was 1284. The electron number (~ electron current) for the TiN coating was clearly smaller than that of the copper by a factor of 2. The electron number of the NEG coating, on the other hand, was almost the same as that of the copper. Only a small difference was observed at a high current region, around 1. 5 A.

Using a simulation, the maximum SEY (δ_{max}) and the PEY (η_e) of the TiN coating, the NEG coating and the copper were estimated based on the measured electron currents [5]. The δ_{max} and η_e for the TiN coating, the NEG coating and the copper were 0.8 - 1.0, 0.9 - 1.1 and 1.1 -1.3, and 0.13 - 0.15, 0.22 - 0.27 and 0.28 - 0.31, respectively. It was found that the TiN coating had an SEY (δ_{max} ~ 0.9) as low as that of the NEG coating (δ_{max} ~ 1.0), but the electron current was clearly smaller than that of the NEG coating, due to its lower η_e (~ 0.14). The electron numbers in the case of the copper and the NEG coating seems to be saturated, that is, limited by the space charge, because of abundant photoelectrons. This study indicated that suppression of photoelectrons is important to make effective use of a surface with a low SEY.

To see the effect of SEY more clearly, similar studies were performed at a straight section of the LER, where the photon density was less than 1/10 of that at an arc section (about 3×10^{15} photons s^{-1} m^{-1} at a beam current of 1 A). The electron numbers around beams were again measured during the beam operation, and compared with each other. A typical result is presented in Fig.4, where the bunch spacing was 3.5 RF-buckets in average, and the total bunch number was 1389. The repeller voltage was -1000 V. The electron numbers for the TiN coating and the NEG coating were about 1/3 and 2/3 of that in the case of the copper chamber, respectively. The difference between the NEG coating and the copper was clear in this case due to the small amount of photoelectrons. Assuming almost the same η_e values as in the previous experiment at the arc section, the δ_{max} values for three cases were again estimated using the previous simulation. The results were 0.8 - 1.0, 1.0 - 1.15, and 1.1 - 1.25 for the TiN coating, the NEG coating and the copper, respectively. They were almost consistent with those previously obtained at the arc section.

CLEARING ELECTRODE

Considered here was a conventional type as proposed by L. Wang et al. [11], where an electrode was a wire. Schematic structure of the electrode is shown in Fig. 5.

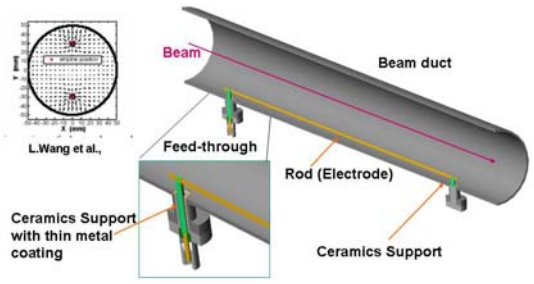

Fig. 5 Schematic drawing of a rod-type clearing electrode.

The feed-through had a high resistivity, which contributes to reduce the impedance of the electrode [12 - 14]. The estimation of the impedance and the loss factor has just begun using the MAFIA code.

In the calculation model, the electrode (rod) was set at 8 mm apart from the duct wall, and had a width, a thickness and a length of 3 mm, 4 mm, and 1 m, respectively. One end was supported by a ceramic rod (Al_2O_3, ε_r = 9.0) with a diameter of 4.8 mm. The other end was supported by a feed-through with a length of 40 mm. The feed-through was a ceramics rod with a metal layer on the surface with a thickness of 0.8 mm, and a width of 2 mm. The conductivity of the metal layer was designed so that the ratio of the thickness to the skin depth was about 40 at a frequency of 1.35 GHz. The model had a diameter of 94 mm, and the total length was 2.4 m. The simulation was done for a 1/4 model, that is, two electrodes were up and bottom of the duct.

Typical longitudinal impedance is shown in Fig.6. The longitudinal shunt impedance was about 1 Ω at 1.35 GHz. The *R*/*Q* was about 0.05. The transverse shunt impedance, on the other hand, was about 10 Ω, and the R/Q was about 5. The output voltage from the feed-through was estimated as a few volts at most. The loss factor was about 1.1×10^{10} V/C for a bunch with a length of 8 mm. Issues to be further investigated are to reduce the loss, to estimate the heating of electrode, and to evaluate the growth rate for the coupled-bunch instability and the microwave instability.

Beam test of the clearing electrode at a wiggler section of the LER is planed. The magnet has a length of 250 mm, and the magnetic field is 0.75 T. Design of a test chamber with an electrode and an electron monitor is now proceeding. The electron monitor will have 5 strips to see the spatial distribution of the electron cloud.

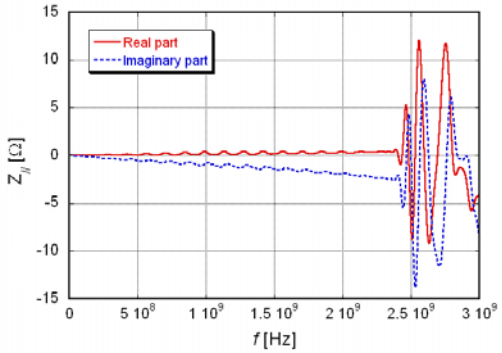

Fig. 6 Longitudinal impedance for a rod-type clearing electrode with a high-resistive feed through.

REFERENCES

[1] K. Akai, et al., Nucl. Instrum. Methods in Phys. Res. A, 499 (2003) 191.

[2] Y. Funakoshi, et al., "KEKB PERFORMANCE" , EPAC2004, 5-10 July, Lucerne, p.707.

[3] Y. Suetsugu, K. Kanazawa, K. Shibata, H. Hisamatsu, K. Oide, F. Takasaki, A.E. Bondar, V. Kuzminykh, A. Gorbovsky, R. Dostovalov, K. Sennyu and H. Hara, NIM-PR-A, 538 (2005) 206.

[4] Y.Suetsugu, K.Kanazawa, K.Shibata, H.Hisamatsu, K.Oide, F.Takasaki, R.V.Dostovalov, A.A.Krasnov, K.V.Zolotarev, E.S.Konstantinov, V.A.Chernov, A.E.Bondar and A.N.Shmakov, NIM-PR-A, 554 (2005) 92.

[5] Y. Suetsugu, K. Kanazawa, K. Shibata and H. Hisamatsu, NIM-PR-A, 556 (2006) 399.

[6] Y. Suetsugu, K. Kanazawa, K. Shibata, N. Ohuchi, H. Hisamatsu, M. Shirai, "R&D STATUS OF VACUUM COMPONENTS FOR THE UPGRADE OF KEKB", Proceedings of PAC2005, May 16-20, Knoxville, p.3256.

[7] Y. Suetsugu, K. Shibata, H. Hisamatsu, M. Shimamoto, M. Shirai and K. Kanazawa , "R&D on Copper Beam Ducts with Antechambers and Related Vacuum Components", Proceedings of EPAC2006, June 26 - 30, Edinburgh, p.1438.

[8] K. Kanazawa, S. Kato, Y. Suetsugu, H. Hisamatsu, M. Shimamoto, M. Sato, M. Shirai, Appl. Surf. Sci., 169-170 (2001) 715.

[9] K. Kanazawa, S. Kato, Y. Suetsugu, H. Hisamatsu, M. Shimamoto and M. Shirai, NIM-PR-A, 499 (2003) 66.

[10] Y. Ohnishi, T. Murakami, K. Kanazawa, M. Tanaka and M. Tejima, "Detection of Photoelectron Cloud in Positron Ring at KEKB", www-eng.kek.jp/heacc2001/ProceedingsHP.html.

[11] L. Wang, "Possible Remedies to Suppress electron cloud in ILC damping ring", in Vancouver Linear Collider Workshop, 19-22 July, 2006.

[12] F. Caspers, "Some Remarks on the Concept of Invisible Clearing Electrodes", ECLOUD02, 15-18 April 2002, CERN.

[13] M. Spataro and M. Zobov, "WAKE FIELD AND COUPLING IMPEDANCE OF DAΦNE ELECTRON RING", DAΦNE Technical Note, INFN-LFN, G-64, 2005.

[14] Y. Suetsugu, K. Shibata, A. Morishige, Y. Suzuki and M. Tsuchiya, Phys. Rev. Special Topics - Acc. Beams, 9 (2006) 103501.

Alternating slots for suppressing Electron Cloud Buildup

W. Bruns, CERN, Geneva, Switzerland

ALTERNATING SLOTS IN AN ELLIPTICAL CHAMBER, NO PHOTOELECTRONS

Slots on the beam pipe walls significantly reduce the electron cloud buildup. When a positively charged beam passes, electrons near the wall are accelerated towards the beam. Due to the magnetic field, they essentially move in y-direction. When they hit the opposite wall, secondary particles are created. Snapshots of the charge density in an elliptical beampipe at different times near the passage of a proton beam are shown in figure 2.

When the beam pipe wall is slotted, electrons which are within a slot will experience a much lower acceleration, as the slots effectively shield the TEM-field of the passing beam. The slots must be arranged alternating, such that an electron which starts on a unslotted part on one side of the pipe will land within a slot on the other side. Snapshots of the resulting charge density in a slotted elliptical beampipe at different times near the passage of a proton beam are shown in figure 3.

The charge density near the axis is shown in Fig. 1. That figure shows the results with four different slot configurations. Without slots, with a unbiased electrode behind the slots, and with a attracting and repelling electrode. Snapshots of the charge density are shown in Fig. 2, Fig. 3.

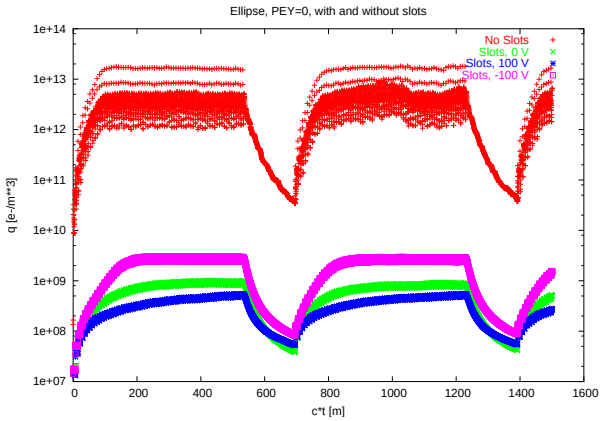

Figure 1: The charge density near the axis in the elliptical beampipe of figs. 2 and 3 as a function of c*t. Slightly more than two passages of a train of 72 bunches followed by 21 emtpy bunches are simulated. The bunches have a distance of 7.48 metres and a population of 11.5×10^{10} positrons. The y-directed magnetic field has an amplitude of 0.01 Tesla, which is rather small, smaller than the typical dipole fields in LHC or SPS. No photelectron generation is considered. The secondary emission yield is assumed to be 1.5 at 200 eV. The large red values are of a chamber without slots. The green values are when slots are on the beampipes wall. The lowest, blue values are computed when behind the slots an electrode with +100 Volt is assumed. The turqoise values are the results when behind the slots an electrode with -100 Volt is assumed.

SLOTS IN A LHC-LIKE CHAMBER

Unfortunately, slots do not have such a drastic effect on a LHC like chamber. Figure 4 shows the computed charge density near the axis in the case of only gasionisation without photoelectrons for unslotted chambers, for slotted chambers without voltage applied and for slotted chambers with voltage applied. Only the applied voltage behind the slots is capable of drastically reducing the charge density.

Figure 5 shows the computed charge density near the axis when a photoelectron rate of 0.001 photoelectrons per beamparticle per metre is assumed. Figure 6 shows the charge densities in the case of an unmodified LHC pipe, a slotted pipe with voltage behind, and the case of a pipe with unslotted electrodes directly on the beam pipes wall.

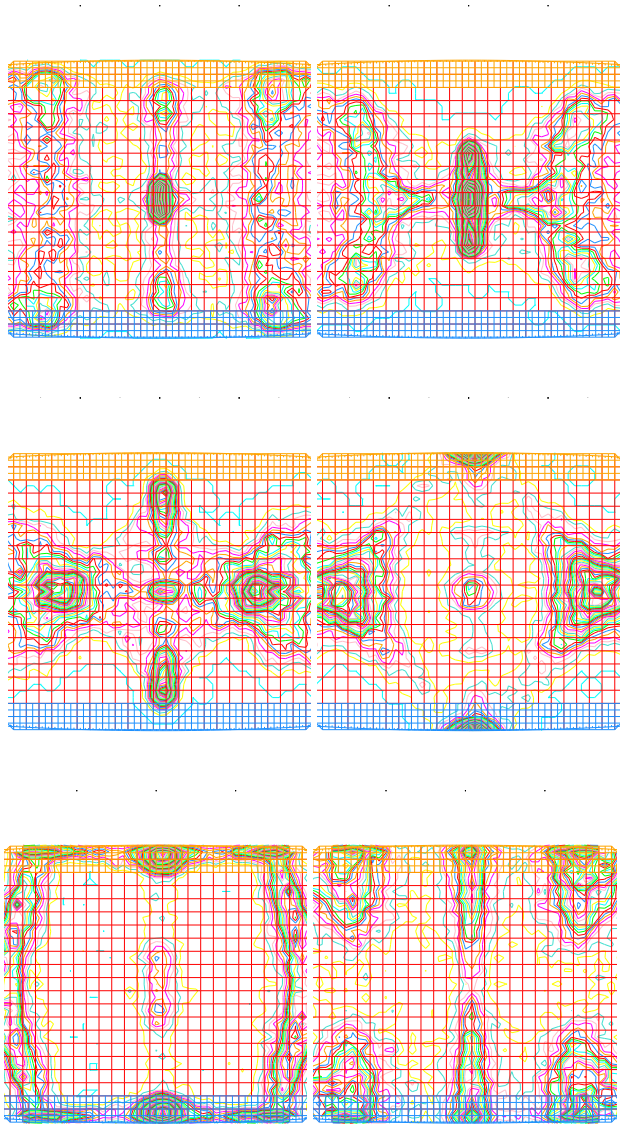

Figure 2: A zoom of the grid with charge densities at different times, just when a beam is passing. An elliptical beampipe with x-extension of $2 \times 7.6\mathrm{cm}$ and y-extension of $2 \times 1.75\mathrm{cm}$ is modeled. There are positively charged ions in the center. Above left: The electrons have just left the pipes boundary. Above right: The fast electrons have almost reached the center of the beampipe. Middle left: The slow electrons have reached the plane y=0, the fast electrons at x=0 have traversed the plane y=0 and are approaching the opposite wall. Middle right: The fastest electrons near x=0 have almost reached the opposite side of the beampipe, while the slower electrons have not yet reached the middle plane. Lower left: Almost all electrons have reached the opposite side. Last right: The electrons are diffusing back into the beampipe.

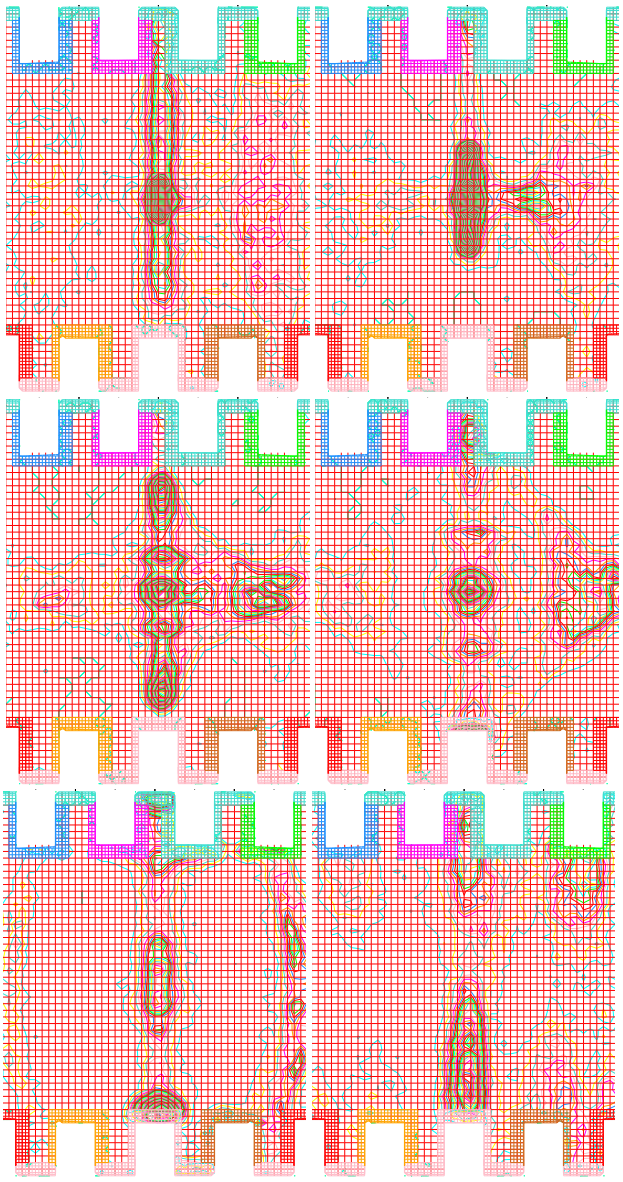

Figure 3: A zoom of the grid with charge densities at different times, just when a beam is passing. The dimensions of the beampipe are the same as the one shown in fig. 2. This beampipe additionally has slots at the upper and lower wall. Charges starting at the lower wall not within a slot experience the full acceleration of the passing positively charged beam. Because of the y-directed magnetic field, they move essentially in y direction. They end up within a slot on the opposite wall. Charges starting from within a slot experience only a fraction of the full acceleration and hit the opposite wall with a low energy. The times of the frames are the same as the ones in fig. 2. The total charge in the beampipe is a factor of 1000 lower than the charge in the pipe without slots.

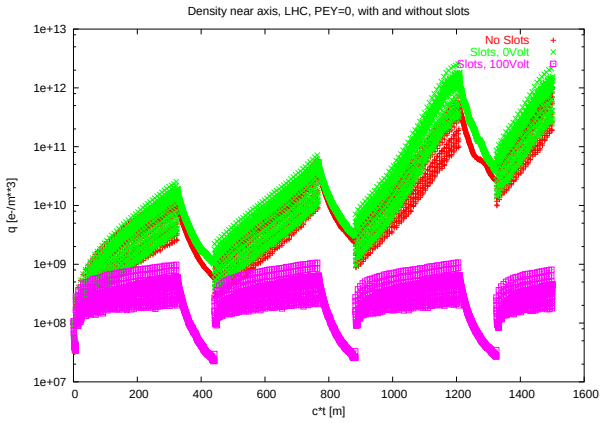

Figure 4: Charge density near the axis in a LHC like beampipe. No photoelectrons are considered. The primary electron creation is due to gasionisation with a probability of 0.25×10^{-6} pairs per bunchparticle per metre, which corresponds to 50 nTorr. The secondary emission yield is assumed to be 1.5 at 200 eV. Four passages of a train of 72 bunches followed by 21 emtpy bunches are simulated. The bunches have a distance of 7.48 metres and a population of 11.5×10^{10} positrons. The y-directed magnetic field has an amplitude of 1.8 Tesla. The red values are for a chamber without slots. The green values are for a slotted chamber, without a voltage behind the slots. The turqoise values are the results when behind the slots an electrode with +100 Volt is assumed.

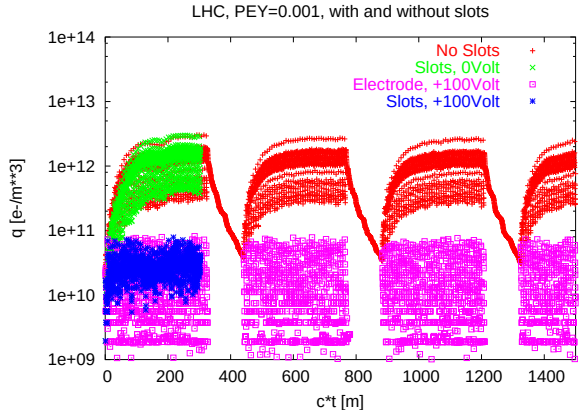

Figure 5: Charge density in a LHC like beampipe. The photoelectron rate is assumed to be 0.001 photelectrons per beam particle per metre. The red values are for a chamber without slots. The green values are for a slotted chamber,. Turoise: No slots, but electrodes at +100 volt at top and bottom. Blue: Slots, and electrodes at +100 volt behind the slots. All charge densities are much larger than the densities when no photoelectrons are considered.

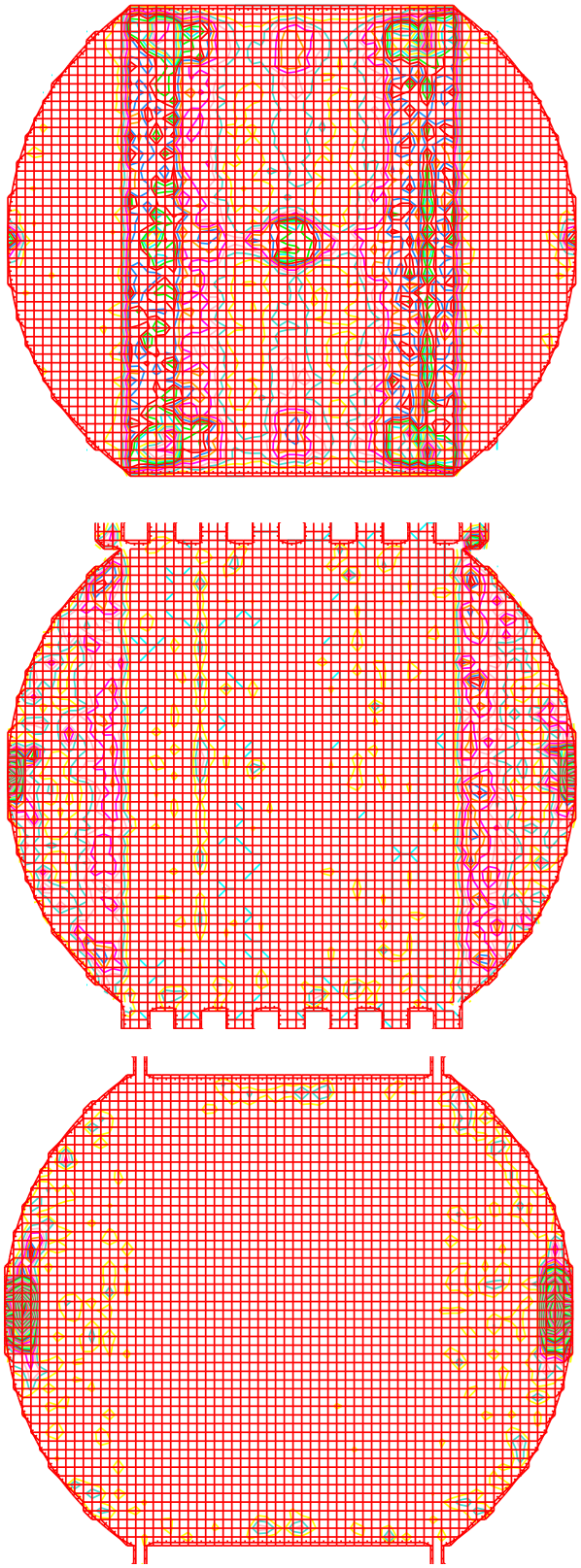

Figure 6: Charge densities in LHC-like beampipes. Above: No slots, no voltage applied. Middle: Slots, and 100 volts behind the slots applied. Below, no slots, but 100 volts applied at the lower an upper beampipes walls.

Results using coupled maps for electron and ion clouds in accelerators

U. Iriso* and S. Peggs§
*CELLS, PO Box 68, 08193 - Bellaterra, Spain
§Brookhaven National Laboratory, Upton, NY-11973 (USA)

Abstract

This article is a summary of the work presented in Refs. [1, 2]. In the following, we present the main topics discussed on them. For more information, see those articles and references therein.

INTRODUCTION

Dynamical models of cloud build-up, and of the phase transition from "cloud off" to "cloud on", are enhanced when simple coupling between electron and ion clouds is included. Maps are then capable of reproducing the first order phase transitions sometimes seen in practice. They also predict that hysteresis, period doubling, and chaotic phenomena may be observed.

MAPS FOR ELECTRON CLOUDS

For RHIC, it is found that the simulated evolution from the passage of bunch m to $m+1$ is empirically well represented by a cubic map [2, 3].

$$\rho_{m+1} \;=\; a\rho_m + b\rho_m^2 + c\rho_m^3 \;, \tag{1}$$

This result is also found for the LHC [4].

However, the map coefficients are inferred after fitting of the detailed computer simulation codes output, like ECLOUD or CSEC. Only the linear map coefficient is calculated from first principles, showing that it can be interpreted as the effective Secondary Emission Yield (SEY or δ) [2]:

$$a = \int_0^\infty \Big[\delta_r(E)^{n(E)} \;+ \\ +\; \delta_t(E)\delta_{\rm sec}^{\xi(E)}\; \frac{\delta_{\rm sec}^{n(E)\xi(E)} - \delta_r^{n(E)}}{\delta_{\rm sec}^{\xi(E)} - \delta_r(E)}\Big] h(E)\; dE \;, \tag{2}$$

where δ_r and δ_t are the reflected and true secondary electrons, $h(E)$ is the spectrum of the electron energy gain during the bunch passage, and $n(E)$ and $\xi(E)$ are two dimensionless parameters that account for the electron survival between two consecutive bunch passages.

EXPERIMENTAL OBSERVATIONS

Two puzzling observations at RHIC prompt us for the presence of ions during electron clouds. These are:

- "First and second order" phase transitions – pressure due to electron clouds shows an abrupt decay (first order phase transition) in one RHIC region, but is shows a smooth decay (second order) elsewhere, as the bunch intensity threshold for multipacting is crossed. Contemporary electron cloud simulation codes only reproduce the smooth decay [5].

- Vacuum instability driven by electron clouds – electron clouds and beam gas collisions create ions in a feedback process that leads to a vacuum instability [6].

But ion lifetimes ar between 3 to 6 order of magnitude larger than electrons, which imply a prohibitely large CPU times using detailed simulation codes (CSEC or ECLOUD). However, maps can be used to circunvent this limitation.

COUPLED ELECTRON AND ION CLOUDS MAPS

In a map model, the interplay between electron clouds and ion clouds is generally expressed by

$$\rho_{m+1} \;=\; f(\rho_m, R_m) \tag{3}$$
$$R_{m+1} \;=\; g(\rho_m, R_m) \;, \tag{4}$$

where R_m [nC/m] is the ion cloud density after the passage of the m'th bunch. (Both ρ and R are defined to be positive.) In the following, we use the vector $\vec{r}$ for the electron and ion densities

$$\vec{r}_m = \begin{pmatrix} \rho_m \\ R_m \end{pmatrix} \;. \tag{5}$$

The saturated electron and ion densities are found when an equilibrium is reached. The so-called fixed points are found when

$$\vec{r}_{\rm m+1} = \vec{r}_m \equiv \vec{r*} \;, \tag{6}$$

Furthermore, we need the fixed point to be *stable*. That is, small perturbations around the fixed point $\vec{r*}$ must result in an evolution that converges towards the fixed point. This depends on the trace and determinant of the Jacobian matrix, J:

$$J = \begin{pmatrix} \frac{\partial f}{\partial \rho_m} & \frac{\partial f}{\partial R_m} \\ \frac{\partial g}{\partial \rho_m} & \frac{\partial g}{\partial R_m} \end{pmatrix}_{\vec{r*}} \;, \tag{7}$$

References [1, 2] show the conditions that must follow the trace and determinant of the J to obtain stable or unstable fixed points.

RESULTS USING A NUMERICAL EXAMPLE

Results in [1] show that the final solution $\vec{r}^*$ for the electron and ion densities can depend on the initial conditions, which is the origin of the hysteresis effects and the first order phase transitions seen in practice. Results also predict that chaotic regimes may appear at or near machine operating conditions.

CONCLUSIONS

Maps are a suitable tool to overcome CPU limitations presented by a possible electron and ion cloud coupling. Using the maps formalism, the development of stability conditions for a broad spectrum of potential coupling mechanisms indicates that the final solution $\vec{r}^*$ can depend on the initial conditions (hysteresis). This brings up first order phase transitions, period doubling and the appearance of chaotic phenomena.

REFERENCES

[1] U. Iriso and S. Peggs. Maps for coupled electron and ion clouds in accelerators. Phys. Rev. ST Accel. Beams 9, 071002 (2006).

[2] U. Iriso, *Electron cloud at RHIC*, PhD Thesis in the Univ. de Barcelona (Spain), and BNL Techn. Note C-A/AP/228, Upton (USA), 2006.

[3] U. Iriso and S. Peggs, *Maps for electron clouds*, PRST-AB 8, 024403 (2005).

[4] T. Demma, S. Petraca, F. Ruggiero, G. Rumolo, and F. Zimmermann. *Maps for electron clouds: application to LHC*, TH-PCH047, Proc. of EPAC'06, Edinburgh, Scotland (2006).

[5] U. Iriso and S. Peggs, *Electron cloud phase transitions*, BNL Techn. Note C-AD/AP/147, Upton (USA), 2004.

[6] W. Fischer, U. Iriso, and E. Mustafin. *Electron Cloud driven vacuum instability*, Proc. of ICFA Workshop on High Intensity and High Brightness Hadron Beams, Bensheim (2004).

Extracting the electron-induced molecular desorption coefficient using an electron detector

U. Iriso* and W. Fischer§
*CELLS, PO Box 68, 08193 - Bellaterra, Spain
§Brookhaven National Laboratory, Upton, NY-11973 (USA)

Abstract

This article is a summary of the work presented in Refs. [1, 2]. In the following, we present the main topics discussed on them. For more information, see those articles and references therein.

INTRODUCTION

Valuable information can be extracted from the electron detectors, provided that they are properly calibrated. In this case, the extracted information is the electron flux into the wall and its energy spectrum. This allows to infer the electron-induced molecular desorption coefficient for both baked and unbaked stainless steel surfaces.

SYSTEM CALIBRATION

A significant number of electron detectors are installed in different machines to evaluate the electron cloud effects. However, often they are not properly calibrated and hence only qualitative information can be inferred.

This work enhances the usefulness of a proper calibration of the electron detectors. These calibrations are:

- Detector transparency – evaluate the ratio between the number of electrons at the collector plate and the number of electrons that hit the accelerator chamber wall.
- Bandwidth calibration – evaluate the effect of the system electronics and/or cable length.

These calibrations provide the electron flux to the wall for a given electron signal (typically, a voltage reading in the scope located at the service area). This information can then be used for:

- Calculation of important surface chamber parameters. For instance, using the electron flux to the wall and the pressure signal, the electron-induced molecular desorption coefficient can be inferred.
- Proper benchmark with the computer simulation codes.

ELECTRON-INDUCED MOLECULAR DESORPTION COEFFICIENT

The analysis of the experimental data in Refs. [1, 2] shows a linear relation between the pressure and the electron flux into the wall. For unbaked stainless steel and assuming CO as the only desorbed gas, this value is about 0.05 molecs/electron at the beginning of the run, and decreases to 0.01 after 6 weeks of machine operation due to scrubbing. For baked stainless steel, this value is around 0.005 molecs/electron.

ELECTRON ENERGY SPECTRUM DURING MULTIPACTING CONDITIONS

The desorption coefficient strongly depends on the striking electron energy at the beam-pipe wall. This is why a measurement of the electron energy spectrum is of great importance. References [1, 2] show that for unbaked stainless steel, a measure of the energy spectrum shows a large peak around 15 eV, and that the spectrum extends to at least 350 eV. The measurement is in a generally good agreement with the spectrum obtained using CSEC computer simulations.

CONCLUSIONS

A proper calibration of the electron detector allows to infer the electron flux into the wall, and using the pressure readings, the electron-induced desorption coefficient is inferred for baked and unbaked stainless steel surfaces at RHIC. Desorption coefficient for baked surfaces are about one order of magnitude lower than for unbaked surfaces, and results are consistent with laboratory measurements. The measurement of the electron energy spectrum peaks at about 15 eV and extends to about 300 eV, and are in a good agreement with computer simulation results.

REFERENCES

[1] U. Iriso and W. Fischer. Electron induced molecular desorption from electron clouds at the Relativistic Heavy Ion Collider. PRST-AB, 8, 113201 (2005).

[2] U. Iriso, PhD Thesis in the Universitat de Barcelona, Theory, observations, and simulations of the electron cloud at RHIC, to be publised, 2005.

Maps for Electron Cloud in LHC Dipoles

T. Demma, INFN-LNF, Frascati, Italy,
S. Petracca, University of Sannio, Benevento, Italy,
G. Rumolo, F. Zimmermann, CERN, Geneva, Switzerland.

Abstract

The cubic map formalism introduced in [1] to model electron cloud in RHIC is also reliable in the range of typical LHC parameters.

INTRODUCTION

The generation of a quasi-stationary electron cloud inside the beam pipe through beam-induced multipacting has become an area of intensive study. The analysis performed so far was based on very heavy computer simulations taking into account photoelectron production, secondary electron emission, electron dynamics, and space charge effects providing a very detailed description of the electron cloud evolution. In [1] it has been shown that, for the typical parameters of RHIC, the evolution of the electron cloud density can be followed from bunch to bunch introducing a cubic map with no constant term for the average line electron density between two successive bunches, ρ_l, whose coefficients are extrapolated from simulations and are function of the beam parameters and of the beam pipe characteristics. Simulations based on this map formalism are orders of magnitude faster than those based on usual codes. In this communication we show that this formalism is also reliable for the typical parameters of the LHC dipole bending magnet region [2].

BUILDING THE CUBIC MAP FOR LHC

We have followed the bunch to bunch evolution of the electron cloud density by averaging the output of the simulation code ECLOUD [3] between the end of a bunch and the start of the next bunch, using the typical parameters of an LHC dipole, varying the bunch population, from $0.8 \cdot 10^{11}$ to $1.6 \cdot 10^{11}$ protons per bunch, and the maximum secondary emission yield (SEY), from 1.2 to 1.7. We used the secondary emission yield curve model described in [4] scaled to an elastic reflection probability at zero electron energy of 0.5 instead of 1 [5]. The typical time evolution of the electron density is shown in Figure 1 for a train of 72 successive bunches followed by 28 empty bunches (bunches with a null bunch intensity, $N = 0$). The longitudinal electron density, as a function of time grows exponentially until the space charge due to the electrons themselves produces a saturation level. Once the saturation level is reached the average electron density does not change significantly. The final decay corresponds to the succession of the empty bunches. In Figure 1 one can see that the bunch-to-bunch evolution contains enough information about the build-up or the decay time, although the details of the line electron density oscillation between two bunches are lost. Figure 2 shows the average electron density, ρ_{m+1}, after

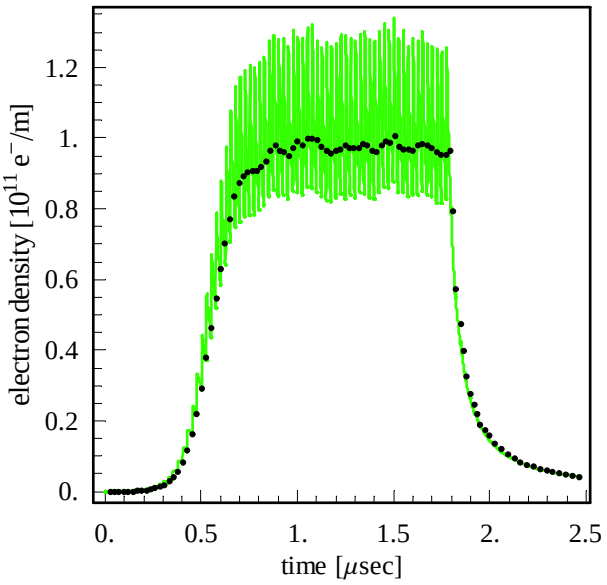

Figure 1: Time evolution of the electron density (green line) computed with ECLOUD. The case corresponds to the injection of 72 successive bunches with a bunch spacing of 25 ns, a bunch intensity of $N = 1.2 \cdot 10^{11}$ protons, and $\delta_{max} = 1.7$, followed by 28 empty bunches. The black dots mark the average electron density between two consecutive bunches.

the passage of bunch m as a function of the electron density, ρ_m, for different bunch intensities, N. The points in Fig. 2 show the average electron cloud density between two bunches using results from ECLOUD, the lines are cubic fits to these points. Figure 2 is explained as follows: starting with a small initial linear electron density, after some bunches the density takes off and reaches the corresponding saturation line ($\rho_{m+1} = \rho_m$, red line) where the space charge effects due to the electrons in the cloud itself take place. In this situation, all the points (corresponding to the passage of full bunches) are in the same spot. The chice of a cubic form for the map is explained as a consequence of the linear growth (this term has to be larger than unity in case of electron cloud formation), a parabolic decay due to space charge effects (this term has to be negative to give concavity to the curve ρ_{m+1} vs ρ_m), and a cubic term corresponding to perturbations. Neglecting the point

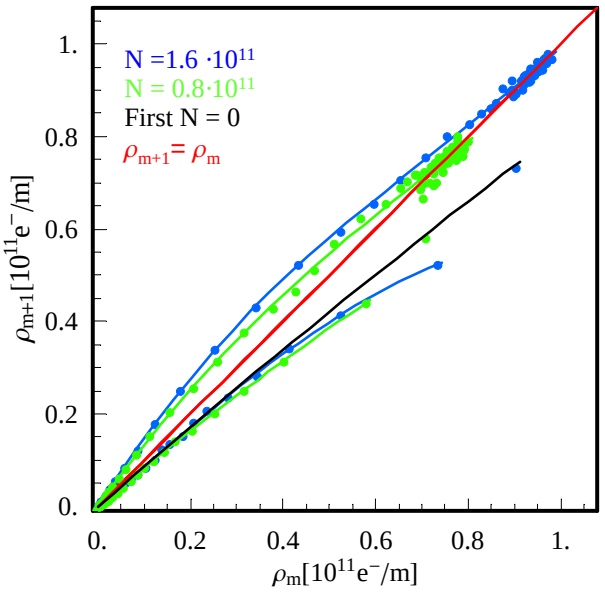

Figure 2: Average longitudinal electron density ρ_{m+1} after the passage of bunch m as a function of longitudinal electron density ρ_m before the passage of bunch m, for different bunch intensities ($N = 0.8 \cdot 10^{11}$ green, $N = 1.6 \cdot 10^{11}$ blue), and $\delta_{max} = 1.7$. The lines correspond to cubic fits applied to the average bunch to bunch points. The red line corresponds to the identity map $\rho_{m+1} = \rho_m$. Points above this line describe the initial growth and saturation of the bunch-to-bunch evolution of the line electron density, those below describe the decay. The black line represents the cubic fit to the points corresponding to the first empty bunches.

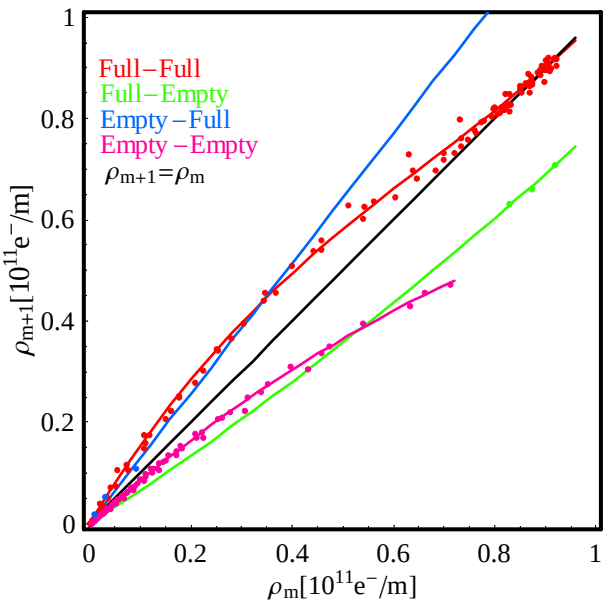

Figure 3: Average electron density ρ_{m+1} as a function of ρ_m, for the case of 24 bunches, 12 empty bunches, 36 bunches.The lines correspond to cubic fits applied to the four different cases: full bunch followed by another full bunch; full bunch followed by an empty bunch; empty bunch followed by a full bunch; empty bunch followed by another empty bunch.

corresponding to the electron cloud density after the first empty bunch, the longitudinal electron density follows a similar decay independently of the initial value of the saturated line electron density. The points corresponding to the first empty bunches coming from different saturation values lie on a general curve (black curve in Figure 2). Thus the electron density build up for a given bunch intensity is determined by a cubic form , while decay is described by two different cubic forms, one corresponding to the first empty bunch, and a second to the rest. The behavior of the map coefficients is not well understood and the determination of their values is purely empirical.

BUNCH PATTERNS

A possible application of the map formalism is in the search of the optimal distribution of bunches along the LHC circumference. A promising scheme to suppress the build up of the electron cloud is to increase the bunch spacing, or to introduce additional gaps in the bunch train [6]. The goal is to find out a bunch pattern using uneven bunch spacing around the LHC circumference that minimizes the electron cloud density. The nominal LHC beam consists of trains of 72 bunches, spaced by $25ns$, separated by a gap of 8 missing bunches. Several additional gaps can be easily introduced in the 72 bunch train, such as gaps of one or more trains of 12 missing bunches (e.g. cases like 24 bunches, 12 missing bunches, 36 bunches, or 12 bunches, 24 missing bunches, 36 bunches, etc.), obtaining a large number of different bunch filling patterns. Hence in order to determine the best filling pattern for a fixed set of beam pipe parameters, several simulation runs have to be launched for all the possible bunch filling patterns. The cubic map formalism can be used to reproduce the results. As it can be seen in Figure 3 where the bunch filling pattern (24 bunches, 12 missing bunches, 36 bunches) is reproduced, not only it takes two bunches to jump from the curve $N \neq 0$ to $N = 0$, but it also takes two bunches to jump from $N = 0$ to $N \neq 0$. Hence four different cubic form are needed to describe a particular bunch filling pattern. However the coefficients of these forms do not depend on the particular bunch pattern, and can be extrapolated from a single simulation for a fixed set of physical parameters. As an example in Figure 4 results are compared obtained by ECLOUD and the cubic map formalism using the coefficients extrapolated for the case (24 bunches, 12 missing bunches, 36 bunches), for different bunch filling patterns. In particular, regardless of the initial longitudinal electron density, the map results agree within an error range of 10% for all bunch filling patterns. The speed up in simulation time is several orders of magnitude (for the parameters used in these simulations, ECLOUD takes about

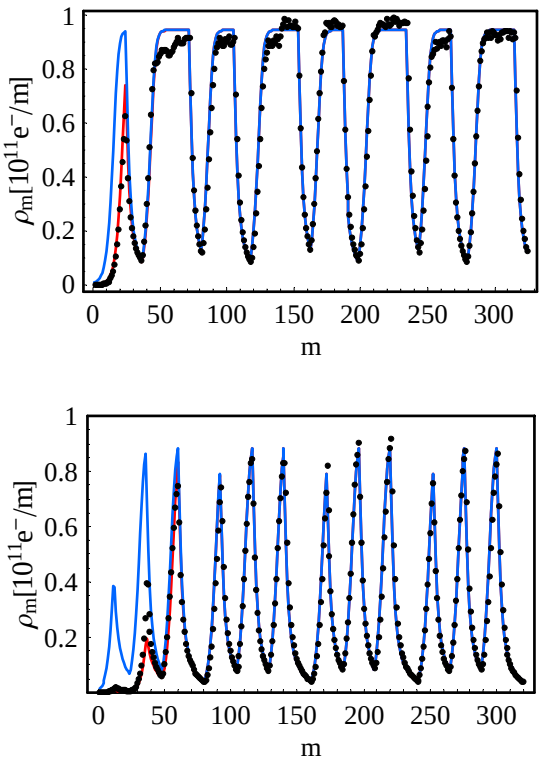

Figure 4: Electron cloud density evolution for two different bunch pattern (24 f.,12 e.,36 f. top, and 12 f.,12 e.,12 f.,12 e.,12 f.,12 e. bottom),for $N = 1.2 \cdot 10^{11}$ and $\delta_{max} = 1.7$, using ECLOUD (black dots) and cubic map with two different initial electron densities $\rho_0 = 10^{-2}\left[10^{11} \cdot e^-/m\right]$ (blue line) and $\rho_0 = 10^{-4}\left[10^{11} \cdot e^-/m\right]$ (red line).

12 h for each simulation run, the map only few milliseconds).

CONCLUSIONS AND OUTLOOK

The electron cloud build-up in an LHC dipole can be described using a cubic map. The coefficients of this map are functions of the pipe and beam parameters. This dependence can be extrapolated from simulation codes. For a given beam pipe and beam parameters the map coefficients are fixed and can be used to simulate the bunch to bunch evolution of electron cloud for different bunch filling patterns, obtaining a reduction of orders of magnitude of the simulation time. Another possible application of this formalism could be the construction of a map including the heat load. Deeper insight of the map formalism would be gained if a model of the dependence of the map coefficients on the physical parameters influencing the electron cloud were available. Work in this direction is in progress.

REFERENCES

[1] U.Iriso and S.Peggs, "Maps for Electron Clouds", Phys. Rev. ST-AB8, 024403, 2005.

[2] ,11. Th.Demma, S.Petracca, F.Ruggiero, G.Rumolo, F.Zimmermann, "Maps for Electron Clouds: Application To LHC", in Proceedings of the 2006 European Particle Accelerator Conference,p. 2889, 2006.

[3] http://wwwslap.cern.ch/electron-cloud/Programs/Ecloud/ecloud.html.

[4] R. Cimino et al., "Can low energy electrons affect high energy physics accelerators?", PRL93, 014801, 2004.

[5] D. Schulte et al., "Electron cloud measurements in the SPS in 2004", PAC-2005-FPAP014, 2005.

[6] R.Cappi et al., "Electron cloud buildup and related instability in the CERN Proton Synchrotron", Phys. Rev. ST-AB5, 094401, 2002.

SIMULATION PROGRESS AND PLANS AT ROSTOCK/DESY*

A. Markoviḱ, G. Pöplau, U. van Rienen, Rostock University, Germany
R. Wanzenberg, DESY, Germany

In this paper we give an overview over our algorithms developed for space charge calculations, the recently implemented tracking routines and our plans for electron cloud simulations.

Since 1999 fast algorithms for 3D space charge simulations, more precisely fast Poisson solvers, have been developed by G. Pöplau. Based on the multigrid technique these Poisson solvers have optimal performance, i.e. the numerical effort depends linearly on the number of macro particles. Another goal of these algorithms is that they are constructed for non-equidistant tensor product meshes which allows for instance a discretization of the bunch adapted to the distribution of the macro particles. The algorithms are available as software package MOEVE 2.0 (MOEVE: **M**ultigrid for n**o**n-**e**quidistant grids to sol**v**e Poisson's **e**quation) [7]. More precisely, MOEVE includes different iterative solvers: geometric multigrid (MG) and multigrid pre-conditioned conjugate gradients (MG-PCG), a pre-conditioned conjugate gradient method (PCG) with Jacobi pre-conditioner, (mainly for comparison reasons) the successive over relaxation (SOR), Biconjugated gradients (BiCG) and BiCGSTAB as stabilized version of BiCG. The algorithms of our software package we call MOEVE Poisson solvers in the following. The software package MOEVE contains three different types of boundary conditions: open boundary conditions, a perfectly conducting rectangular box and a perfectly conducting beam pipe with elliptical cross section, respectively.

Furthermore the MOEVE Poisson solvers are implemented in the tracking code GPT (General Particle Tracer) [14] of Pulsar Physics (Eindhoven, The Netherlands) and the tracking code ASTRA of K. Flöttmann (DESY, Hamburg) [3]. Simulations for the DC/RF gun at the TU Eindhoven were performed with GPT and the results are presented in [10, 12]. A tracking example with ASTRA can be found in [8].

For more details about the algorithms and the numerical results the reader is referred to the papers [8, 9, 10, 11, 12, 13, 15].

In 2005 R. Wanzenberg suggested to simulate electron cloud effects and to apply the MOEVE Poisson solvers for space charge calculations. Following this suggestion the first step was to implement algorithms for a beam pipe with elliptical cross section as boundary for the Poisson solver. This implementation was done by A. Markoviḱ [4]. It contains not only the adaption of the model to the elliptic shaped beam pipe but also the implementation of additional solvers for non-symmetric linear systems of equations. As a next step a tracking algorithm has been implemented.

A detailed description of the Poisson model for a beam pipe with elliptical cross section is given in [4]. As illustrated in [5, 6] the influence of different boundaries and boundary conditions on the space charge fields is not trivial especially if one observes the fields far from the beam axis and near the boundary. This certainly has a big importance for the simulation of the e-cloud build-up and its dynamics because different space charge fields could mean different energies and number of electrons in the cloud. Motivated by [1] the results of the solver on elliptical shaped domains are compared with the usually chosen open or Dirichlet boundaries on a rectangular box [5, 6].

Furthermore, in order to advance the charged particles in the presence of an electromagnetic (EM) field we have implemented the algorithm known as the Boris pusher [2]. It has been successfully implemented in many particle-in-cell (PIC) codes and the penalty for its parallelization is relative low. The EM fields are grid quantities while the quantities related to the particles (position and momentum) are stored with the particles which can be anywhere inside the computational domain. In order to update particle position and momentum, the EM fields on the grid are interpolated at the position of each particle. For the computation of the space charge fields the charge of the particles should be deposited on the grid points. When a particle hits the wall, the position, the incidence angle and the energy of the particle are known and can be used as an input to an e-cloud modelling routine. Although the electrons and the beam particles are defined in the same lab frame the space charge computation should be done separately for the two kinds of particles. For the relativistic beam particles the computational grid (in the rest frame) is stretched in longitudinal direction by the relativistic factor γ. The potentials computed from both kinds of particles are superposed on the grid in the lab frame.

Our plan for self-consistent beam-e-cloud simulations with focus on a single bunch instability is to have a full 3D computational domain around the bunch moving through the e-cloud in the lattice element of interest. Through the remaining part of the lattice the bunch should be mapped and transported to the next lattice element where it interacts with an e-cloud. After the first passage of the bunch through a certain lattice element the decay of the e-cloud in the element will be simulated and stored. The decay will be simulated over the time equal to the time distance between two neighboring bunches in the train. The presumption of a certain periodicity in the e-cloud decay allows to load the

* Work supported by DESY, Hamburg

stored e-cloud distribution after the decay for each further bunch passage.

REFERENCES

[1] E. Benedetto, D. Schulte, F. Zimmermann, and G. Rumolo. Simulation of Transverse Single Bunch Instabilities and Emittance Growth caused by Electron Cloud in LHC and SPS. *Proceedings of ECLOUD'04*, 2004.

[2] C.K. Birdsall and A.B. Langdon. *Plasma Physics via Computer Simulation*. The Adam Hilger Series on Plasma Physics, New York, 1991.

[3] K. Flöttmann. *ASTRA*. DESY, Hamburg, `www.desy.de/~mpyflo`, 2000.

[4] A. Markoviḱ. Numerical computation of space-charge fields of electron bunches in a beam pipe of elliptical shape. TESLA-Report 2005-21, DESY, Hamburg (`tesla.desy.de/new_pages/TESLA/TTFnot05.html`), 2005.

[5] A. Markoviḱ, G. Pöplau, U. van Rienen, and K. Flöttmann. Simulation of 3D space charge fields of bunches in a beam pipe of elliptical shape. In *Proceedings of EPAC 2006 (10th European Particle Accelerator Conference), Edinburgh, Great Britan*, pages 2200–2202, 2006.

[6] A. Markoviḱ, G. Pöplau, U. van Rienen, and R. Wanzenberg. Tracking code with 3-D space-charge calculations taking into account the elliptical shape of the beam pipe. In *Proceedings of ICAP 2006 (Proceedings of the 7th International Computational Accelerator Physics Conference), Chamonix Mont-Blanc, France*, pages 218–221, 2006.

[7] G. Pöplau. *MOEVE: Multigrid Poisson Solver for Non-Equidistant Tensor Product Meshes*. Universität Rostock, 2003.

[8] G. Pöplau, U. van Rienen, and K. Flöttmann. 3D space charge calculations for bunches in the tracking code Astra. In *Proceedings of EPAC 2006 (10th European Particle Accelerator Conference), Edinburgh, Great Britan*, pages 2203–2205, 2006.

[9] G. Pöplau, U. van Rienen, S.B. van der Geer, and M.J. de Loos. A fast 3D multigrid based space-charge routine in the GPT code. In *Proceedings of EPAC 2002 (8th European Particle Accelerator Conference), Paris, France*, pages 1658–1660, 2002.

[10] G. Pöplau, U. van Rienen, S.B. van der Geer, and M.J. de Loos. Multigrid algorithms for the fast calculation of space-charge effects in accelerator design. TESLA-Report 2003-31, DESY, Hamburg (`tesla.desy.de/new_pages/TESLA/TTFnot03.html`), 2003.

[11] G. Pöplau, U. van Rienen, S.B. van der Geer, and M.J. de Loos. Fast calculation of space charge in beam line tracking by multigrid techniques. In W.H.A. Schilders, E.J.W. ter Marten, and S.H.M. Houben, editors, *Scientific Computing in Electrical Engineering*, number 4 in Mathematics in Industry, pages 329–336, Berlin, 2004. Springer-Verlag.

[12] G. Pöplau, U. van Rienen, S.B. van der Geer, and M.J. de Loos. Multigrid algorithms for the fast calculation of space-charge effects in accelerator design. *IEEE Transactions on Magnetics*, 40(2):714–717, 2004.

[13] G. Pöplau, U. van Rienen, S.B. van der Geer, and M.J. de Loos. A multigrid based 3D space-charge routine in the tracking code GPT. In M. Berz and K. Makino, editors, *Computational Accelerator Physics 2002 (Proceedings of the 7th International Computational Accelerator Physics Conference, East Lansing, Michigan, USA)*, number 175 in Institute of Physics Conference Series, pages 281–288, Bristol and Philadelphia, 2005. Institute of Physics Publishing.

[14] Pulsar Physics, De Bongerd 23, 3762 XA Soest, The Netherlands, `www.pulsar.nl/gpt`. *General Particle Tracer (GPT)*, release 2.70.

[15] S.B. van der Geer, M.J. de Loos, O.J. Luiten, G. Pöplau, and U. van Rienen. 3D space-charge model for GPT simulations of high-brightness electron bunches. In M. Berz and K. Makino, editors, *Computational Accelerator Physics 2002 (Proceedings of the 7th International Computational Accelerator Physics Conference, East Lansing, Michigan, USA)*, number 175 in Institute of Physics Conference Series, pages 101–110, Bristol and Philadelphia, 2005. Institute of Physics Publishing.

*IMPACT OF ION CLEARING ELECTRODES ON BEAM DYNAMICS IN DAΦNE

M. Zobov, A. Battisti, A. Clozza, V. Lollo, C. Milardi,
B. Spataro, A. Stella, C. Vaccarezza, LNF-INFN, Frascati, Italy

* Work partly supported by the EC under the FP6 Research Infrastructure Action - Structuring the European Research Area EUROTeV DS Project Contract no.011899 RIDS

Abstract

Presently clearing electrodes are being considered as a possible cure of e-cloud driven problems in existing and future colliders. "Invisible" electrodes, made of a thin highly resistive layer pasted on a dielectric plate, have been proposed as one of design solutions for the e-cloud clearing. For the first time such electrodes were successfully used in the electron-positron accumulator (EPA) of LEP. Similar electrodes had been using for a long time for ion clearing purposes in the DAΦNE electron ring. Theoretical considerations and experimental measurements at DAΦNE have revealed a substantial contribution of the ion clearing electrodes (ICE) to the machine broad-band impedance giving rise to several harmful effects degrading the collider performance. In this paper we discuss the impact of the electrodes on DAΦNE beam dynamics, show the results of ICE wake field and impedance calculations and compare them with available experimental data. We also describe the procedure of ICE removal from the wiggler sections of the electron ring that has resulted in remarkable improvements in terms of beam dynamics and geometric luminosity.

1. INTRODUCTION

The Φ-factory DAΦNE [1] is an electron-positron collider at the energy of Φ resonance (1.02 GeV in the center of mass) designed and built in Frascati National Laboratories of INFN (see Fig. 1).

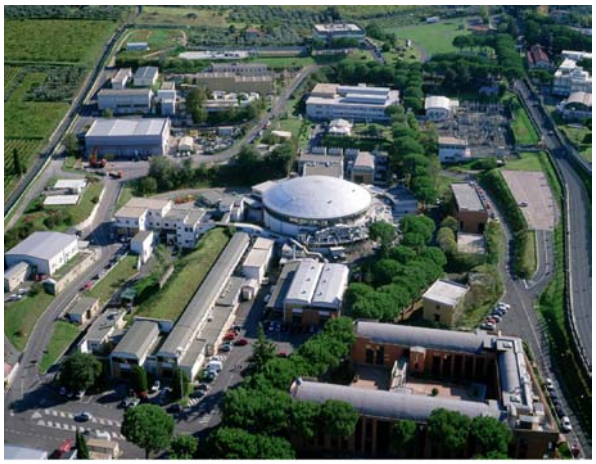

Fig. 1 View of DAΦNE accelerator complex.

The DAΦNE complex consists of two independent rings having two common interaction regions and an injection system composed of a full energy linear accelerator, a damping/accumulator ring and the relative transfer lines. The maximum peak luminosity obtained so far at DAΦNE is 1.6×10^{32} $cm^{-2}s^{-1}$, while the maximum daily integrated luminosity is 10 pb^{-1} [2]. Some of the main collider parameters are listed in Table 1.

In order to prevent accumulation of trapped ions in the electron beam potential several techniques were investigated. It was concluded that the DAΦNE start-up configuration requires a system of ion clearing electrodes (ICE) [3]. Because of the high circulating current stored in the electron multibunch beam (see Table 1) the Machine Advisory Committee suggested to use "invisible" electrodes similar to that proposed by F. Caspers [4] and already successfully used in the electron-positron accumulator (EPA) of CERN [5]. The principal goal of using such electrodes was to make them transparent for the beam as much as possible in order to:

- avoid the ICE to act as an antenna. Otherwise, the ICE would intercept a large fraction of the beam image current with a possible excessive power heating of the ICE themselves and an eventual damage of external feedthroughs and electronics;
- eliminate the resonant part of the beam coupling impedance arising from a mismatch between the ICE structures with the external feedthroughs and loadings. This is particularly important for the high current multibunch DAΦNE operations without coupled bunch instabilities.

Table 1: DAΦNE main parameters (KLOE run)

Energy [GeV]	0.51
Trajectory length [m]	97.69
RF frequency [MHz]	368.26
Harmonic number	120
Damping time, τ_E/τ_x [ms]	17.8/36.0
Bunch length [cm]	1-3
Number of colliding bunches	111
Beta functions β_x/β_y [m]	1.6/0.017
Emittance, ε_x [mm·mrad] (KLOE)	0.34
Coupling [%]	0.2-0.3
Max. tune shifts	0.03/0.04
Max. beam current e-/e+ [A]	2.4/1.4

However, during routine operations several effects harmful for the collider performance have been observed in beam dynamics of the electron beam. Similar effects have not been revealed or were less pronounced in the positron ring. Among the most offending effects are the following: strong lengthening of the electron bunches; lower microwave instability threshold; vertical beam size blow up depending on the bunch current and the RF voltage; quadrupole longitudinal bunch oscillations.

Since the vacuum chambers of the both rings are similar with the exception of the ICE in the electron ring, we have performed a more detailed study of the ICE coupling impedance including both numerical simulations and a comparison of the simulation results with available experimental data on bunch lengthening. These studies have led to the decision to remove the 2 m long ICE from the wiggler section vacuum chambers.

In this paper we describe our observations and experience in running DAΦNE with the ICE. In Section 2 we describe the DAΦNE ICE design while the principal harmful effects are summarized in Section 3. The results of the ICE impedance calculations and their experimental verification are discussed in Sections 4 and 5. Finally, Section 6 describes the wiggler section ICE removal procedure and shows some of the resulting improvements in beam dynamics and collider performance.

2. ICE DESIGN

For the "invisible" ICE a material with a high "resistivity per square" R_0 is required:

$$R_0 = \rho\frac{l}{S} = \rho\frac{l}{dl} = \frac{\rho}{d} \qquad (1)$$

As it is seen from (1), R_0 does not depend on the material length l and it should have a high resistivity ρ and a small thickness d. In this case we can expect that the skin depth δ_s will be much larger than the ICE thickness to provide the ICE transparency at RF frequencies.

The DAΦNE ICE are made of a highly resistive paste with a thickness d of 25 μm and the resistivity per square ρ/d of the order of 10^5 Ω painted on a dielectric material with ε = 9 (alumina). The skin depth estimated at a typical bunch spectrum frequency of 1 GHz is:

$$\delta_S = \sqrt{\frac{2\rho c}{Z_0\omega}} = 0.025m \rightarrow 1000d, \qquad (2)$$

where c is the velocity of light, Z_0 the free space impedance and ω the angular frequency, i.e. the skin depth is much larger than the layer thickness thus making the layer practically transparent for the RF frequencies.

The width of all ICE is about 5 cm, but their length and assembly designs depend on their locations along the ring. The electrodes in the straight sections having a round cross-section with a diameter of 88 mm are typically 10-12 cm long (see Fig. 2). The arc vacuum chambers are more complicated at it is seen in Fig.3. In the arcs there are short ICE installed in the bending magnet sections with the octagonal cross-section and the longest ICE placed in the very flat wiggler vacuum chambers (120 x 20 mm^2). The wiggler section ICE are 2.14 m long and stay very close to the beam trajectory, at about 1 cm distance.

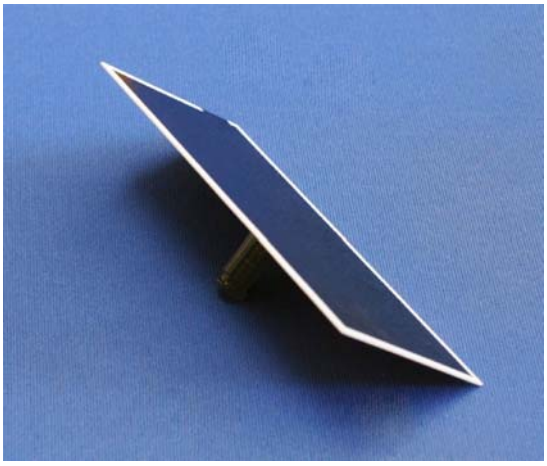

Fig. 2 Short ion clearing electrode located in straight sections.

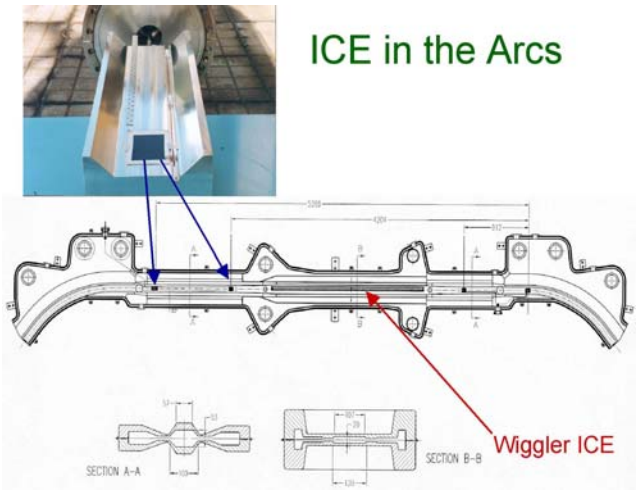

Fig. 3 The arc vacuum chamber with locations of short (bending section) and long (wiggler section) ion clearing electrodes

3. BEAM DYNAMICS WITH ICE

Beam measurements have shown that the beam coupling impedance of the two DAΦNE rings were different by approximately a factor of two [6]. The measured impedance of the positron ring is Z/n = 0.54 Ω to be compared with 1.1 Ω of the electron one. This difference produced several harmful consequences affecting the collider performance.

First, at the nominal bunch current of 20 mA the electron bunches were by about 30% longer than positron ones, as shown in Fig. 4. This immediately gives a geometric luminosity reduction due to the well-known hour-glass effect [7]. Moreover, in beam collision schemes with a horizontal crossing angle, as it is the DAΦNE case, synchro-betatron beam-beam resonances become stronger for longer bunches due to a higher

Piwinski angle, thus limiting the maximum achievable beam-beam tune shift parameter.

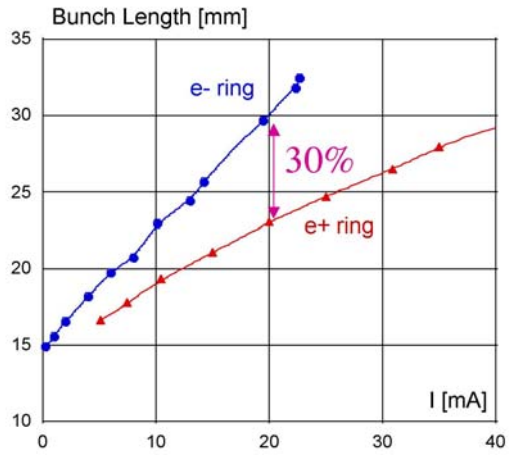

Fig. 4 Bunch length in the electron (blue) and positron (red) rings as a function of bunch current.

Second, the single bunch microwave instability threshold is inversely proportional to the coupling impedance. So, the electron bunches were suffering the instability at lower bunch currents. For DAΦNE the microwave instability leads not only to bunch energy spread widening, but also gives rise to quadrupole (bunch shape) oscillations. This kind of bunch behaviour has been predicted theoretically before DAΦNE commissioning [8] relying on the numerically calculated wake fields [9, 10]. For the positron ring the instability threshold stays above the nominal bunch current [8] while for the electron one it was observed for the currents as low as 9-10 mA in the normal operating conditions. There were several detrimental consequences of that:

- the injection saturation limiting the maximum electron beam current and, respectively, the collider luminosity;
- severe luminosity reduction since in collision the quadrupole oscillations induce additional beam-beam resonances resulting in the beam transverse blow up.

The problem of the quadrupole instability has been solved [11] by tuning the longitudinal feedback system in such way to kick differently heads and tails of bunches. Despite the world record current of 2.4 A has been stored in the DAΦNE electron ring after tuning, further improvements are still possible since in this manner the feedback was working ineffectively due to the necessity of damping at the same time the dipole and the quadrupole coupled bunch oscillations.

The third problem was the vertical beam size blow up (and also the horizontal one, although much weaker) beyond the microwave instability threshold. As shown in Fig. 5, the vertical blow up depends on both the bunch current and the RF voltage V_{RF}. At the nominal bunch current and the nominal RF voltage, a 60% blow up is observed even without beam-beam collisions. Besides, a strong correlation has been found between the transverse blow up and the lattice momentum compaction factor α_c [12]. In particular, the lower transverse blow up threshold has not allowed obtaining high luminosity in a collider lattice with a negative momentum compaction factor [13].

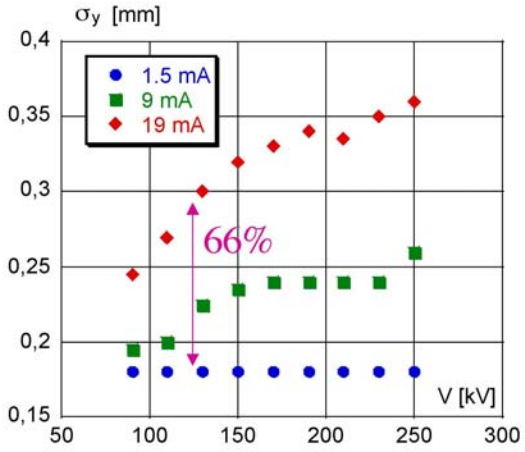

Fig. 5 The vertical beam size measured by the synchrotron light monitor as a function of RF voltage for three different bunch currents

Deeper studies have revealed that the transverse threshold scales accordingly to the Boussard criterion that is used for the longitudinal microwave instability threshold I_{th} estimates [14].

$$I_{th} = \frac{\sqrt{2\pi}\alpha_c (E/e)(\sigma_\varepsilon / E)^2 \sigma_{zo}}{|Z/n|R} \propto \frac{\alpha_c^{3/2}}{|Z/n|\sqrt{V_{RF}}} \qquad (3)$$

where E is the beam energy, σ_ε the rms energy spread at zero bunch current, σ_{z0} the natural bunch length and R the collider radius.

This has confirmed the dependence of the transverse effect on the longitudinal beam coupling impedance. The vertical size blow up was one of the main factors limiting the DAΦNE luminosity.

4. ICE IMPEDANCE

The vacuum chambers of the two DAΦNE rings are similar except for the ICE installed in the electron ring. For that reason and taking into account the relevant impact of the ring impedance on the collider performance we have undertaken more detailed numerical simulations of the ICE impedance [15, 16].

The calculations have shown that the ICE impedance:

- scales linearly with the electrode length L due to the dielectric electrode material;
- scales linearly with the electrode dielectric material thickness t;
- scales as a square root of the material dielectric constant ε.

It is worthwhile mentioning that the linear impedance dependence on the electrode length is not a surprise since it is well known that in dielectric channels the wake field builds up proportionally to the channel length. Namely this effect is used in dielectric wake field acceleration

experiments (see, for example, [17] and references therein).

It has also been found that the dominant impedance contribution comes from four ICE in the wiggler sections (2.1 m long and very close to the beam). The contribution of all the other ICE is almost negligible since they are much shorter than the wiggler ICE and are located at larger distances from the beam trajectory.

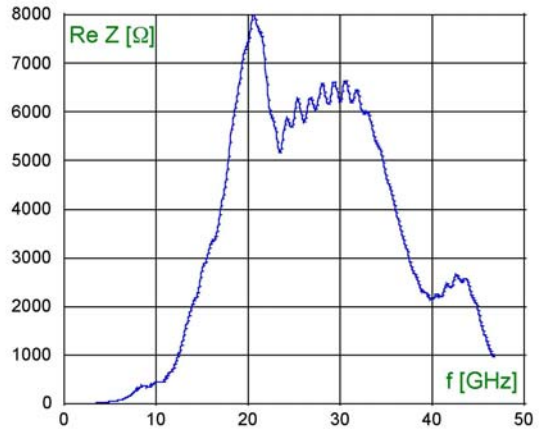

Fig. 6. Real part of the wiggler ICE impedance.

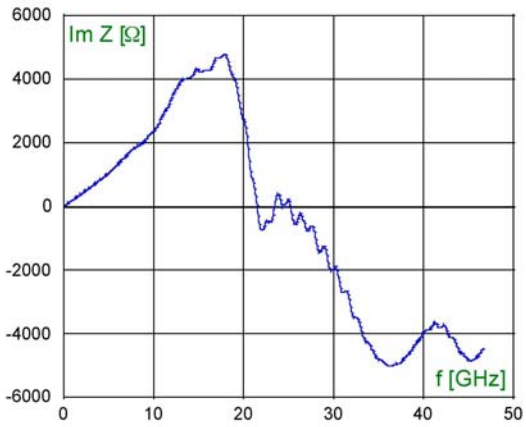

Fig. 7. Imaginary part of the wiggler ICE impedance.

Figure 6 and 7 show the real and the imaginary part of the coupling impedance calculated for the 4 ion clearing electrodes installed in the wiggler sections (4 wigglers per ring). As can be seen, the impedance:

- is broad-band;
- extends till rather high frequencies in the range of tens of GHz;
- is mostly inductive till about 10 GHz.

In turn, Figure 8 shows the respective normalized impedance defined as the beam coupling impedance divided by the revolution harmonic number $n = \omega/\omega o$, where ωo is the angular revolution frequency. The normalized impedance is almost constant over the large frequency range and accounts for half the electron ring impedance explaining the large impedance difference (about 0.6 Ω) between the electron and the positron DAΦNE rings.

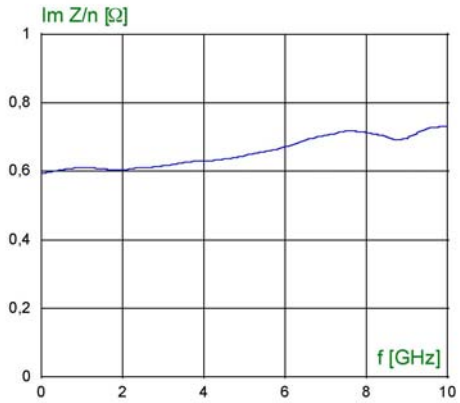

Fig. 8. Normalized impedance of the wiggler ICE.

5. BUNCH LENGTHENING IN ELECTRON RING

In order to check the results of the impedance calculations we have performed bunch lengthening simulations and compared their results with available experimental data.

To this purpose we have calculated the wake potential of the 4 wiggler section ICE for a 2.5 mm long Gaussian bunch. The required wake field of the electron ring has been obtained as the sum of the very well known [8] positron ring wake potential and the calculated wake potential of the ion clearing electrodes. In Fig.9 we plot together for comparison the e^- and e^+ ring wake potentials.

The above wake potential has been used as a pseudo Green function in the standard tracking code [10] in order to simulate bunch lengthening in the electron ring. Below we compare the tracking results with recent experimental data on the bunch lengthening in the electron ring lattice with negative and positive momentum compaction factors [12, 13].

For the lattice with positive momentum compaction factor the measurements and simulations have been carried out with $\alpha_c = 0.02$ and the RF voltage $V_{RF} = 135$ kV. For each bunch profile acquired by the streak camera and stored in the database we have calculated the rms bunch length. In this way the experimental data can be compared with the rms bunch length given by the simulations. As can be seen in Fig. 10 the agreement is quite satisfactory.

The same procedure has been performed for a lattice with negative momentum compaction factor $\alpha_c = -0.017$ and the RF voltage $V_{RF} = 165$ kV. The full width at half maximum (FWHM) of the longitudinal bunch distribution was measured at different bunch currents and, unfortunately, only a few beam profiles were stored during the measurements. So, in Fig.11 we plot the rms bunch length taken from the simulations and the FWHM/2.35 given by the measurements (we remind here

that for a Gaussian bunch FWHM/2.35 is equal to the rms). Only five points (green squares) correspond to the rms bunch length obtained by elaborating the stored bunch profiles. As can be seen in Fig. 11, both simulations and measurements predict the same microwave instability threshold that can be distinguished at the point where the bunch length has its minimum (at about 3 mA per bunch). Figure 12 shows measured and simulated bunch profiles at a bunch current of 7.8 mA.

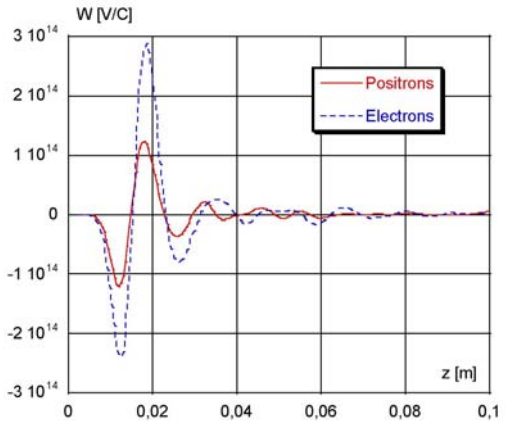

Fig.9. Wake potentials of a 2.5 mm Gaussian bunch for the positron (solid red line) and the electron (dashed blue line) rings.

6. ICE REMOVAL AND FIRST RESULTS

Considering the results of the impedance and wake field calculations and the satisfactory agreement between the bunch lengthening numerical tracking and the experimental bunch length measurements it has been decided to remove the ion clearing electrodes from the wiggler sections.

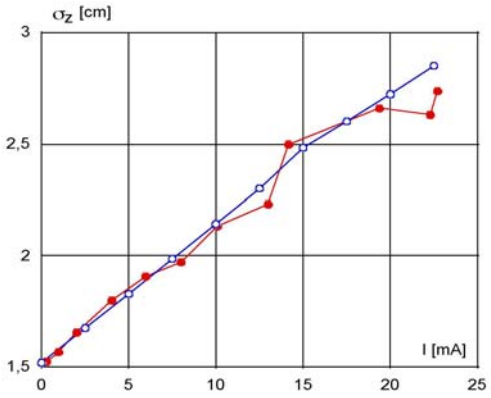

Fig.10. Bunch length in the lattice with positive momentum compaction factor as a function of bunch current: blue dots – numerical tracking; red dots – streak camera measurements.

We did not expect ion trapping worsening after the ICE removal since for the current DAΦNE operating configuration the horizontal emittance is by a factor 3 lower than that in the start-up configuration. Besides, the collider coupling is corrected by a factor 4-5 better with respect to the initial design value. In such conditions only a short gap in the bunch train is required (see Table 1) to expel ions from the electron beam potential.

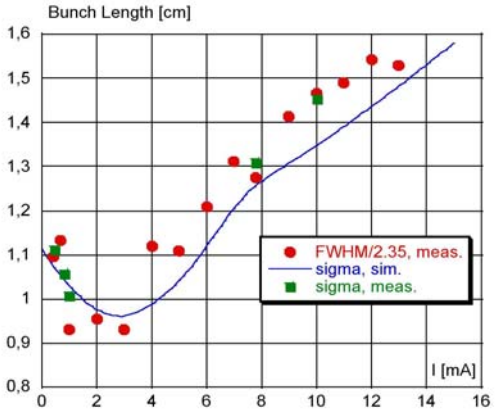

Fig.11. Bunch length in the lattice with negative momentum compaction factor as a function of bunch current: blue line – numerical tracking; red dots – streak camera measurements (FWHM/2.35); green squares – streak camera measurements (elaborated rms).

The ICE removal in-situ was not an easy task because of a limited accessible space overcrowded by other DAΦNE hardware and because of the complexity of the arc vacuum chambers (see Fig.3). The ICE were located in the narrowest part of the chamber which is only 2 cm wide.

In order to extract the ICE from that chamber and to cut the metallic fingers keeping them in place a special dedicated device remotely controlled through an endoscope has been designed and built [18] (see Fig. 13). A kind of a robot moving inside the narrow chamber and equipped with a milling device, a pneumatic piston and a suction cup has been used to both cut the fingers and to extract the electrodes.

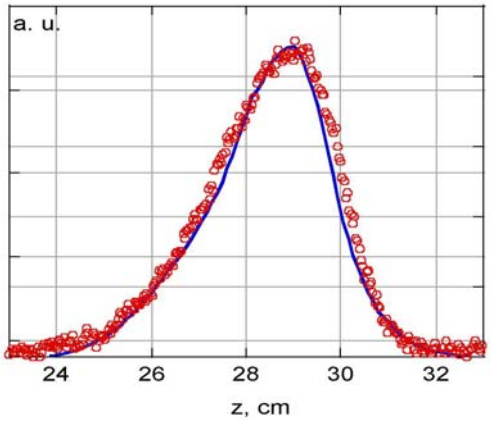

Fig.12. Bunch charge distribution in the lattice with negative momentum compaction factor measured at bunch current of 7.8 mA: red dots – streak camera measurements, blue line – numerical tracking.

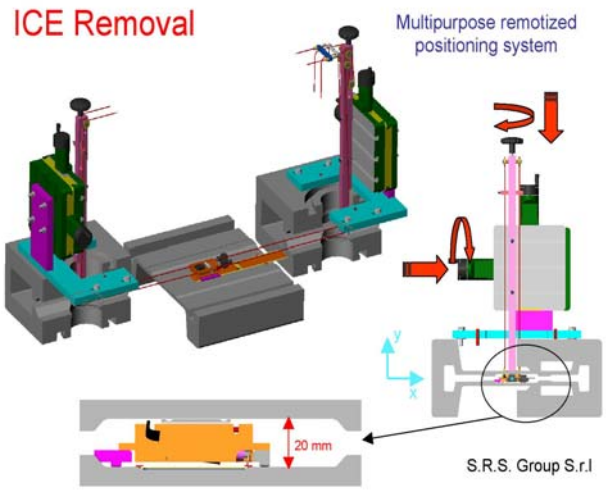

Fig.13. Sketch of the multipurpose remote positioning system used for ICE removal.

The 4 wiggler section ICE have been successfully removed and no vacuum problems have been encountered after DAΦNE re-commissioning. One of the 2 m long ICE is shown in Fig. 14. After the removal observations and measurements, while running the collider for the FINUDA experiment, have confirmed that the electron beam dynamics is now practically similar to that of the positron beam:

- the electron bunches are by about 25-30% shorter for DAΦNE operating conditions;
- the quadrupole instability threshold has been pushed beyond the operating bunch currents;
- no vertical beam size blow up has been observed for the whole range of operating bunch currents and RF voltages.

As can be seen in Fig. 15 in similar working conditions with the same lattice momentum compaction factor and RF voltage (130 kV) bunches are by 25% shorter. Moreover, now we can increase the RF voltage without vertical size blow up. This allows further bunch length reduction by increasing the RF voltage (see the red points at 180 kV, for example).

One of the most important results in terms of collider performance is the geometric luminosity enhancement. Its increase at present is estimated to be around 50%.

7. CONCLUSIONS

The experience in running DAΦNE with the "invisible" clearing electrodes has shown that despite the electrode highly resistive layer is transparent for RF frequencies the ICE give a high contribution to the broad-band coupling impedance due to the dielectric material of the electrode plates.

For the DAΦNE electron ring this resulted in several harmful effects: more pronounced bunch lengthening of the electron bunches, lower microwave instability threshold, vertical beam size blow up above the instability threshold and bunch longitudinal quadrupole oscillations.

The detailed wake field and impedance calculations and their experimental verification have revealed that the largest impedance contribution comes from the 4 long electrodes placed in the wiggler vacuum chambers. Their impedance accounts for half the total impedance budget of the electron ring.

The wiggler ICE removal has eliminated the above mentioned harmful effects for the whole range of typical collider operating parameters resulting in a geometric luminosity increase of about 50%.

Fig. 14 The ion clearing electrode removed from the wiggler vacuum chamber.

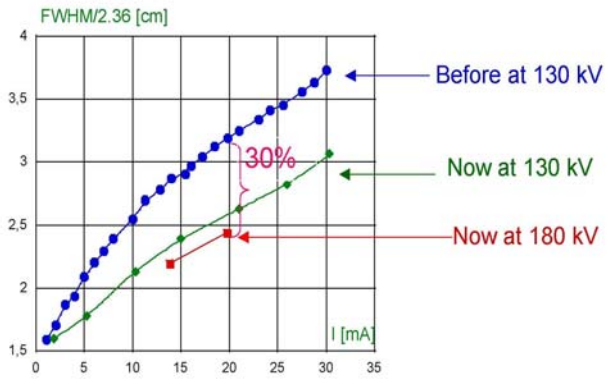

Fig.15 Bunch lengthening before (blue) and after (green) ICE removal. The two red points indicate further bunch length reduction at the higher RF voltage.

8. ACKNOWLEDGMENTS

We would like to thank Pantaleo Raimondi for bringing our attention to the ICE impedance problem and Claudio Sanelli for technical supervision of the ICE removal. We are also grateful to David Alesini, Alessandro Gallo and Alessandro Drago for many fruitful discussions and their help in some machine measurements. Eng. Manni is acknowledged for his help in designing the remote positioning system and in removal of the ICE.

9. REFERENCES

[1] G. Vignola, PAC93, p.1993;
also C. Milardi et al., Frascati Phys.Ser.16:75-84,1999.
[2] A. Gallo, EPAC06, p. 606.
[3] C. Vaccarezza, DAΦNE Technical Note: G-38, 1996.
[4] F. Caspers, IEEE Trans.Nucl.Sci.32:1914-1916,1985.
[5] F. Caspers et al., EPAC88, p.1324.
[6] A. Ghigo et al., EPAC02, p.1494.
[7] G. E. Fischer, SLAC report SPEAR-154, 1972.
[8] M. Zobov et al., e-Print Arxiv: physics/0312072.
[9] S. Bartalucci et al., NIM A337:231-241,1993.
[10] M. Zobov et al., LNF-95/041 (P), 1995.
[11] A. Drago, PRSTAB 6:052801, 2003.
[12] http://www.lnf.infn.it/acceleratori/dafne/report/High_momentumCompaction.pdf
[13] M. Zobov et al., e-Print Arxiv: physics/0607036.
[14] D. Boussard, CERN LABII/RF/INT/75-2, 1975.
[15] http://www.lnf.infn.it/acceleratori/dafne/report/Spataro_Zobov.pdf.
[16] B. Spataro, M. Zobov, DAΦNE Note:G-64, 2005.
[17] C.-B. Wang, J. Hirshfield, PRSTAB 9:031301, 2006.
[18] built by S.R.S. Group S.r.l.

ELECTRON CLOUD OBSERVATIONS AND CURES IN RHIC*

W. Fischer†, M. Blaskiewicz, H. Huang, H.-C. Hseuh, V. Ptitsyn, T. Roser, P. Thieberger,
D. Trbojevic, J. Wei, and S.Y. Zhang, BNL, Upton, NY 11973, USA
U. Iriso, CELLS-ALBA, Barcelona, Spain

Abstract

Since 2001 RHIC has experienced electron cloud effects, which have limited the beam intensity. These include dynamic pressure rises – including pressure instabilities, tune shifts, electrons, a reduction of the stability threshold for bunches crossing the transition energy, and possibly slow emittance growth. We summarize the main observations in operation and dedicated experiments, as well as countermeasures including baking, NEG coated warm beam pipes, solenoids, bunch patterns, anti-grazing rings, pre-pumped cold beam pipes, and scrubbing. This article is a condensed version of Ref. [1].

INTRODUCTION

The Relativistic Heavy Ion Collider (RHIC), in operation since 2000, has collided species from polarized protons, at energies up to 100 GeV, to gold ions, at energies up to 100 GeV/n. Since 2001 dynamic pressure rises were observed that limit the beam intensity. At that time the cause of the dynamic pressure rise was not known. As possible causes were considered: electron impact desorption after electron cloud formation, ion-impact desorption after rest-gas ionization and ion acceleration in the beam potential, and beam loss induced desorption [2]. It was later concluded that all operationally relevant pressure rises can be explained by electron clouds. Tab. 1 shows selected machine and beam parameters relevant to electron clouds for all species operated in RHIC so far.

Table 1: Main machine and beam parameters relevant to electron clouds for all species RHIC has operated with [3].

parameter	unit	Au	Cu	d	p
atomic number Z	...	79	29	1	1
mass number A	...	197	63	2	1
revolution time T_{rev}	μs	12.8			
harm. no. h, accel.	...	360			
harm. no. h, store	...	2520			360
full bunch length, inj.	ns	15			20
full bunch length, store	ns	5			10
no. of bunches N	...	up to 111			
bunch spacing t_b	...	multiples of 108 ns			
ions per bunch N_b	10^9	1.1	50	110	200

* Work performed under US DOE contract No DE-AC02-98CH1-886.
† Wolfram.Fischer@bnl.gov

OBSERVATIONS

Dynamic pressure rise

Dynamic pressure rise from electron-impact desorption after an electron cloud has been formed was the first, and still is the most common electron cloud observation in RHIC [2, 4, 5]. It is also the operationally most relevant electron cloud effect in RHIC. This pressure rise is particularly pronounced at transition crossing when the ion bunches are short [6, 7]. In some cases the electron cloud switched off spontaneously, like in a second order phase transition [8], which can be explained if the both and electron and ion cloud is assumed [9].

Pressure instabilities

In some instances pressure instabilities could be observed, where the pressure growths exponentially without bounds until the beam is aborted by the beam permit system. This occurred with gold beam, in unbaked locations, and after an electron cloud was formed. The formation of an electron cloud can be triggered after the bunch length is reduced, when, for example, bunches are transferred from the accelerating rf system into the storage rf system. An analysis shows that such an instability is possible for gases like CO [10, 11].

Tune shift

The observation of the coherent tune shift along a bunch train was the second electron cloud observation [12]. The sign of the observed tune shift in both planes is consistent with the existence of electron clouds, and the value of the tune shift allowed a first estimate of the electron cloud density, making comparisons with simulations possible [12, 13].

Electrons

Shortly after the first electron cloud observations were made, a number of electron detectors were installed [14, 15]. These allowed a direct observation of the electron cloud build-up, allowed correlations with the observed dynamic pressure rise, and were used to measure the energy distribution of the electrons in the cloud, and electron-impact desorption coefficients [16, 17].

Beam instabilities

In RHIC, all species, except protons, cross the transition energy. Because the main magnets are superconducting, their ramp rate is slow, and transition crossing is facilitated with a γ_t-jump of fast ramping quadrupoles. However, the short bunch length near transition can lead to instabilities. These are single bunch, transverse, and have growth times as low as 15 ms [18]. It was found that electron clouds, also enhanced by the short bunch length, can reduce the stability threshold. This manifests itself through increasing beam loss along the bunch train [19].

Emittance growth

Incoherent emittance growth from electron clouds was investigated in Refs. [20–22]. In the most recent polarized proton run, bunches shortened through rf quadrupole pumping in the AGS were injected into RHIC, in order to increase the luminosity through the reduction of the hourglass effect at store. However, the luminosity of the stores with bunches of reduced length was lower than the luminosity of stores with longer bunches of comparable intensity [23]. At the same time, a higher dynamic pressure was observed at injection. This could be an indication that electron clouds at injection have increased the proton beam emittance. In a separate test the emittance growth of proton bunches at injection was observed, and exceeded expectations from intra-beam scattering.

CURES

In-situ baking

The RHIC beam pipes in the warm regions are made of stainless steel 316LN. At the manufacturer the drawn tubes were detergent cleaned, water rinsed, acid prickled with HF+HNO_3, water rinsed again, annealed at 1050°C for 10 min, and then quenched. At BNL the pipes were cut to length, the end flanges welded, then baked under vacuum for 350°C for 24 h. Pipes for installation in magnets were leak checked and sealed before delivering to the magnet manufacturer.

Due to scheduling constraints the warm beam pipes were not baked in-situ initially. After the first dynamic pressure rises were observed, a program was started to bake in situ all warm pipes. With the exception of a few instruments, and the warm rf, this is possible at all other locations. This program yielded the first significant increase in the beam intensity.

NEG coating

To reduce the dynamic pressure rise, solenoids and NEG coated beam pipes were tested in small sections. For large scale installation in the warm beam pipes, NEG coating was chosen because, at comparable cost, the same or better electron cloud suppression was observed with NEG coating, which also provides distributed pumping [24,25]. Note that dynamic pressure rises is the main electron cloud effect in RHIC.

Solenoids

Up to 64 m of solenoids were installed for evaluation purposes. These showed a reduction of the observed electron cloud, and the pressure rise, at fields of 1.2 mT. However, the electron cloud could not be suppressed completely with fields up to 2.7 mT. Solenoids are still used near some experimental areas, and some equipment that cannot be baked at high temperature.

Bunch patterns

When machines are operated with less than the maximum number of bunches, the flexibility of rearranging the intensity in different bunch patterns can be used to minimize the electron cloud density. For the RHIC parameters we concluded that the electron cloud is minimized, and at the same time the luminosity maximized, when a given total intensity can be distributed in as few bunches as possible, which are uniformly distributed around the circumference [26]. This problem lends itself to analysis through maps for electron clouds [27]. Optimized bunch patterns were used in the RHIC runs in 2004 (Au-Au) and 2005 (Cu-Cu), when the number of bunches was reduced as more bunch intensity became available. These runs were limited by dynamic pressure rises in the PHOBOS experiment, that lead to unacceptable experimental background [8].

Anti-grazing rings

Lost beam particles hitting the beam pipe under a grazing incident angle, penetrate the beam pipe surface many times due to the surface roughness. This is expected to lead to electron and molecular desorption coefficients one to two orders of magnitude higher than for perpendicular impact. In Ref. [28] a mitigation was proposed by installing anti-grazing rings, through which all particles are lost with near perpendicular impact. Such grazing rings were installed in 2 sections in RHIC, and a reduction in the dynamic pressure rise could be observed [29]. However, for the grazing rings to be effective, they must intercept beam, which can lead to increased experimental background if they are close to a detector. With the large-scale installation of NEG coated beam pipes, currently, no anti-grazing rings are installed in RHIC.

Pre-pumping in cold sections

At high proton beam intensities an increase in the gas density in the cold sections was observed. The cold sections relied on cryo-pumping, and had been evacuated to about 10^{-1} Torr only in some areas, leading to up to 100 mono-layers of gas on the wall surface. After the observation of an increased gas density in the cold arcs, more pumps were installed in these regions, which evacuated the beam pipe to 10^{-6} to 10^{-7} Torr before cool-down of the

magnets, leading to much less than a mono-layer of gas on the cold beam pipe surface. With this no further increases in the gas density were observed.

Scrubbing

Scrubbing had been tested first in 2004 [30]. With scrubbing times of a few hours a reduction of the dynamic pressure rise by some 10% was observed in locations with the highest pressure. Scubbing is most efficient in locations with large dynamic pressure rises. At the beginning of the 2007 gold-gold run pressures up to 10^{-6} Torr were observed near the warm rf and a few other locations that can not be baked at high temperature. Two hours of scrubbing at injection with the highest available ion intensities, and seven fills, reduced the dynamic pressure by approximately one order of magnitude at the locations with the highest pressure.

ACKNOWLEDGMENTS

The authors are thankful for support to the members of the vacuum and accelerator physics groups. Many people from other laboratories were helpful in discussions, in particular V. Bagelin, M. Furman, M. Jimenez, A. Krämer, E. Mahner, E. Mustafin, A. Molvik, G. Rumolo, J.-L. Vay, and F. Zimmermann.

REFERENCES

[1] W. Fischer et al., proceeding ECLOUD'07 Workshop, Daegu, Korea (2007).

[2] W. Fischer et al., proceedings EPAC'02, Paris, France (2002).

[3] W. Fischer, http://www.agsrhichome.bnl.gov/RHIC/Runs/ (2007).

[4] U. Iriso et al., proceedings EPAC'04, Lucern, Switzerland (2004).

[5] S.Y. Zhang et al., proceedings PAC'05, Knoxville, TN (2005).

[6] W. Fischer and U. Iriso, BNL C-A/AP/184 (2004).

[7] S.Y. Zhang, BNL C-A/AP/198 (2005).

[8] G. Rumolo and W. Fischer, BNL C-A/AP/146 (2004).

[9] U. Iriso and S. Peggs, Phys. Rev. ST - Accel. Beams **9**, 071002 (2006).

[10] W. Fischer, U. Iriso, and E. Mustafi n, proceedings 33rd ICFA Beam Dynamics Workshop on High Intensity and High Brightness Beams, Bensheim, Germany, AIP Conference Proceedings 773 (2004).

[11] S.Y. Zhang, BNL C-A/AP/190 (2005).

[12] W. Fischer, J.M. Brennan, M. Blaskiewicz, and T. Satogata, Phys. Rev. ST Accel. Beams 5, 124401 (2002).

[13] M. Blaskiewicz and U. Iriso, BNL C-A/AP/260 (2006).

[14] U. Iriso, Ph.D. thesis, University of Barcelona, BNL C-A/AP/228 (2006).

[15] U. Iriso et al., PAC'03, Portland, OR (2003).

[16] U. Iriso and W. Fischer, Phys. Rev. ST - Accel. Beams **8**, 113201 (2005).

[17] U. Iriso and W. Fischer, Phys. Rev. ST - Accel. Beams **9**, 029901 (2005).

[18] M. Blaskiewicz et al., proceeding PAC'03, Portland, OR (2003).

[19] J. Wei et al., proceedings of the 39th ICFA Advanced Beam Dynamics Workshop on High Intensity High Brightness Hadron Beams HB2006, Tsukuba, Japan (2006).

[20] E. Benedetto, D. Schulte, F. Zimmermann, and G. Rumolo, Accel. Beams **8**, 124402 (2005).

[21] E. Benedetto, G. Franchetti, and F. Zimmermann, PRL **97**, 034801 (2006).

[22] K. Ohmi and K. Oide, Phys. Rev. ST - Accel. Beams **10**, 014401 (2007).

[23] S.Y. Zhang and V. Ptitsyn, BNL C-A/AP/257 (2006).

[24] S.Y. Zhang, H.C. Hseuh, W. Fischer, H. Huang, T. Roser, BNL C-A/AP/220 (2005).

[25] S.Y. Zhang et al., proceedings EPAC'06 (2006).

[26] W. Fischer and U. Iriso, proceedings EPAC'04 (2004).

[27] U. Iriso and S. Peggs, Phys. Rev. ST - Accel. Beams **8**, 024403 (2005).

[28] P. Thieberger, W. Fischer, H.C. Hseuh, V. Ptitsyn, L.P. Snydstrup, D. Trbojevic, and S.Y. Zhang, Phys. Rev. ST - Accel. Beams **7**, 093201 (2004).

[29] S.Y. Zhang, H.C. Hseuh, P. Thieberger, D. Trbojevic, Phys. Rev. ST - Accel. Beams **8**, 123201 (2005).

[30] S.Y. Zhang, et al., proceedings EPAC'04 (2004).

Beam heat load in the ANKA superconducting undulator

S. Casalbuoni*, A. Grau, M. Hagelstein, R. Rossmanith,
Forschungszentrum Karlsruhe, Karlsruhe, Germany
F. Zimmermann, CERN, Geneva, Switzerland,
B. Kostka, E. Mashkina, E. Steffens, University of Erlangen, Erlangen, Germany
A. Bernhard, D. Wollmann, T. Baumbach, University of Karlsruhe, Karlsruhe, Germany

Abstract

The beam heat load in the cold bore superconductive undulator installed at ANKA has been monitored for almost two years. The possible sources of the observed heat load as synchrotron radiation from upstream magnets, image currents, electron and ion bombardment are here discussed and compared with the experimental results.

INTRODUCTION

Conventional undulators are built with permanent magnets. The advantage of superconducting undulators is that for the same gap and same period length they produce higher fields. This technological solution is very interesting for synchrotron light sources since it permits to increase the brilliance [1, 2] at relatively low costs. Superconducting undulator technology has also recently been acknowledged by the high energy particle physics comunity to be the most promising solution for the CLIC damping wiggler [3] and for the ILC positron source [4]. However superconducting undulator technology is not yet mature. One of the key issues is the understanding of the beam heat load to the cold vacuum chamber. In this paper we present beam heat load measurements performed at the synchrotron light source ANKA in the superconducting cold bore undulator operating in the ring since March 2005.

EXPERIMENTAL SETUP

ANKA is an electron storage ring used as a synchrotron facility [5]. The maximum achievable energy is 2.5 GeV and the maximum current is 200 mA. The revolution time is $T_r = 368$ ns and the machine is normally operated with two trains, each composed of 32 bunches separated by 2 ns. The cold bore superconducting undulator built by ACCEL Instr. GmbH, Bergish, Gladbach, Germany [6], is installed in one of the four straight sections of the ring, see Fig. 1: the rest of the ring is warm. The vacuum chambers of the warm part of ANKA have been "prebaked ": before installation they have been baked at 200^{o}C for 48 hours and vented with nitrogen. The storage ring compatible cryostat is shown in Fig. 2. The system is cryogen free and is cooled by three Sumitomo cryocoolers (RDK-408D @ 50 Hz) [7]: two of them are cooling the coils to about 4 K and one the UHV tank, which is at 10 K and protects the coils from the external thermal radiation. The cryostat consists of two

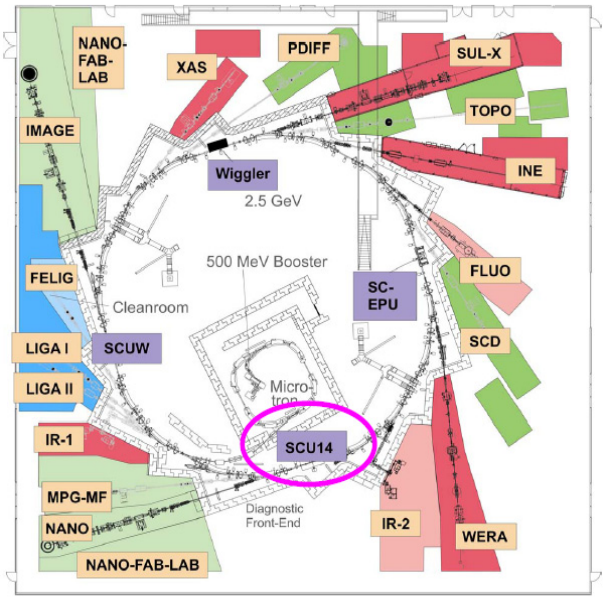

Figure 1: The synchrotron radiation facility ANKA.

separated vacuum systems for the cold mass: an UHV (Ultra High Vacuum) vacuum system for the beam and an insulation vacuum system for the coils and the rest of the cold mass. The pressure of the two vacua are monitored. A 300 μm stainless steel foil coated with 30 μm of copper is placed between the cold mass and the beam vacuum. A taper system connects the normal beam pipe with the cold mass and has two functions: 1) smooth transition for wake fields, 2) thermal transition between the cold bore at 4 K and the beam pipe at room temperature. Several temperature sensors are placed on the different elements: coils, UHV tank, taper entrance, taper exit, etc. The undulator can be operated at different gap sizes: 16, 12, and 8 mm. The undulator gap can be opened to 29 mm without current in the coils during injection. Some of the parameters of the electron beam, the storage ring and the superconducting undulator are summarized in Table 1. In order to protect the undulator from the synchrotron radiation emitted by the upstream magnets a collimator system is located at about 1 m from the entry point of the undulator [8].

POSSIBLE HEAT LOAD SOURCES

Possible heating mechanisms are: 1) synchrotron radiation from upstream magnets, 2) high frequency image currents on the cold surface also called resistive wall heating,

* sara.casalbuoni@iss.fzk.de

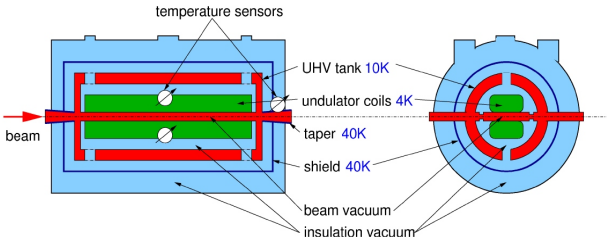

Figure 2: Schematic layout of the vacuum system of the superconducting undulator and the position of the temperature sensors.

Electron beam	
E_{max}	2.5 GeV
I_{max}	200 mA
Storage ring	
Circumference	110.4 m
Cavity frequency	499.66 MHz
T_{rev}	368 ns
Undulator	
Length	1.4 m
Periods	100
Magnetic gap	8,12, 16 mm
Beam stay clear gap	29 mm
Maximum magnetic field at 8 mm gap	0.8 T

Table 1: Electron beam, storage ring and superconducting undulator parameters.

3) ions and electrons accelerated to the walls by the transverse field of the ultrarelativistic beam. Knowing how the different heat load sources scale with the different beam parameters as the energy E, the average beam current I, the total number of bunches M, the bunch length σ_z and measuring the beam heat load varying the above mentioned parameters allows one to distinguish between the different heating mechanisms.

Heat load from synchrotron radiation

Synchrotron radiation losses are given by [9]:

$$P_{synch} = \int_{\psi_0}^{\psi_1} P_0 \frac{21}{32} \frac{\gamma}{(1+\gamma^2\psi^2)^{5/2}} \left[1+\frac{5}{7}\frac{\gamma^2\psi^2}{(1+\gamma^2\psi^2)}\right] d\psi \quad (1)$$

where ψ is the vertical opening angle between the tangent of motion in the horizontal plane and the plane of interest, ψ_0 and ψ_1 are the lower and upper values of ψ determined by the distance of the bending magnet to the undulator and by the gap, $\gamma = E/m_e c^2$, $P_0 = \frac{eI}{10^3 6\pi\epsilon_0}\frac{E^4}{\rho(m_e c^4)^4}$ is the total radiated power per mrad of arc integrated over all vertical angles, e is the electron charge, I is the average beam current, ϵ_0 is the vacuum permittivity, E is the beam energy, ρ is the radius of curvature of the electron trajectory in the bending magnet, m_e is the electron mass and c is the velocity of light.

Heat load from resistive wall effect

The resistive wall heating losses per unit length can be calculated by [10]:

$$P_{RWH} = \frac{I^2}{M f_0 \pi^2 g} \int_0^\infty S^2(\omega) R_{surf}(\omega) d\omega \quad \text{[W/m]} \quad (2)$$

where I is the average beam current, M is the number of bunches, f_0 the revolution frequency and g is the gap (an equivalent formula is given in Ref. [9]). $S(\omega)$ is the bunch spectrum. Assuming a bunch with Gaussian shape and length σ_z, $S(\omega) = e^{-\frac{\sigma_z^2\omega^2}{2c^2}}$. $R_{surf}(\omega)$ is the surface resistance. The vacuum chamber is made of a 300 μm layer of stainless steel electroplated with 30 μm of copper. Electroplated copper has usually a Residual Resistivity Ratio (RRR) in the range between 10 and 100 [9]. For copper at low temperature and $RRR > 7$ we are in the regime of the anomalous skin effect [9, 10, 11] and:

$$R_{surf}(\omega) = R_\infty(\omega)(1 + 1.157\alpha^{-0.276}), \quad \text{for } \alpha \geq 3 \quad (3)$$

with $\alpha = \frac{3}{2}(\frac{\ell}{\delta(\omega)})^2 = \frac{3}{4}\mu_r\mu_0\sigma\omega\ell^2$ where ℓ is the mean free path, $\delta(\omega) = \sqrt{\frac{2}{\mu_r\mu_0\sigma\omega}}$ the skin depth, μ_r the relative permeability, μ_0 the vacuum permeability and σ the electrical conductivity, and with $R_\infty(\omega) = (\frac{\sqrt{3}}{16\pi}\frac{\ell}{\sigma}(\mu_r\mu_0\omega)^2)^{1/3}$.

Synchrotron radiation losses increase linearly with the average beam current, while resistive wall heating losses scale as I^2/M and strongly depend on the bunch length σ_z.

Heat load from electron and ion bombardment

A naive model of heat load due to electron and ion bombardment is described below. A charged particle with mass m and charge q in the vacuum chamber can be accelerated by the transverse electric field carried by the ultrarelativistic bunch:

$$E(r) = \frac{\lambda}{2\pi\epsilon_0 r} \quad (4)$$

where λ is the line charge of the bunch, $\lambda = \frac{eN_b}{c\tau}$ and τ is the bunch duration and N_b the particles per bunch $N_b = \frac{IT_r}{eM}$ with T_r the revolution time [12]. The momentum transfer by one bunch to a stationary electron at radial position r is

$$\Delta p = qE(r)\tau = \frac{qeN_b}{2\pi\epsilon_0 cr} \quad (5)$$

and the corresponding energy increase:

$$\Delta W = \frac{\Delta p^2}{2m} = \frac{\left(\frac{qeN_b}{2\pi\epsilon_0 cr}\right)^2}{2m}. \quad (6)$$

Roughly, the power is the energy gained by the charged particle ΔW times the number of charged particles accelerated to the wall per unit time $\dot{\Gamma}$:

$$P_{el} = \Delta W \cdot \dot{\Gamma} \quad (7)$$

Since the energy ΔW is inversely proportional to the mass of the particle m the ion contribution can be neglected, see Eq. (6). It is then known how the energy gain scales with the different beam parameters. A possible source of electrons is the condensed gas layer physisorbed on the surface. In the gas layer the molecules are loosely bound (binding energy $\approx$ few meV) by Van der Waals forces (see Fig. 3). The gas layer is formed at low temperatures. Energetic particles first hit the surface oxide layer of the vacuum chamber and part of the gases are desorbed. Then the desorbed gases recondense on the surface, so that the energetic particles will after hit the condensed gas layer where the molecules are loosely bound and this can be a source of electrons. Since the molecules forming the condensed gas layer have already been desorbed this phenomenon is usually refered in the literature as "recycling"(see for example Ref. [13]). Our vacuum chamber is very similar to the LHC beam screen (300 μm stainless steel with 30 μm of electroplated copper). For such a chamber the dominating desorbed gases are H_2, CH_4, CO, CO_2 and H_2O. Of these only H_2 has a non negligible vapour pressure at 4-20 K. The plot in Fig. 4 from Ref. [15] shows the adsorption isotherm of H_2 at 4.2 K, that is the density of H_2 molecules in gas form n, corresponding to the equilibrium pressure measured at room temperature $P_{UHV} = n(\text{mol/cm}^3) \cdot 4.9 \cdot 10^{-18}$ mbar [15] as a function of the H_2 surface coverage s. The adsorption isotherm varies with many parameters as the molecular species present in the surface oxide, on the surface temperature, on the nature of the surface oxide and on the gas composition inside the chamber. In the vacuum chamber of the superconducting undulator the equilibrium pressure is about $2 - 5 \cdot 10^{-11}$ mbar, which corresponds to 10^{15} H_2 molecules per cm^2. Considering the geometry of our vacuum chamber we can calculate the number of H_2 molecules on the surface and in the volume. At the surface we have $N_{Surf} \approx 10^{17}$ and in the volume, considering $P_{UHV} = 10^{-11}$ mbar, $N_{Vol} \approx 5 \cdot 10^{10}$. At the surface there are more than one milion times molecules than in the volume: the surface is a huge electron reservoir. The mass

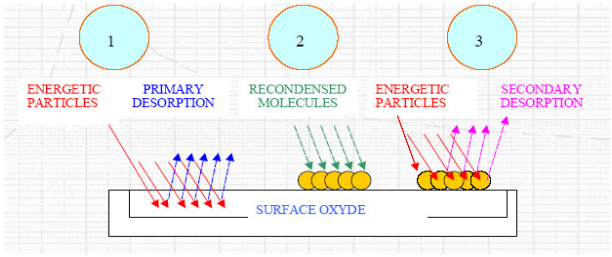

Figure 3: Scheme of the desorption process on a cold surface. After N. Hilleret [14].

spectrum of the warm vacuum chamber just before the undulator with beam detects only H_2 and CO, see Fig 5. CO disappears when there is no beam: this is an indication of the dynamic of the desorption and recycling process discussed above. In the rest of the ring most of the time no

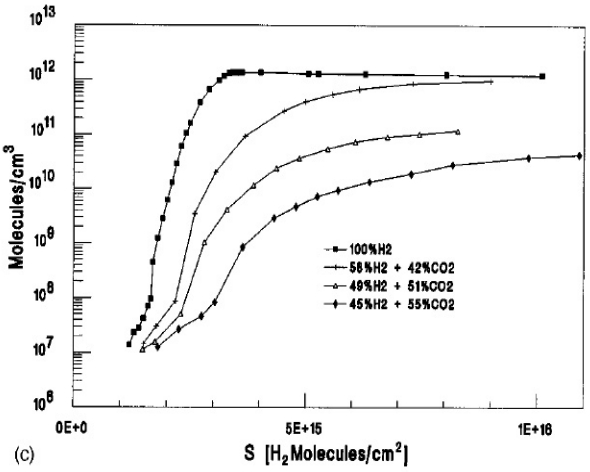

Figure 4: Isotherms of coadsorption of H_2 and CO_2 on Cu plated stainless steel at 4.2 K, plotted as a function of the surface density of H_2 molecules. After E. Wallén [15].

CO is detected.

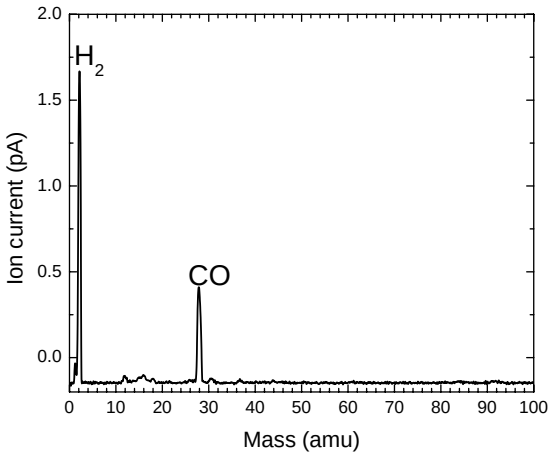

Figure 5: Mass spectrum of the warm vacuum chamber just before the undulator with beam.

RESULTS

Beam induced heat load during normal beam operation

Fig. 6 shows the average beam current, the beam energy, the UHV pressure and the temperature of the coils as a function of time during user operation in a time range of 2 weeks. The increase in temperature to the coils can be converted into the deposited beam heat load. The calibration has been performed using a resistor in thermal contact with the coils. The time constant to reach thermal equilibrium is of the order of two hours. The beam heat load to the coils is about 1 W. A pressure rise is observed after

injection. In Fig. 7 are reported the heat load (upper plot) and the pressure (lower plot) as a function of the beam current. The heat load is higher when the pressure is higher. A correlation between the heat load and the pressure is observed, (see inset of the upper plot). In the lower plot of Fig. 7 a non-linear increase in the pressure is observed by increasing the beam current. A maximum of the pressure is observed for an average current of about 160 mA. The peak shifts to lower currents of about 140 mA when the pressure is higher. A similar pressure rise with current has been observed in the positron ring at the Bfactory PEPII, a warm machine, for high currents and has been attributed to electron multipacting [16]. During the user operation mode of

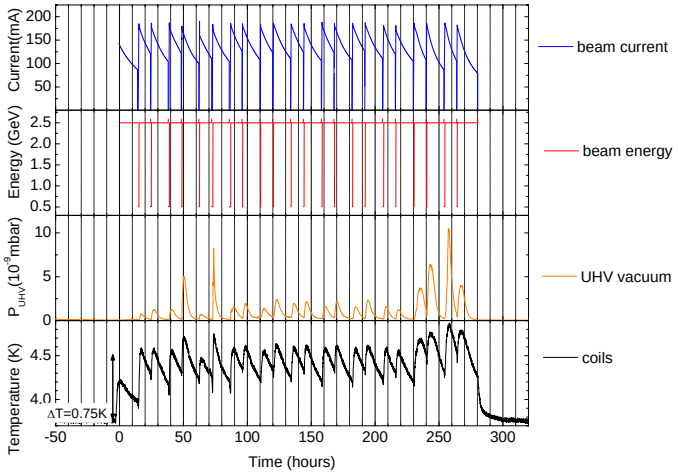

Figure 6: Typical user operation run with open gap (= 29 mm) and no current in the undulator. The beam current, the beam energy, the UHV pressure and the temperature of the coils are reported as a function of time.

ANKA a large variation of the heat load and of the UHV pressure is observed. In Fig. 8 is shown the heat load (upper plot) and the UHV pressure (lower plot) as a function of the average beam current I measured over half a year. In all cases the orbit is identical. The different colours refer to different runs over periods of about two weeks (similar to what is shown in Fig. 6 and in Fig. 7). The low current run measured during one of the machine shifts dedicated to the superconducting undulator studies indicates the correct calibration of the beam heat load: the heat load goes to zero for low beam currents. In the inset of the upper plot of Fig. 8 the beam heat load is shown as a function of the UHV pressure. A correlation between the two measured quantities is observed: above a certain heat load and pressure the heat load increases by increasing the pressure, below it is independent.

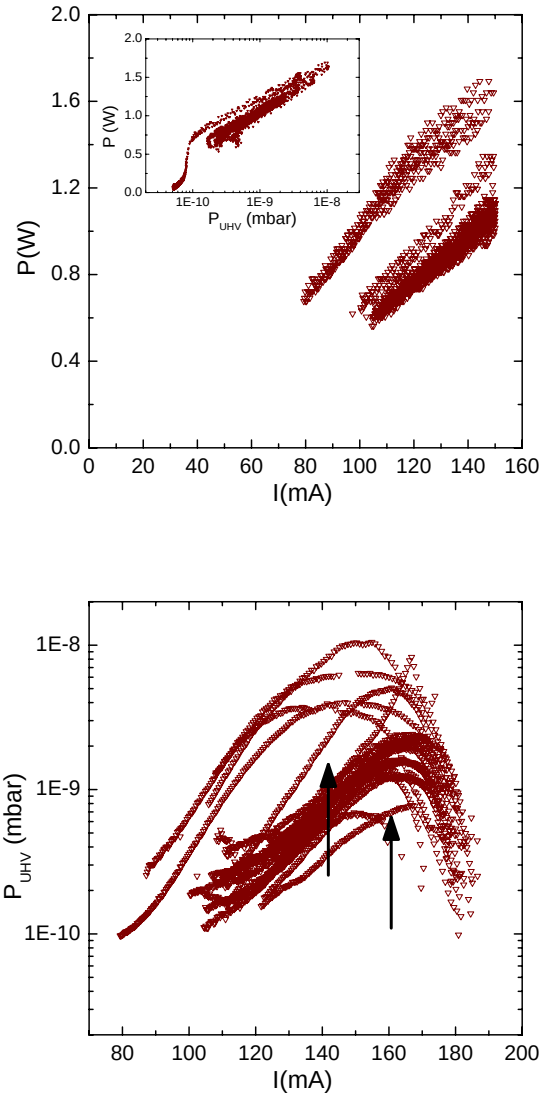

Figure 7: Upper plot: the beam heat load from Fig. 6 is shown as a function of the average beam current I and in the inset the beam heat load as a function of the UHV pressure. Lower plot: the UHV pressure from Fig. 6 is shown as a function of the average beam current I. The arrows indicate the current where the peak pressure is observed.

Dependence of the beam heat load on filling patterns

We have studied the dependence of the beam heat load as a function of current for different filling patterns. ANKA can be filled with one bunch train consisting of 32 bunches with a bunch spacing of 2 ns, or two or three bunch trains spaced by 120 ns. This allows to change the bunch current while the average current remains identical. Keeping in mind that for the following measurements less statistics is available, the beam heat load measured as a function of the

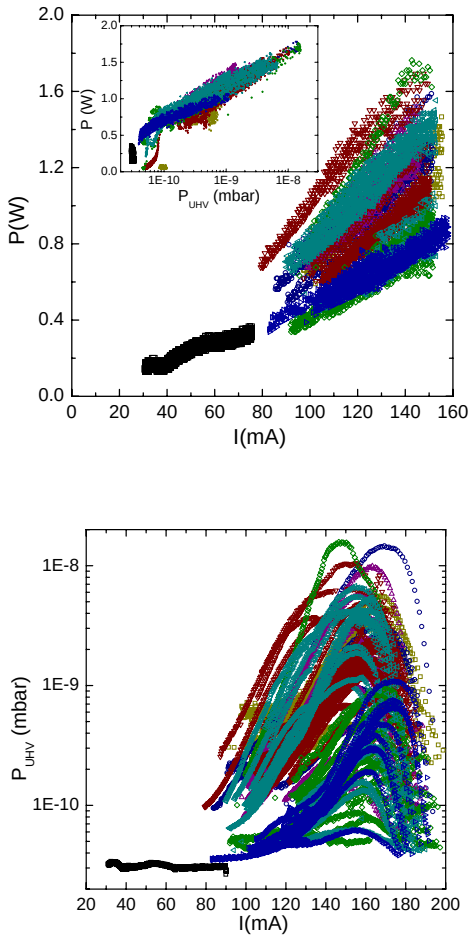

Figure 8: Variation over half a year of the beam heat load (upper plot) and of the UHV pressure (lower plot) reported as a function of the average beam current. The different colours refer to different runs over a period of about two weeks. In the inset of the left plot the beam heat load is shown as a function of the UHV pressure. Beam parameters: E=2.5 GeV, I=80-200 mA, two trains. Undulator parameters: gap= 29 mm, undulator current=0 A.

average beam current for 16 mm gap (see Fig. 9) scales as:

$$P \propto \frac{I^2}{M} \tag{8}$$

where I is the stored average beam current and M the total number of bunches per revolution. Such a scaling is typical for losses caused by resistive mechanisms.

In the inset of Fig. 9 the UHV pressure as a function of the average beam current is shown. The pressure rise is in some runs quite low and no peak is observed as a function of current. In case of electron bombardment a possible explanation would be the dependence of the peak current on the beam history: it is in fact known that the desorption coefficients and the secondary emission yields of the different gas molecules adsorbed on the vacuum chamber decrease with beam exposure time (electron dose) [13].

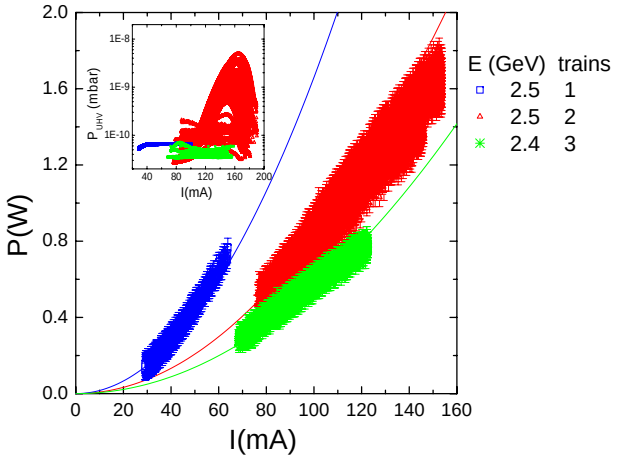

Figure 9: The beam heat load reported as a function of the average beam current for three different filling patterns. The three curves are polynomial fits demonstrating the scaling law $P \propto I^2/M$. Blue line: $P(\mathrm{W}) = 1.66 \times 10^{-4} I^2(\mathrm{mA})$. Red line: $P(\mathrm{W}) = 1.66/2 \times 10^{-4} I^2(\mathrm{mA})$. Green line: $P(\mathrm{W}) = 1.66/3 \times 10^{-4} I^2(\mathrm{mA})$. In the inset the UHV pressure is shown as a function of average beam current.

Beam heat load with sub-picosecond pulses

In order to produce short bunches of a few hundreds fs ANKA can be operated in the so-called low α mode [17]. The measured beam heat load for a run in the low α mode with one train at E=1.3GeV and a gap=29mm is shown in Fig. 10. The data can be well fitted by the resistive wall heating model using Eq. (2) taking into account the anomalous skin effect, assuming a RRR=100 and a bunch length of 500 fs. The value of 500 fs is consistent with the bunch lengths measured in the low α mode by means of THz edge synchrotron radiation [19]. During standard operation the bunch length varies with beam energy. The heat load induced by resistive wall effects should be higher at lower energies since the bunch length is shorter. This is not the case. So resistive wall heating seems to be dominant for short bunches but not for longer ones. We conclude that another heating mechanism must be responsible for the beam heat load observed during user operation.

Heat load by changing the gas content in the undulator

With the aim to see if the effect is caused by the gas composition, H_2 was injected in the warm side before and after the undulator. A scheme of the experimental setup is shown in Fig. 11. The idea is to increase the equilibrium pressure to enhance the H_2 surface coverage s and consequently the beam heat load. We were able to change the equilibrium pressure only by about a factor of 2.5 from $2 \cdot 10^{-11}$ mbar to $5 \cdot 10^{-11}$ mbar, so the surface coverage could not significantly be changed (see Fig. 4). The results

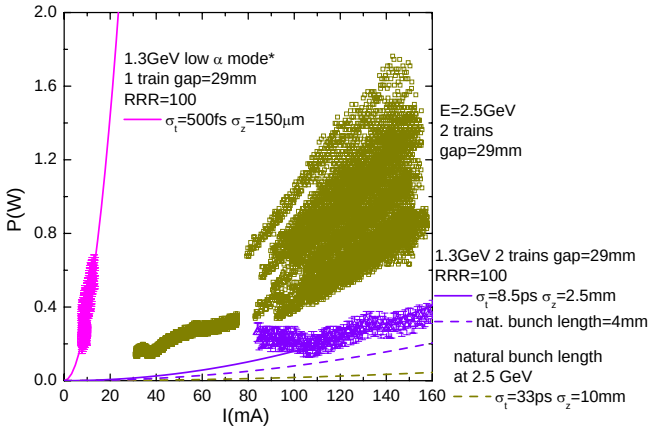

Figure 10: The beam heat load reported as a function of the average beam current for three different bunch lengths. The four curves are theoretical predictions based on Eq. (2) computed for different bunch legnths as indicated. The dashed curves are obtained with the natural bunch length (defined only for the normal optic of the ring, so for longer bunches), derived from Ref. [18]. The continuous curves are obtained by using bunch lengths values to fit the experimental data.

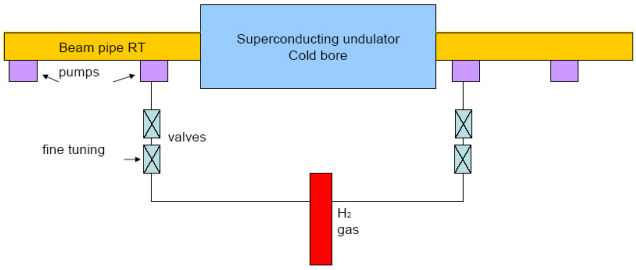

Figure 11: Scheme of the experimental setup for H_2 injection in the undulator.

are shown in Fig. 12: the beam heat load does not change. Two runs with respectively three and two trains have been performed. Figure 12 also shows two successive runs without further injecting H_2 and with pumps once on and once off. The pressure gets higher during all the runs and the current where the peak pressure is observed shifts to values lower than observed before H_2 injection (see the run with $E = 2.5$ GeV with two trains, open red triangles). As shown in the inset of the upper plot of Fig. 12, again a correlation is observed between the beam heat load and the pressure. We also observe (see lower plot of Fig. 12) that the current where the peak pressure is observed depends on the number of bunches: for two trains it is lower than for three trains.

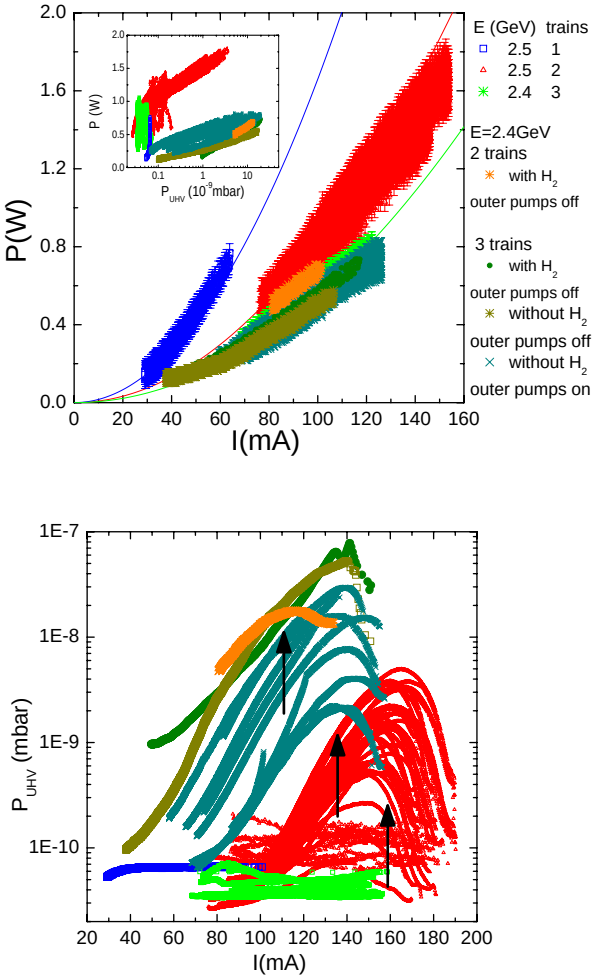

Figure 12: The beam heat load (upper plot) and the UHV pressure (lower plot) are shown as a function of the average beam current I. In the upper plot the three curves (continous lines) have been explained in Fig. 9. The arrows in the lower plot indicate the current at which the pressure has a peak. Starting from high currents they refer to: run with E=2.5 GeV, two trains and no H_2 injected (red open triangles), run with E=2.4 GeV, three trains, H_2 injected and after injection (olive green circles, dark yellow stars and dark cyan crosses), run with E=2.4 GeV, two trains and H_2 injected (orange stars). In the inset the beam heat load is reported as a function of the UHV pressure. The beam parameters and the undulator gap are indicated in the upper plot for the different runs. In all cases the current in the superconducting coils of the undulator is zero.

Pressure rise and heat load due to electron bombardement

The equations of gas dynamic balance inside a vacuum chamber can be written as (see Ref. [20, 21] and references

therein):

$$\begin{aligned} V\frac{dn}{dt} &= q + q'(s) - \alpha S(n - n_e(s,T)) + u\frac{d^2n}{dz^2}; \\ A\frac{ds}{dt} &= \alpha S(n - n_e(s,T)) - q'(s) \end{aligned} \quad (9)$$

where n is the volume gas density, s the surface density of the cryosorbed gas, V the vacuum chamber volume, A the vacuum chamber wall area, q is the primary beam induced desorption flux, q' the secondary beam induced desorption flux (desorption of cryosorbed molecules), α the sticking coefficient, $S = A\bar{\nu}/4$ is the ideal wall pumping speed, $\bar{\nu}$ is the mean molecular speed, n_e the thermal equilibrium gas density, and u the specific vacuum chamber conductance per unit axial length. The beam induced desorption flux consists of photon (PSD) and electron (ESD) stimulated desorption:

$$\begin{aligned} q &= \eta\dot{\Gamma} + \phi\dot{\Theta}; \\ q' &= \eta'\dot{\Gamma} + \phi'\dot{\Theta}; \end{aligned} \quad (10)$$

where η and η' are the primary and secondary electron stimulated desorption yields, $\dot{\Gamma}$ is the electron flux, ϕ and ϕ' are the primary and secondary photodesorption yields, and $\dot{\Theta}$ is the photon flux.

The volume gas density n at a temperature T is related to the pressure measured at room temperature by:

$$n = \frac{P}{k_B\sqrt{TT_{RT}}} \quad (11)$$

When the pressure reaches the maximum (see Fig. 6) as a function of time, $dn/dt = 0$. The u the specific vacuum chamber conductance per unit axial length is given by $u = A_cD$, where $D = 2/3A_c\bar{\nu}$ is the Knudsen diffusion coefficient being A_c the area of the rectangular cross section of the vacuum chamber. Axial diffusion can be neglected when $DA_c/L^2 < S\alpha$ [20], which means:

$$\frac{8}{3}\frac{A_c^2}{AL^2} < \alpha \quad (12)$$

Experimental values of the sticking coefficient for H_2 at 4.2 K indicate $\alpha > 0.02$ [22]. Even considering $\alpha = 0.02$ condition (12) is satisfied for the geometry of the undulator vacuum chamber where L=1.4 m and for a gap of 29 mm, $A_c = 0.00191$ m^2 and $A = 0.266$ m^2. Neglecting axial diffusion $ud^2n/dz^2 \approx 0$, the sum of the primary and recycling desorption yield of all gas species can be computed using the following equation:

$$\frac{q + q'}{\alpha} = S(n - n_e(s,T)) = SG\Delta P \quad (13)$$

where $\Delta P = P_{max} - P_e$ with $P_e \approx 2 \cdot 10^{-11}$ mbar the thermal equilibrium pressure and $G = \frac{1}{k_B\sqrt{TT_{RT}}} = 2 \cdot 10^{17}$ cm^{-3}/mbar. For the ANKA cold bore vacuum chamber with gap $=$ 29 mm and average beam current $I = 100$ mA, the photon flux impinging on the lower and upper surfaces is $\dot{\Theta} \approx 10^{16}$ photons/s.

If the heat load observed is generated by electron bombardment and assuming a mean electron energy $\Delta W =$ 10 eV, the estimated electron flux for a heat load of $P =$ 1 W is $\dot{\Gamma} \approx 6 \cdot 10^{17}$ electrons/s. Being $\phi + \phi' \lesssim \eta + \eta'$ [13, 23], we can neglect the PSD to the beam desorption flux, so that $q = \eta\dot{\Gamma}$ and $q' = \eta'\dot{\Gamma}$. The observed ΔP ranges from $2 \cdot 10^{-11}$ mbar to $8 \cdot 10^{-8}$ mbar. For H_2 the mean molecular speed at 4.2 K is $\bar{\nu} = 210$ m/s. The area of the vacuum chamber for a gap=29 mm is $A = 0.266$ m^2. Applying Eq.(13) we find that the sum of the primary and secondary desorption yields for H_2 $(\eta + \eta')/\alpha$ ranges between 10^{-4} molecules/electron to 4 molecules/electron. Our values are in good agreement with the ones measured at COLDEX [13] that range between 10^{-2} molecules/electron for an electron dose of $2 \cdot 10^{19}$ electrons/cm^2 to 30 molecules/electron for an electron dose of 10^{17} electrons/cm^2, considering that in our case the temperature is lower (4.2 K instead of 12 K), the mean electron energy is an order of magnitude smaller (10 eV instead of 100 eV) and that our electron dose is in some cases much higher (after two weeks of normal user operation it is about $2 \cdot 10^{20}$ electrons/cm^2).

CONCLUSIONS AND OPEN QUESTIONS

A non-linear pressure rise with current is observed. This rise might be due to H_2 recycling and/or electron multipacting. The current where the peak pressure is observed is lower when the pressure is higher and it decreases also for higher bunch currents. The peak is not always observed. One possible explanation would be the dependence of the peak current on the beam history: it is in fact known that the desorption coefficients and the secondary emission yields of the different gas molecules adsorbed on the vacuum chamber decrease by increasing the beam exposure time [13].

Concerning the beam heat load we have compared the data with theoretical predictions from different models. Synchrotron radiation cannot explain the data since it predicts a linear dependence with current which is not observed. The resistive wall heating model can fit the data for short bunches but it does not for longer bunches. We do observe that the heat load scales with I^2/M, which is typical for resistive effects. On the other hand a smaller beam heat is observed at lower beam energies when the bunch length is shorter. Resistive effects would imply to observe a higher beam heat load for shorter bunches. Resistive effects also can not explain the large variation in the beam heat load.

The electron bombardment model is consistent with the beam heat load and pressure rise observed during normal user operation (longer bunches). Still to be understood is the mechanism responsible for releasing the electrons from the gas layer cryosorbed on the wall of the vacuum chamber.

ACKNOWLEDGEMENTS

The authors are indebted to V. Baglin and O. B. Malyshev for valuable discussions. The measurements at ANKA were performed together with the ANKA machine group: I. Birkel, E. Huttel, A.-S. Müller, and P. Wesolowski. The authors would like to thank E. Huttel for useful discussions and A. Völker for technical support in setting up the H_2 experiment.

REFERENCES

[1] J. Chavanne, P. Elleaume, Proceedings of EPAC 2006, Edinburgh, Scotland 2006.

[2] S. Casalbuoni et al., *Phys. Rev. ST Accel. Beams* **9**, 010702 (2006).

[3] E. Levitchev et al., Proceedings of EPAC 2006, Edinburgh, Scotland 2006.

[4] J.A. Clarke et al., Proceedings of EPAC 2006, Edinburgh, Scotland 2006.

[5] http://ankaweb.fzk.de/

[6] S. Chouhan et al., Proceedings of PAC 2003, Portland, Oregon, USA 2003.

[7] SHI Cryogenics Group, http://www.apdcryogenics.com

[8] S. Casalbuoni et al., Proceedings of EPAC 2006, Edinburgh, Scotland 2006.

[9] E. Wallén, G. LeBlanc, *Cryogenics* **44**, 879 (2004).

[10] W. Chou and F. Ruggiero, LHC Project Note 2 (SL/AP), (1995).

[11] H. London, *Proc. Royal Society (London)* **A176**, 522 (1940); A.B. Pippard, *Proc. Royal Society (London)* **A191**, 385 (1947); G.E.H. Reuter and E.H. Sondheimer, *Proc. Royal Society (London)* **A195**, 336 (1948); R.G. Chambers, *Proc. Royal Society (London)* **A215**, 481 (1952).

[12] O. Gröbner, Proceedings of PAC 1997, Vancouver, Canada 1997.

[13] V. Baglin, B. Jenninger, LHC Project Report 721, 2004.

[14] http://cas.web.cern.ch/cas/Spain-2006/PDFs/Hilleret-1.pdf

[15] E. Wallén, *JVSTA* **14** (5), 2916 (1996).

[16] A. Kulikov et al., Proceedings of PAC 2001, Chicago, Illinois, USA 2001.

[17] A.-S. Müller et al., Proceedings of PAC 2005, Knoxville, Tennessee, USA 2005.

[18] F. Perez et al., Proceedings of PAC 2003, Portland, Oregon, USA 2003.

[19] A. Bernhard et al., Proceedings of Applied Superconductivity Conference, ASC 2006, Seattle, WA, USA, to appear in IEEE Transactions on Applied Superconductivity

[20] W.C. Turner, Proceedings of PAC 1993, Washington, D.C., USA 1993.

[21] I.R. Collins and O.B. Malyshev, LHC Project Report 274, 2001.

[22] S. Andersson et al., *Phys. Rev. B* **40**, 8146 (1989).

[23] V.V. Anashin et al., Vacuum **48** (7-9), 785 (1996).

Wakepotential of an Array of thin Electrodes in a Beampipe.

Warner Bruns, CERN, Geneva, Switzerland

Abstract

Clearing electrodes might decrease the buildup of electron clouds. The wakepotential of such electrodes is computed under simplifying conditions: The thickness of the electrodes is neglected, the electrodes are very near to the beampipe walls, the beampipe and the electrodes are assumed to be rectangular. Under such conditions, the wakepotential of electrodes *without* a substrate is essentially negligible. The wakepotential with substrate is significant and can be explained by the lower group velocity in the substrate.

The device under scrutiny is an array of electrodes in a beam pipe. The beampipe is assumed to be rectangular. At the bottom and top of the pipe the electrodes are attached. The electrodes are modeled as infinitely thin sheets of perfectly conducting material. If the electrodes would be located at places of constant beam-potential, and if the substrate would consist of invisible material, ie. $\varepsilon_r = 1$, they would not have any wakepotential at all, as they then would not disturb the primary field of the relativistic beam. The part of the primary field which enters the space between the electrodes and the wall travels with the velocity of light towards the end of the electrode, where it recombines with the primary field of the beam above the electrode. No field scattering occurs. No wakepotential is experienced. Because the electrodes are very near to the beam pipe walls, they almost fulfil the condition of being on places of constant beam-potential.

Between the pipes wall and the electrodes is a dielectric material. The wakepotential are computed when the electrodes are lying on a dielectric with $\varepsilon_r = 2$, and for comparison when the dielectric material is invisible, ie. $\varepsilon_r = 1$. The wakepotential of the conducting foil with dielectric is much larger. This is because the energy in the dielectric travels with a velocity much less than the velocity of light. The field which travels through the dielectric reaches the end of the foil much later than the beam reaches the end of the foil. The beam field above the foil therefore cannot recombine with the field below the foil, as it is the case if the dielectric below the foil is not present.

WAKEPOTENTIALS OF AN LHC-BEAM

The results are computed with beamparameters of the LHC. The length of the beam is sigma=8cm. The width and height of the rectangular beam pipe is 4cm.

Figure 2 shows the wakepotential of two electrodes with a length of 40cm. The wakepotential is essentially a periodic function with a period length of 10/9 metres. This period length is twice the length of the electrodes times the refractive index of the material with $\varepsilon_r = 2$.

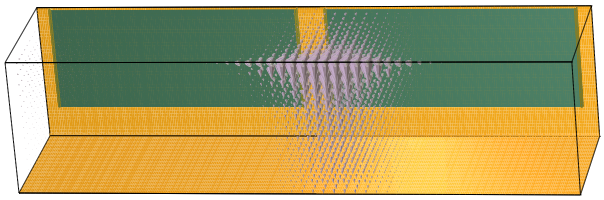

Figure 1: The grid used to compute the wakepotential of an array of two electrodes. The substrat thickness is 1mm. The width of the electrodes is 30mm. The gap between the electrodes is 4mm. The x-extension of the beampipe is 40 mm, the y-extension is 20 mm. A quarter of the structure is used for the computation. The shown electrodes are much shorter than the ones used for the real computations. The shown electrodes have a length of only 4 cm. The field shown in this plot is from a bunch with a length of sigma=0.5cm. This is much shorter than the bunch used for the real computations.

Figure 3 shows the wakepotentials of 2,4,8 and 16 electrodes. The shape of the wakepotentials do not differ. The amplitude grows linearly with the number of electrodes.

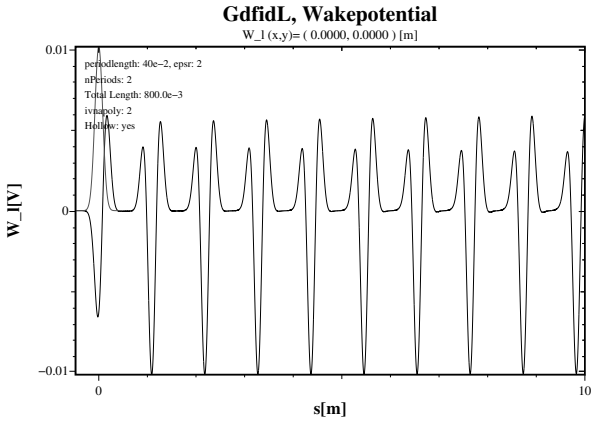

Figure 2: The computed longitudinal wakepotential for a gaussian line charge with sigma=8cm. Total charge 1pC. The number of electrodes is 2. The length of a single electrode is 40 cm. The permittivity of the substrate is epsr=2.

Figure 4 shows the wakepotential of two electrodes without a supporting dielectric. The wakepotential is again almost periodic, but it is much smaller than the wakepoten-

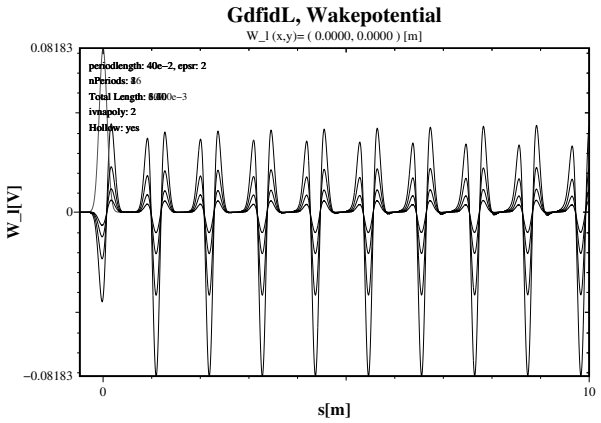

Figure 3: The computed longitudinal wakepotential for a gaussian line charge with sigma=8cm. Total charge 1pC. The number of electrodes is 2,4,8,16. The length of a single electrode is 40 cm. The permittivity of the substrate is epsr=2.

tial as shown in figure 2. The period length is 10/12.5 metres. This period length is twice the length of the electrodes times the refractive index of the material with $\varepsilon_r = 1$.

Figure 5 shows the wakepotential of 2,4,8,16 electrodes without a supporting dielectric. The shape of the wakepotentials do not differ. The amplitude grows linearly with the number of electrodes.

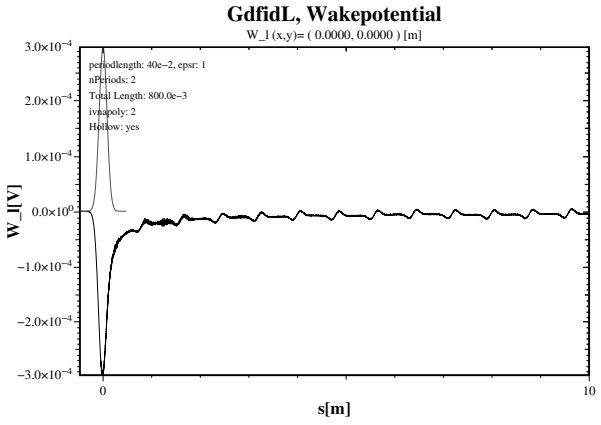

Figure 4: The computed longitudinal wakepotential for a gaussian line charge with sigma=8cm. Total charge 1pC. The number of electrodes is 2. The length of a single electrode is 40 cm. The permittivity of the substrate is epsr=1.

Figures 6, 7, 8, 9 show the real and imaginary part of the impedance corresponding to the wakepotentials as shown in figure 4, 5. The shown results are computed by an FFT of the finite s-range of figures 4, 5 and therefore do show finite resonances, ie not dirac pulses.

Figure 10 shows the wakepotential of two electrodes with a length of 20cm. The wakepotential is essentially a periodic function with a period length of 10/18 metres. This period length is twice the length of the electrodes

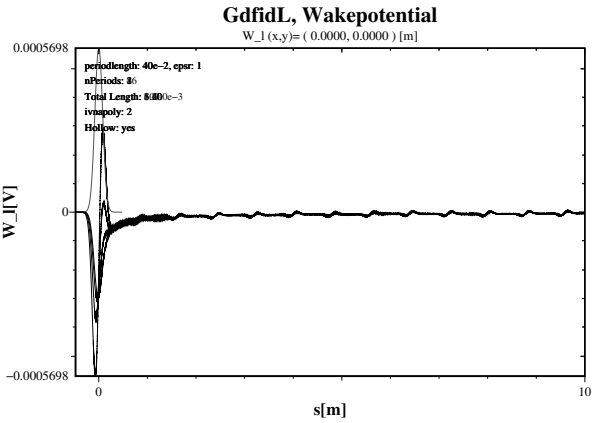

Figure 5: The computed longitudinal wakepotential for a gaussian line charge with sigma=8cm. Total charge 1pC. The number of electrodes is 2,4,8,16. The length of a single electrode is 40 cm. The permittivity of the substrate is epsr=1.

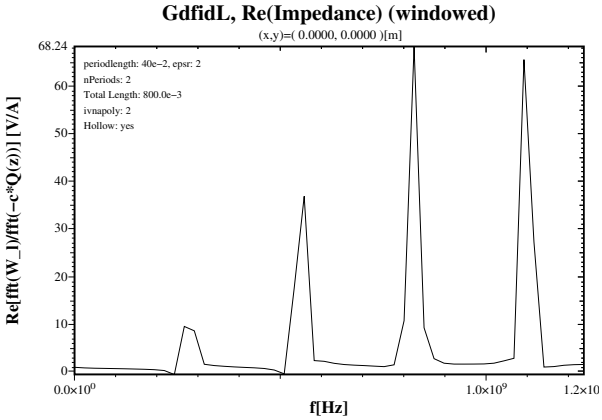

Figure 6: Real part of the computed longitudinal impedance. The number of electrodes is 2. The length of a single electrode is 40 cm. The permittivity of the substrate is epsr=2.

times the refractive index of the material with $\varepsilon_r = 2$.

Figure 11 shows the wakepotentials of 2,4,8 and 16 electrodes. The shape of the wakepotentials do not differ. The amplitude grows linearly with the number of electrodes.

Figures 12, 13 show the real part of the impedance corresponding to the wakepotentials as shown in figure 10, 11. The shown results are computed by an FFT of the finite s-range of figures 10, 11 and therefore do show finite resonances, ie not dirac pulses.

Figure 14 shows the wakepotential of two electrodes with a length of 10cm. The wakepotential is essentially a periodic function with a period length of 10/37 metres. This period length is twice the length of the electrodes times the refractive index of the material with $\varepsilon_r = 2$.

Figure 15 shows the wakepotentials of 2,4,8 and 16 electrodes. The shape of the wakepotentials do not differ. The amplitude grows linearly with the number of electrodes.

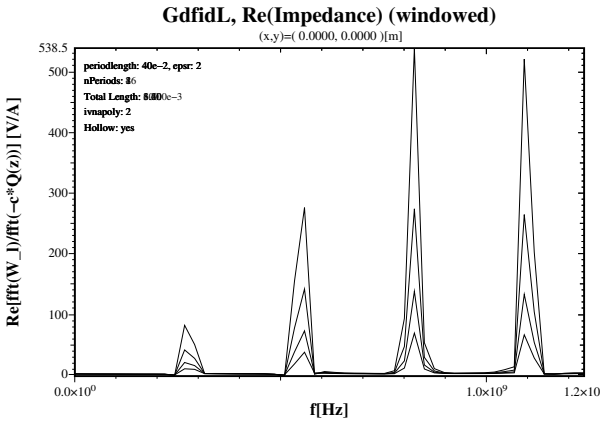

Figure 7: Real part of the computed longitudinal impedance. The number of electrodes is 2,4,8,16. The length of a single electrode is 40 cm. The permittivity of the substrate is epsr=2.

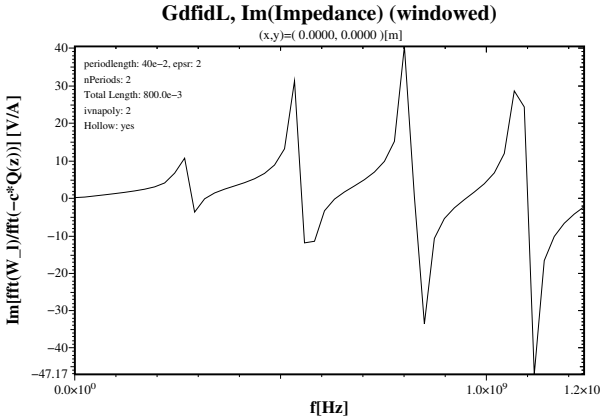

Figure 8: Imaginary part of the computed longitudinal impedance. The number of electrodes is 2. The length of a single electrode is 40 cm. The permittivity of the substrate is epsr=2.

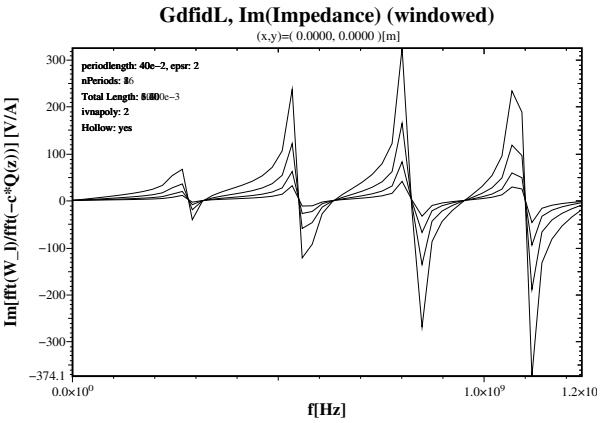

Figure 9: Imaginary part of the computed longitudinal impedance. The number of electrodes is 2,4,8,16. The length of a single electrode is 40 cm. The permittivity of the substrate is epsr=2.

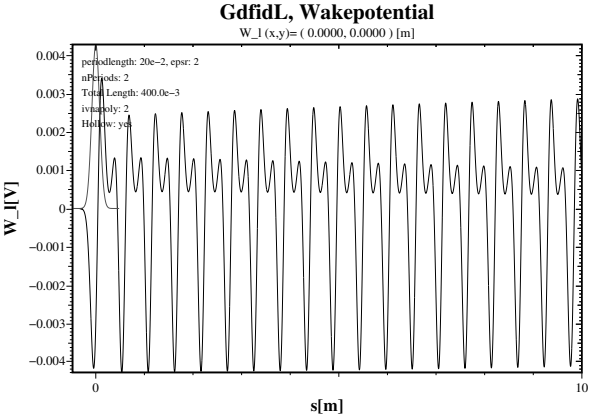

Figure 10: The computed longitudinal wakepotential for a gaussian line charge with sigma=8cm. Total charge 1pC. The number of electrodes is 2. The length of a single electrode is 20 cm. The permittivity of the substrate is epsr=2.

Figures 16, 17 show the real part of the impedance corresponding to the wakepotentials as shown in figure 10, 11. The shown results are computed by an FFT of the finite s-range of figures 14, 15 and therefore do show finite resonances, ie not dirac pulses.

DISCUSSION AND CONCLUSION

Figures 3, 11, 15 show that the amplitude of the wakepotentials grow linearly with the number of electrodes.

The amplitude of the wakepotential of two electrodes with a length of 40cm, 2, is 0.01 V/pC. The wakepotential of two electrodes of half length, 20cm, 10, is 0.004 V/pC. The wakepotential of two electrodes of quarter length, 10cm, 14, is 0.001 V/pC. This suggests that the wakepotential grows with the length of the electrodes. This is not expected from the model that the wakepotential comes from the fact that the energy flowing below the electrodes cannot recombine with the energy flowing above. From that model one would expect that the wakepotential only depends on the number of the electrodes, not on their length. It might be, that the wakepotential has this dependence on the length of the electrodes, because the length of the exciting bunch is comparable with the length of the electrodes. To investigate this, the wakepotential of a shorter bunch is computed. Figures 18, 19, 20 show the wakepotentials of a gaussian line charge with sigma=1cm. The length of the electrodes is 10cm, 20cm, 40 cm. The number of electrodes is 2. The amplitude of these three wakepotentials is about the same.

For electrodes having a low wakepotential per length, the dielectric would have to be invisible, which is not possible, or the electrodes should have maximal length. The wakepotential is proportional to the number of electrodes, not the total length of the electrodes.

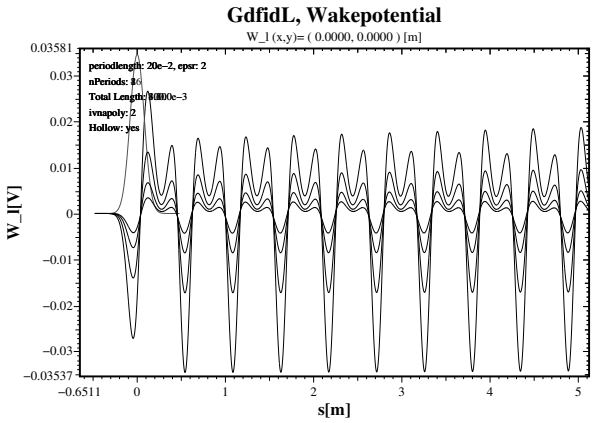

Figure 11: The computed longitudinal wakepotential for a gaussian line charge with sigma=8cm. Total charge 1pC. The number of electrodes is 2,4,8,16. The length of a single electrode is 20 cm. The permittivity of the substrate is epsr=2.

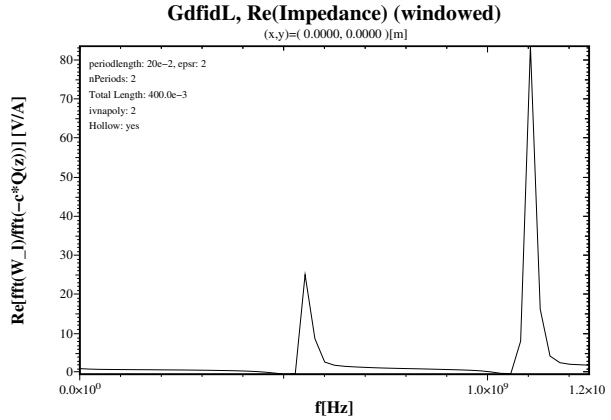

Figure 12: Real part of the computed longitudinal impedance. The number of electrodes is 2. The length of a single electrode is 20 cm. The permittivity of the substrate is epsr=2.

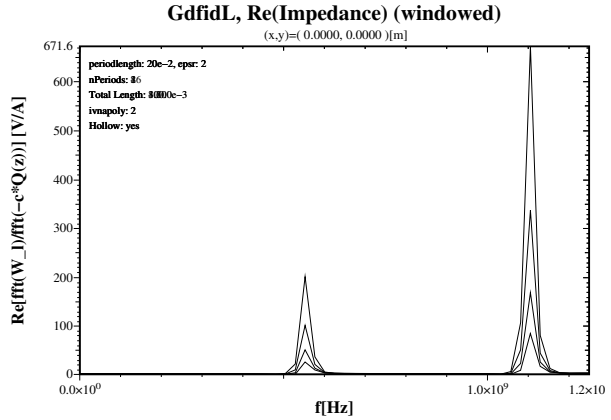

Figure 13: Real part of the computed longitudinal impedance. The number of electrodes is 2,4,8,16. The length of a single electrode is 20 cm. The permittivity of the substrate is epsr=2.

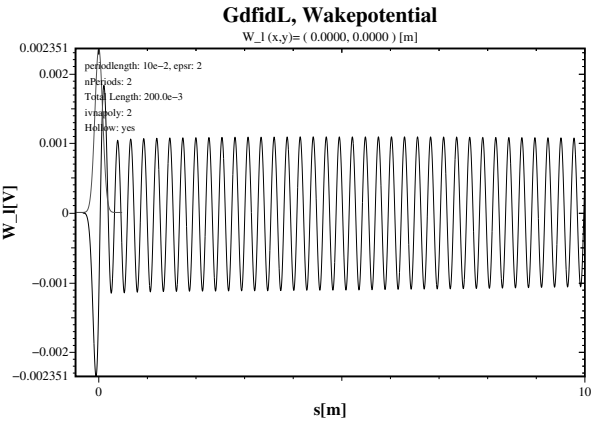

Figure 14: The computed longitudinal wakepotential for a gaussian line charge with sigma=8cm. Total charge 1pC. The number of electrodes is 2. The length of a single electrode is 10 cm. The permittivity of the substrate is epsr=2.

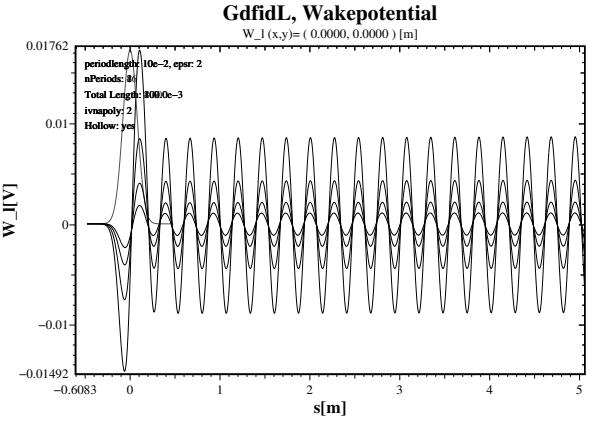

Figure 15: The computed longitudinal wakepotential for a gaussian line charge with sigma=8cm. Total charge 1pC. The number of electrodes is 2,4,8,16. The length of a single electrode is 10 cm. The permittivity of the substrate is epsr=2.

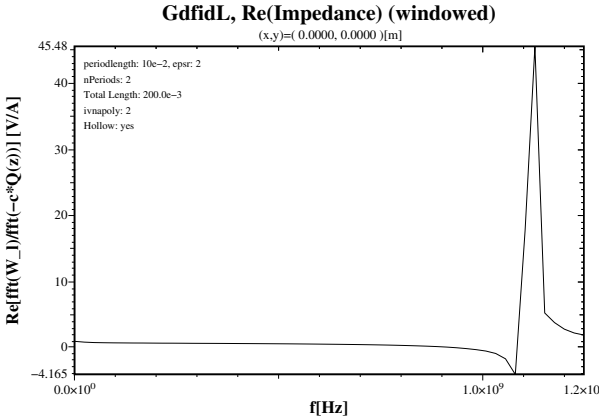

Figure 16: Real part of the computed longitudinal impedance. The number of electrodes is 2. The length of a single electrode is 10 cm. The permittivity of the substrate is epsr=2.

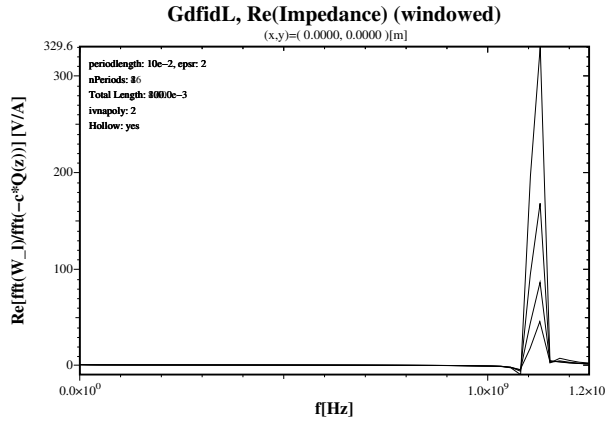

Figure 17: Real part of the computed longitudinal impedance. The number of electrodes is 2,4,8,16. The length of a single electrode is 10 cm. The permittivity of the substrate is epsr=2.

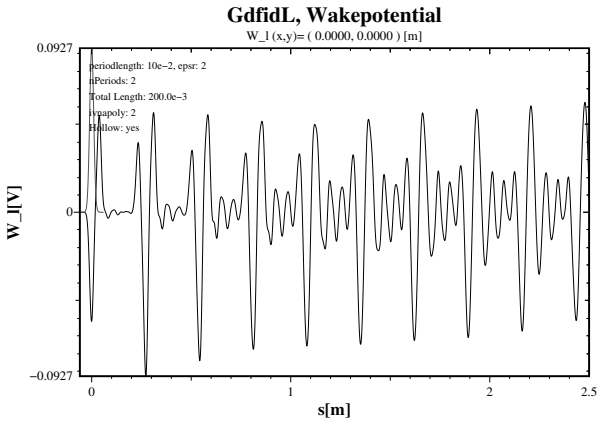

Figure 18: The computed longitudinal wakepotential for a gaussian line charge with sigma=1cm. Total charge 1pC. The number of electrodes is 2. The length of a single electrode is 10 cm. The permittivity of the substrate is epsr=2.

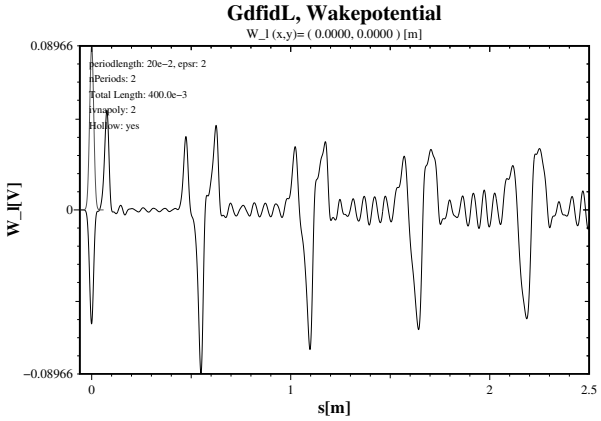

Figure 19: The computed longitudinal wakepotential for a gaussian line charge with sigma=1cm. Total charge 1pC. The number of electrodes is 2. The length of a single electrode is 10 cm. The permittivity of the substrate is epsr=2.

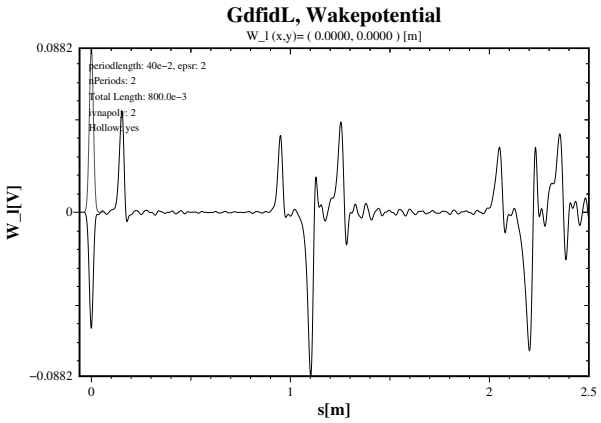

Figure 20: The computed longitudinal wakepotential for a gaussian line charge with sigma=1cm. Total charge 1pC. The number of electrodes is 2. The length of a single electrode is 40 cm. The permittivity of the substrate is epsr=2.

DISTRIBUTED ELECTRON CLOUD CLEARING ELECTRODES

T. Kroyer, F. Caspers, E. Métral, F. Zimmermann, CERN, Geneva, Switzerland

Abstract

Clearing electrodes can be an efficient means for suppressing the electron cloud build-up in high intensity particle accelerators. So far mainly button type and other small electrodes have been used in various machines at distinct locations. This paper discusses distributed clearing electrodes, which can be installed over longer sections of a machine. The longitudinal and transverse impedance is evaluated analytically and by numerical simulations. Furthermore, the clearing efficiency of various electrode geometries was simulated and the properties of enamel as a possible insulator are discussed.

INTRODUCTION

In many high-intensity particle accelerators the electron cloud (EC) effect turned out to be a serious issue. A potential remedy is clearing electrodes, which have been installed in several machines for suppressing the EC build-up or for ion clearing [1, 2, 3]. So far, however, the experience with clearing electrodes is mostly limited to button-type electrodes. Longer electrodes have also been used [1, 4, 5]. In order to suppress the EC effect over longer sections of a machine, distributed clearing electrodes are needed. However, as the design length of such electrodes increases, many requirements become more stringent. Retrofittable clearing electrodes for the LHC cold arcs were proposed in [6].

This paper first lists desirable features of distributed clearing electrodes. Then possible electrode geometries are discussed and beam coupling impedance aspects, clearing efficiency and technological issues examined.

Desirable features

Clearing electrodes should fulfil as many as possible of the following points:

- Good mechanical stability. This is important in particular in superconducting machines, where significant forces may appear in conductors during magnet quench.
- Good vacuum properties. The clearing electrodes must be compatible with the ultra-high vacuum (UHV, 10^{-8} mbar and below) in the beam pipe. Very low outgassing (of the order of 10^{-12} mbar·l/(s·cm^2)) is required. The electrode assembly should be easy to clean for installation in the UHV environment.
- Limited aperture reduction. The aperture reduction should be very small, possibly only fractions of a mm.
- Low longitudinal and transverse impedance. Clearing electrodes should not substantially increase the machine impedance.
- Good thermal coupling to a heat sink. Especially when high heat loads on the electrode are expected, a good thermal contact to the heat sink, e.g. the beam pipe is needed. The main heat load is usually due to resistive losses in the electrodes; in case a significant EC develops it will also contribute to the heat load. In particular for stretched wires the thermal coupling to the beam pipe may be insufficient, since heat conduction is not possible and heat radiation is generally not efficient due to the low emissivity of the involved metal surfaces.
- Low secondary emission yield (SEY). The efficiency of clearing electrodes is reduced when their SEY is higher than that of the beam pipe.
- The electrodes should survive the usual baking at about 250 to 300° C. In superconducting machines they should also stand cryogenic temperatures.
- They should stand a DC voltage of the order of 1 kV.
- For electrodes with a highly resistive coating the voltage drop along the electrode due to the clearing current and leakage should be small compared to the bias voltage.
- Radiation hardness and activation. The electrodes should withstand the beam losses impacting onto the beam pipe. The usage of materials susceptible to activation should be very limited.
- Magnetic properties. In order not to interfere with beam diagnostics and the beam itself ferromagnetic materials must be avoided.

ELECTRODE CONFIGURATION

The number and shape of the electrodes are fundamental design parameters. In order to find an appropriate electrode geometry for studying aspects of implementation and impedance, the available literature was researched and electrostatic field simulations were carried out using the CST EM Studio package [7].

Number of electrodes

Simulation results of the clearing efficiency of two wire electrodes in KEKB are reported in [8]. The electrostatic simulation results of a similar geometry are depicted in

Fig. 1.
When the electrodes have opposite polarities at ± 1 kV, the EC build-up is considerably enhanced. This effect is probably due to the electrons gaining energy when they are accelerated close to the positive electrode, where the electric field is high. On the other hand, for one single electrode at a potential of -1 kV with respect to the beam pipe a very good clearing efficiency was found. When both electrodes are at -1 kV, the clearing efficiency is still slightly better. Similar results are published in [2].
If these results are applicable to other machines, then the EC build-up can be efficiently suppressed by repelling the electrons using negatively polarized electrodes. Even a single electrode appears to be sufficient, which eases problems related to manufacturing, aperture and impedance. In order to be effective in dipole magnets, this electrode must be installed at the top or bottom of the chamber, since a horizontal electric field would only cause a slow $E \times B$ drift [10]. Recent simulations showed that a single electrode at -1 kV should work well in the CERN PS [11].

Electrode shape

In the following we consider a single electrode at a negative potential with respect to the beam pipe. The clearing efficiency depends on the potential in the center of the beam pipe U_C. When an electrode much wider than the beam pipe height is used U_C will be at the most half of the electrode voltage. For wire electrodes close to the wall U_C will be much smaller, since the resulting field looks like a dipole field.
For an U_C as large as the beam potential (typically several kV) the EC will be almost totally suppressed. For rather small clearing voltages (a few 100 V) considerable effects can be obtained as well, however the clearing efficiency is generally not a monotonic function of the clearing voltage [8, 2].
Two elementary electrode shapes were studied for a single electrode on the top of the vacuum chamber:

- A 2 mm radius round electrode 5 mm from the wall
- A 20 mm wide and 1 mm thick electrode 1 mm from the wall.

The resulting electric field pattern and potential for an electrode voltage of -1 kV are shown in Figs. 2 and 3. For flat electrodes a substantial potential U_C is retained even when the electrode is very close to the chamber wall. Therefore it is possible to minimize the aperture reduction. The design considered below is based on such flat electrodes.

Reference configuration

Two concepts exist for realizing clearing electrodes. Firstly, they can be built as a metallic conductor on a dielectric support. In practice, solid conductors or thin metal layers deposited e.g. by sputtering are used. Longitudinal resonances are possible on such structures unless both ends

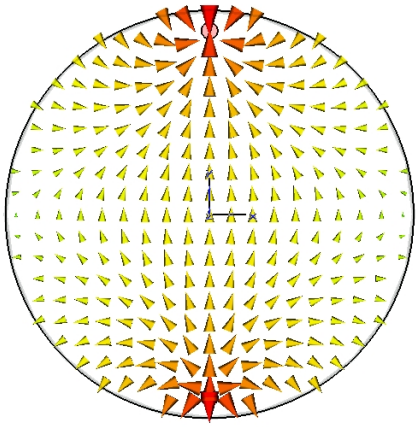

(a) Electrodes at opposite polarity enhance the EC build-up.

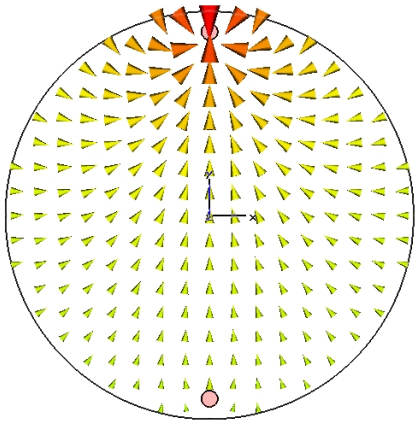

(b) One electrode at negative polarity gives a good clearing efficiency.

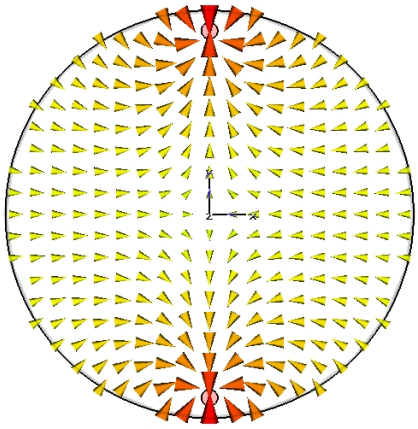

(c) Both electrodes at negative polarity yield a slightly better clearing effect than one single electrode.

Figure 1: Electrostatic simulation of two wires in a round chamber, corresponding to the clearing efficiency simulations presented in [8].

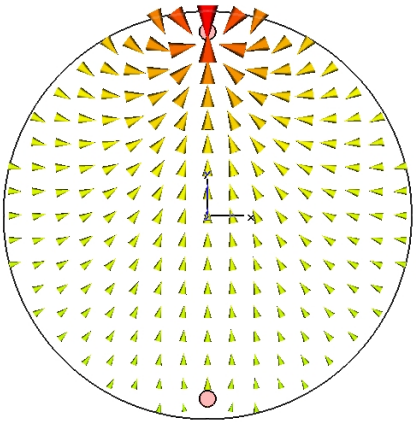

(a) A single wire with 2 mm diameter 5 mm from the wall, field in the center: 2.5 kV/m.

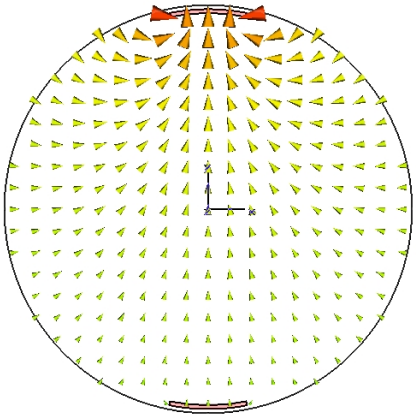

(b) A 20 mm wide electrode 1 mm from the wall, field in the center: 3.8 kV/m.

Figure 2: Comparison of the electric field (in logarithmic scale) from a wire and a flat electrode in a 50 mm diameter chamber with -1 kV clearing voltage. Going towards the center the field of the flat electrode decreases much slower than the one of the wire.

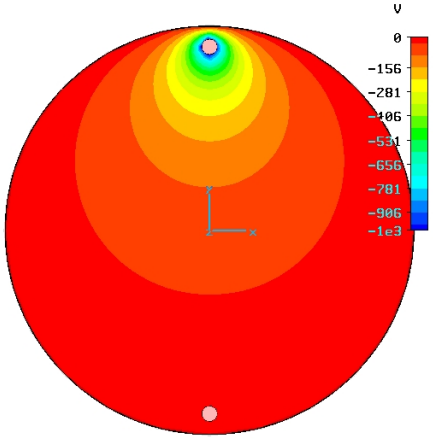

(a) A single wire with 2 mm diameter 5 mm from the wall, potential in the center: -60 V.

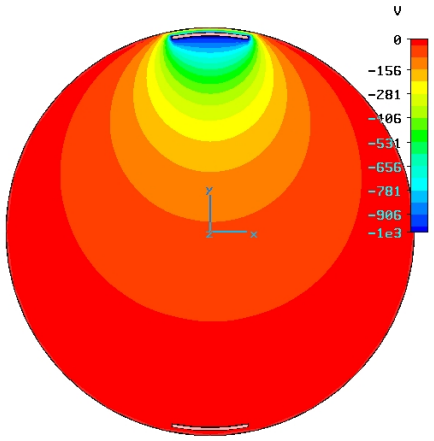

(b) A 20 mm wide electrode 1 mm from the wall, potential in the center: -85 V.

Figure 3: Comparison of the electric potential from a wire and a flat electrode in a 50 mm diameter chamber with -1 kV clearing voltage. The flat electrode allows a higher potential to be obtained while keeping the aperture reduction small.

of the electrode are terminated with their characteristic impedance. In the latter case we have a well-known stripline pick-up, which may have a substantial impedance and heat dissipation.

Alternatively, a highly resistive layer on an isolating strip can be used. If the layer's surface resistance is much higher than the free space impedance ($R_\square \gg Z_0 = 377\ \Omega$) such an electrode is "invisible" to the electromagnetic wave in the sense that it does not act like a metallic electrode [9]. The electrode together with the underlying insulator rather behaves like a bulk dielectric in the frequency range of interest, which typically extends up to a few GHz. This option was considered in more detail, since it appears most promising for long structures. In analytic calculations and numerical simulations this electrode was approximated as a dielectric strip.

The reference structure that was researched in more detail looks like the one depicted in Fig. 2(b). Inside a circular 50 mm radius chamber a single 25 mm wide dielectric strip is deposited. This layer can be made e.g. of enamel or a ceramic such as alumina with a thickness of the order of 0.1 mm. On top of this strip a $\approx$ 20 mm wide highly resistive thick film coating with a few 10 μm thickness is applied. At one or both ends of the chamber a feedthrough is installed to put the clearing voltage on the highly resistive layer. Each section of the electrode could have up to a few meters length and be installed both in straight sections as well as in magnets. The advantages of this kind of structure are as follows:

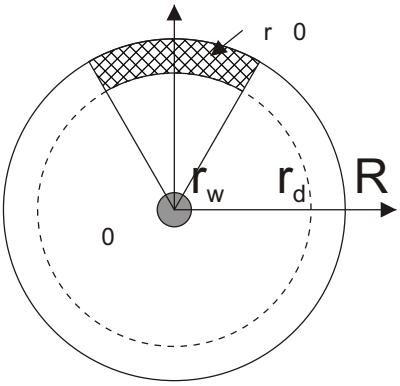

Figure 4: The single-electrode geometry used for the impedance calculations. The highly resistive electrode can be modelled as a dielectric layer in the relevant frequency range.

- Good mechanical stability, provided that the adherence of the dielectric to the chamber can be assured in the production process.
- Small aperture reduction of fractions of a mm.
- Good thermal contact to the beam pipe.

IMPEDANCE

The impedance of the highly resistive clearing electrodes described in the previous section was examined using an analytical approach as well as by numerical simulations. It was assumed that the dielectric strip together with the thick-film coating acts like a low-loss dielectric in the frequency range of interest. The considered geometry is a $R = 50$ mm diameter circular pipe with a $w = 25$ mm wide and $t = R - r_d = 0.1$ mm thick dielectric strip (Fig. 4). The permittivity was assumed to be $\epsilon_r \approx 5$, as measured on a sample of enamel coating.

Longitudinal impedance

The analytic evaluation of the longitudinal impedance is based on the analogy of the field pattern of highly relativistic beams and TEM transmission lines. The beam is represented by a lossless wire having a radius r_w equal to the rms beam size. Basic transmission line theory was used to calculate the capacity per unit length of a line with a dielectric layer all over the inner surface (dashed line in Fig. 4):

$$C' = \frac{2\pi\epsilon_0}{\ln\frac{r_d}{r_w} + \frac{1}{\epsilon_r}\ln\frac{R}{r_d}}. \tag{1}$$

As for an empty line the inductance per unit length is

$$L' = \frac{\mu_0}{2\pi}\ln\frac{R}{r_w}. \tag{2}$$

The group velocity v is given by

$$v = \frac{1}{\sqrt{L'C'}}. \tag{3}$$

Due to the presence of the dielectric v is smaller than the free space speed of light c.
The longitudinal impedance Z can be calculated from the log formula [12] by

$$Z = -2Z_L \ln S_{21}, \tag{4}$$

where Z_L designates the line impedance and S_{21} the transmission normalized to a reference line. Z_L is given by

$$Z_L = \sqrt{\frac{L'}{C'}} = \frac{1}{2\pi}\sqrt{\frac{\mu_0}{\epsilon_0}}\sqrt{\ln\frac{R}{r_w}\left(\ln\frac{r_d}{r_w} + \frac{1}{\epsilon}\ln\frac{R}{r_d}\right)}. \tag{5}$$

For very thin dielectric layers we recover the expression for the empty coaxial line

$$Z_L = \frac{1}{2\pi}\sqrt{\frac{\mu_0}{\epsilon_0}}\ln\frac{R}{r_w}. \tag{6}$$

Evaluating the imaginary part of the logarithm in Eq. 4 yields

$$\Im\{Z\} = -2Z_L \arg S_{21}. \tag{7}$$

For the given structure the phase of S_{21} is given by

$$\arg S_{21} = 2\pi f \Delta\tau, \tag{8}$$

where $\Delta\tau$ is the delay of the structure compared to the reference line. For $\Delta v = c - v \ll c$

$$\Delta\tau \approx -L\frac{\Delta v}{c^2} \tag{9}$$

for a length L. Hence, the longitudinal impedance becomes

$$\Im\{Z\} = 4\pi Z_L f L \frac{\Delta v}{c^2} \tag{10}$$

and after normalization for L equal to the machine circumference

$$\Im\{Z/n\} = 4\pi Z_L\left(1 - \sqrt{\frac{\ln\frac{r_d}{r_w} + \frac{1}{\epsilon_r}\ln\frac{R}{r_d}}{\ln\frac{R}{r_w}}}\right), \tag{11}$$

which for $t/R \ll 1$ can be simplified to first order to

$$\Im\{Z/n\} \approx \sqrt{\frac{\mu_0}{\epsilon_0}}\left(1 - \frac{1}{\epsilon_r}\right)\frac{t}{R}. \tag{12}$$

The above derivation is valid

- for dielectric layers very thin compared to the chamber radius.
- for frequencies where the highly resistive layer does not carry a significant image current, i.e. when the layer's surface resistance is much higher than the free space impedance ("invisibility" condition) and where the skin depth in the highly resistive layer is much larger than its thickness.
- when the dielectric loss tangent $\tan\delta \ll 1$.

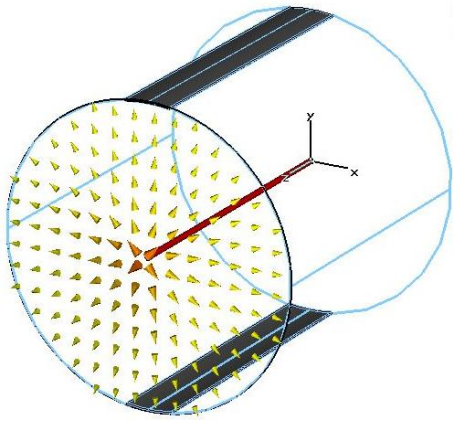

Figure 5: Wire simulation of two 0.5 mm thick dielectric strips inside a 50 mm radius pipe.

All these conditions should be fulfilled up to the 10 GHz range for typical ceramic or enamel-based layers covered with a thick-film coating. From Eq. 12 we can conclude that

- Since to first order a thin layer of lossless dielectric can only delay the wakefield, only the $\Im\{Z/n\}$ is affected by the presence of the electrodes.
- In the relevant frequency range $\Im\{Z/n\}$ is constant.
- Numerical evaluation shows that for thin layers
  - $\Im\{Z/n\}$ is proportional to the layer thickness t.
  - $\Im\{Z/n\}$ does not depend very strongly on ϵ_r.

These analytical results were cross-checked with numerical simulations using a wire under CST Microwave Studio and HFSS [7, 13]. A typical geometry used is shown in Fig. 5. For not too small layer thicknesses ($t \geq 1$ mm) very good agreement was found; for much smaller t the simulations get problematic for convergence issues. It was also verified that $\Im\{Z/n\}$ is proportional to the dielectric cross-section in the case when the dielectric does not cover the full azimuth.

To give concrete examples Z/n was estimated for chamber geometries similar to the CERN PS and SPS for electrodes all around the ring:

- PS: Round 50 mm radius chamber, one single 25 mm wide and 0.1 mm high strip (corresponds to reference geometry): $\Im\{Z/n\} \approx 0.07\ \Omega$.
  This should be compared to today's machine impedance in the broad-band resonator parameters with $Z/n \approx 20\ \Omega$, $Q \approx 1$ at the resonance frequency $f_r \approx 1$ GHz.
- SPS: Round 25 mm radius chamber, one single 20 mm wide and 0.1 mm high strip: $\Im\{Z/n\} \approx 0.3\ \Omega$.
  Today's machine impedance: $Z/n \approx 7\ \Omega$, $Q \approx 1$ and $f_r \approx 1$ GHz.

These results were cross-checked with simulations done using GdfidL, showing a very good agreement [14, 15].

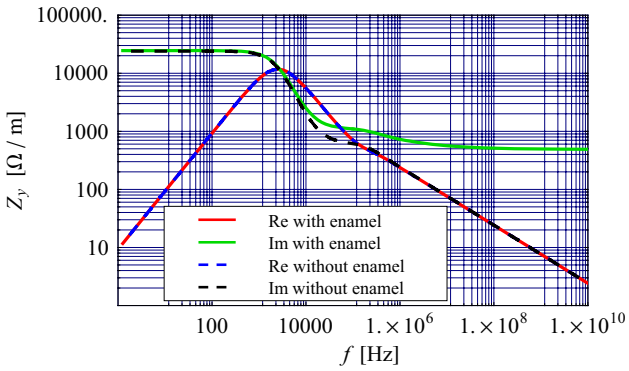

Figure 6: Calculation of the transverse impedance of a 0.5 mm thick dielectric layer ($\epsilon_r = 5$) inside a 2 mm thick stainless steel pipe with 50 mm radius and 1 m length. For this rotationally symmetric structure the Burov-Lebedev formula was used.

Transverse impedance

The transverse impedance Z_{TR} of a multi-layer structure with rotational symmetry can be determined from the Burov-Lebedev formula [16]. As a first step Z_{TR} was calculated for a thin layer covering the entire azimuth of a stainless steel pipe and compared to a reference pipe without dielectric (Fig. 6). Dielectric losses were neglected. A similar geometry was then examined using numerical simulations using CST Microwave Studio (Fig. 7). The analytical results were reproduced and other electrode geometries tested, in particular longitudinal dielectric stripes. The properties of Z_{TR} are as follows:

- At very low frequencies there is no change with respect to the resistive wall impedance of the reference pipe.
- Above 10 kHz $\Im\{Z_{TR}\}$ is increased, whereas $\Re\{Z_{TR}\}$ is not affected.
- For thin layers $\Im\{Z_{TR}\}$ is proportional to the layer thickness.

When the coating is reduced to strips at the top and bottom of the beam pipe, the horizontal $Z_{TR,x}$ is significantly decreased, whereas there is only a rather small impact on the vertical $Z_{TR,y}$. For two electrodes covering 36° each $Z_{TR,y}$ goes down by about a factor two. For strips much narrower than the chamber radius $Z_{TR,y}$ is proportional to the strip width.

In the following rectangular chamber geometries as in EC build-up simulations in [17] were used (Fig. 8). Scaling the results for the CERN PS and SPS we find for electrodes all around the machine circumference as a first approximation:

- PS: 80×40 mm half axes, one single 25 mm wide and 0.1 mm high strip: $\Im\{Z_{TR}\} \approx 0.04$ MΩ/m,
  compared to today's machine impedance in the broad-band resonator parameters with $Z_{TR} \approx 3$ MΩ/m, $Q \approx 1$ and $f_r \approx 1$ GHz.

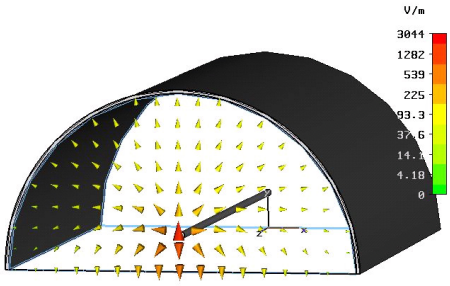

Figure 7: Simulation of the Z_{TR} of a dielectric coating inside a circular beam pipe.

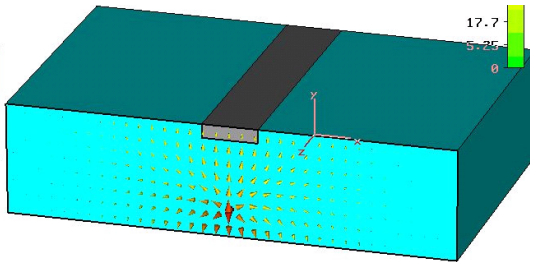

Figure 8: Simulation of the Z_{TR} of a thin dielectric strip inside a flat beam pipe.

- SPS: 80×20 mm half axes, one single 20 mm wide and 0.1 mm high strip: $\Im\{Z_{TR}\} \approx 4$ MΩ/m, compared to today's $Z_{TR} \approx 20$ MΩ/m, $Q \approx 1$ and $f_r \approx 1$ GHz.

The large difference between the two machines comes from the smaller SPS chamber size, which enters with the third power, and the larger SPS circumference. A cross-check with GdfidL results showed good agreement [14]. It would be possible to reduce $Z_{TR,y}$ by installing two off-center electrodes, however $Z_{TR,x}$ rises significantly in this case and the clearing efficiency for a given voltage decreases.

CLEARING EFFICIENCY

The clearing efficiency of several electrode types was simulated for the case of the PS straight section chamber at top energy using the ECLOUD code, which was modified so as to read in the transverse electric field generated for various clearing electrode geometries [11]. The latter was computed by a CST EM Studio simulation on a 2-D grid. A small dipolar magnetic field of $B = 10$ Gauss was used, since the studies were aimed at verifying that EC build-up can be expected in the PS in straight sections equipped with a small dipole. The simulation parameters are summarized in Table 1. Three different electrode geometries were examined:

- a 46 mm wide metallic electrode.
- a 20 mm wide electrode on a thin dielectric layer in the center of the beam pipe.
- a single 20 mm wide electrode on a thin dielectric layer with 30 mm offset from the beam pipe center.

Parameter	Value
proton momentum [GeV/c]	26
number of bunches	72
protons per bunch	$1.15 \cdot 10^{11}$
bunch spacing [ns]	25
gap length [μs]	0.4
rms bunch length [m]	0.75
rms momentum spread	$2.30 \cdot 10^{-4}$
rms trans. norm. emittance [μm]	3.00
σ_x [mm]	1.58
σ_y [mm]	0.42
β_x [m]	20
β_y [m]	12
horizontal dispersion D_x [m]	2.5
chamber half width [mm]	73
chamber half height [mm]	35
maximum SEY yield δ_{max}	1.5
electron energy at δ_{max} [eV]	239.5
pressure [nTorr]	10
magnetic field [Gauss]	10
electrode bias voltage [V]	-1000

Table 1: Parameters used in the EC build-up simulation performed with the ECLOUD code. The case of the elliptical PS vacuum chamber was analysed.

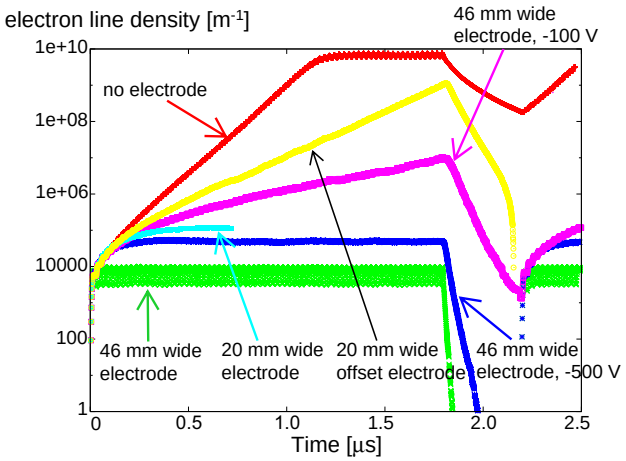

Figure 9: Simulation of the clearing efficiency for different electrode geometries having a clearing voltage of -1 kV at PS top energy (26 GeV/c).

The results are plotted in Fig. 9. With the assumed parameters the EC saturates for an electron line density of almost 10^{10} m^{-3} (red trace). The wide electrode works best, but also the 20 mm wide centered electrode is effective for a -1 kV clearing voltage. The off-center electrode does not suppress the EC build-up for the given clearing voltage. Varying the magnetic field, it was found that the EC saturation line density does not increase monotonically with B. At $B = 10$ Gauss the build-up is more pronounced than at $B = 100$ Gauss.

TECHNOLOGICAL ISSUES

The considered electrode geometry requires the deposition of a thin dielectric layer inside the beam pipe. Due to the stringent requirements of the accelerator environment the properties of this dielectric are critical for the application. For reasons of dielectric strength, a thickness of about 0.1 mm or more is necessary. Potential technologies are the application of enamel and plasma spraying. Enamel has good mechanical stability, strength and adhesion and good thermal contact to the beam pipe. Its dielectric strength is good and it can stand baking at $300°$ or more [18, 19, 20]. Plasma spraying offers similar features, however for both technologies vacuum properties, SEY and radiation hardness have to be analysed in more detail.
On top of the dielectric, a highly resistive coating, preferably in thick-film technology, has to be applied. Its surface resistance $R_\square$ must be chosen higher than the free space impedance of $Z_0 = 377\ \Omega$ ("invisibility" condition) but small enough that the voltage drop along the electrode is not too high. Values of $R_\square = 10$ kΩ to 100 kΩ appear to be suitable. There is a large body of experience with thick film coated surfaces in ultra-high vacuum applications [5, 9]. The SEY of thick-film layers should be determined by measurements.

CONCLUSION

The concept of distributed electron cloud clearing electrodes installed in an accelerator beam pipe has been discussed. Any electrode should fulfil a number of requirements, including mechanical stability, vacuum compatibility and low beam coupling impedance. The latter can be achieved with a highly resistive layer applied on a dielectric strip, since it acts as a bulk dielectric if the surface resistance of the resistive layer is much larger than the free space impedance. In order to minimize the impedance of such a structure as well as the aperture reduction, the dielectric should be made as thin as possible. A thickness of the order of 0.1 mm should be possible for a layer that stands typical clearing voltages of about 1 kV. Vitreous enamel appears to be an interesting candidate for the dielectric, but vacuum properties and other issues should be checked in more detail. Furthermore, the clearing efficiency of a typical electrode geometry was confirmed in numerical simulations.

ACKNOWLEDGEMENTS

We would like to thank Joerg Wendel, Peter Hellmold and Franz-Josef Behler from the German enamel industry for the fruitful exchange of ideas. Thanks to Warner Bruns and Elena Benedetto for inspiring discussion.

REFERENCES

[1] Pedersen, F., Poncet, Alain., Soby, L., *The CERN antiproton accumulator clearing system with ion current measurements as a residual neutralization diagnostic*, CERN-PS-89-17-ML, Geneva (1989)

[2] Wang, L. F., *Mechanism of electron cloud clearing in the accumulator ring of the Spallation Neutron Source*, PRST 7, 034401 (2004)

[3] Wei, L. et al., *Electron Cloud Effects: Observations, Mitigation Measures, and Challenges in RHIC and SNS*, CARE-HHH-APD Workshop 2004, CERN, Geneva (2004)

[4] Tavares, P. F., *Ion Clearing in the LNLS UVX-2 Soft X Ray Source*, Proceedings of the EPAC 1992, Berlin (1991)

[5] Spataro, B., Zobov, M., *Wake Fields and Coupling Impedance of the Daphne Electron Ring*, Daphne Technical Note G-64 (2005)

[6] McIntyre, P. M., *Killing the Electron Cloud Effect in the LHC Arcs*, Proceedings of the PAC 2005, Portland (2005)

[7] http://www.cst.com

[8] Zimmermann, F., *Beam Sizes in Collision and Electron-Cloud Suppression by Clearing Electrodes for KEKB*, CERN-SL-Note-2001-022, Geneva (2001)

[9] Caspers, F., Delahaye, J. P., Godot, J. C., Hubner, K., Poncet, A., *EPA beam-vacuum interaction ion clearing system*, Proceedings of the EPAC 1988, Rome, CERN-PS-88-37-ML (1989)

[10] Chen, F. F., *Introduction to Plasma Physics and Controlled Fusion*, Vol. 1, Plenum Press, New York (1984)

[11] Zimmermann, F. and Kroyer, T., *Simulations of Clearing Electrodes for PS & PS2*, ECL2 Workshop, http://indico.cern.ch/getFile.py/access?contribId=29&sessionId=6&resId=3&materialId=slides&confId=11937, Geneva (2007)

[12] Kroyer, T., Caspers, F., *Longitudinal and Transverse Wire Measurements for the Evaluation of Impedance Reduction Measures on the MKE Extraction Kickers*, to be published as CERN-AB-RF note (2007)

[13] http://www.hfss.com

[14] Bruns, W., *Impedance of clearing electrodes with GdfidL*, ECL2 workshop, http://indico.cern.ch/contributionDisplay.py?contribId=42&sessionId=9&confId=11937 (2007)

[15] http://www.gdfidl.de

[16] Burov, A., Lebedev, V., *Transverse Resistive Wall Impedance for Multi-layer Round Chambers*, EPAC 2002, Paris (2002)

[17] Furman, M. A., *E-Cloud in PS2, PS+, SPS+*, Proceedings LHC-LUMI-06 (2006)

[18] Behler, F.-J., Nose, G., Kunkel, H., *Industrial Enamel – Foundations, production, applications and CERN-tests*, these proceedings (2007)

[19] Biscardi, C., Hseuh, H. and Mapesa, M., *Application of porcelain enamel as an ultra-high-vacuum-compatible electrical insulator*, J. Vac. Sci. Technol. A 18.4. (2000)

[20] Severgin, Yu. P., Filimonov, M. Z., *Insulating and Metal-Ceramic Materials for Particle Accelerators*, PAC 1993, Washington, DC, USA (1993)

RESISTIVE WALL WAKES AND CLEARING ELECTRODES*

R. Wanzenberg#, DESY, Hamburg, Germany

Abstract

One electron and one positron damping ring are foreseen for the International Linear Collider (ILC). Damping rings are necessary to reduce the emittances delivered by the particle sources to the small values required for luminosity production. In this paper the effect of resistive wall wakes on the clearing electrodes, which are one option to mitigate or suppress the effects due to electron clouds, are investigated. Furthermore the resistive wall effects of NEG coating and the implications on transverse mode coupling instabilities are presented.

INTRODUCTION

Damping rings are necessary to reduce the emittances obtained from the particle sources to the design values of the linear collider. In the recent reference design of the International Linear Collider (ILC) [1] one electron and one positron damping ring, each about 6.7 km long, are foreseen. The main parameters of the damping rings are listed in Table 1.

Table 1: ILC DR Parameters

Parameter	ILC DR
Energy / GeV	5
Circumference /m	6695
RF Frequency / MHz	650
RF harmonic number	14516
RF Voltage / MV	24
Momentum compaction	1.22 10-3
Synchrotron tune	0.067
Total current / mA	376
Number of bunches	2625
Bunch population / 10^{10}	2.0
Bunch separation / ns	7.69
Emittance (horz.) /nm	0.51
Bunch length / mm	9
Damping time H/V/L / ms	25.7 / 25.7 / 12.9

In positron storage rings electrons produced by photoemission, ionization and secondary emission accumulate in the vacuum chamber forming an “electron cloud”. The interaction of the electron cloud with the positron beam can cause transverse single bunch instabilities [2] leading finally to an emittance blow up. These effects have been studied in [3, 4] using computer simulations and analytical estimates.

Simulations indicate that the use of clearing electrodes is an effective method to suppress the electron effects [5, 6, 1]. Furthermore it has been proposed to use TiVrZr films as an effective getter material (NEG pump) with a low secondary emission coefficient inside the vacuum system of the damping rings [7].

CLEARING ELECTRODES

There exist different designs for the clearing electrodes to minimize the effect of the geometric impedance. A schematic layout of a clearing electrode is shown in Fig. 1. A metallic electrode is mounted in the vacuum pipe using feed-throughs.

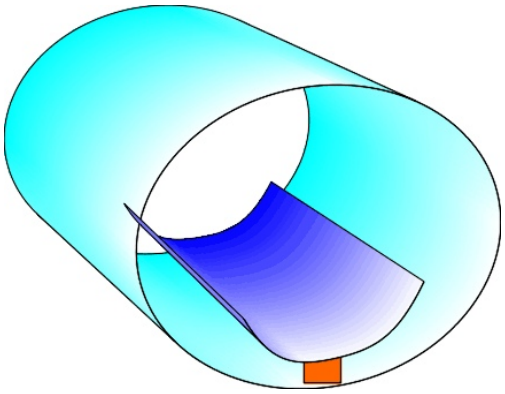

Figure 1: Schematic layout of a clearing electrode.

In addition, other designs with continuous clearing electrodes based on double layers of enamel coating have been proposed [8,9,10]. The calculation of the resistive wall wakefields, which are presented in this paper, are based on metallic surfaces in a round beam pipe. It is assumed that enamel layers are not visible for the beam, which is a rather crude approximation.

RESISTIVE WALL WAKEFIELD

The wake field due to the resistivity of the metallic wall has been calculated for various geometries [11, 12, 13, 14, 15]. To estimate the resistive wall wake fields for the damping ring the results for a round vacuum chamber have been used [12]. The normalized longitudinal and transverse wake potential for a Gaussian bunch are shown in Fig. 2.

From the wake potential the total loss parameter and the kick parameter are calculated:

$$k_{loss} = \int ds\ \lambda(s)\ W_{\parallel}(s) \tag{1}$$

$$k_{\perp} = \int ds\ \lambda(s)\ W_{\perp}(s) \tag{2}$$

*Work supported by the Commission of the European Communities Contract No. RIDS-011899.

#Rainer,Wanzenberg@desy.de

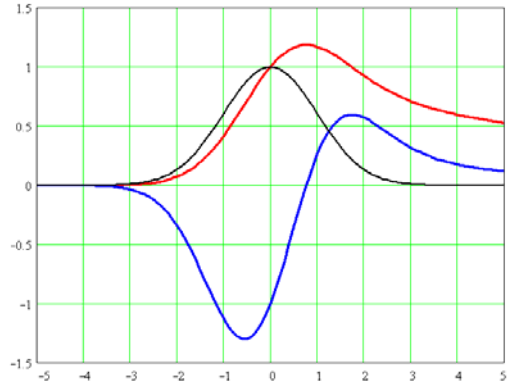

Figure 2: Normalized longitudinal (blue line) and transverse (red line) resistive wall wake potential of an Gaussian bunch (black line).

For a round beam pipe with radius r and conductivity σ_{cond} the loss and kick parameter are [13, 15]:

$$k_{loss} = \frac{1}{4\pi^2\sqrt{2}}\Gamma(\tfrac{3}{4})\ \frac{c}{r\ (\sigma_z)^{3/2}}\sqrt{\frac{Z_0}{\sigma_{cond.}}}, \qquad (3)$$

$$k_{\perp} = \frac{1}{2\pi^2\sqrt{2}}\Gamma(\tfrac{1}{4})\frac{c}{r^3\sqrt{\sigma_z}}\sqrt{\frac{Z_0}{\sigma_{cond}}}, \qquad (4)$$

where Z_0 is the impedance of free space (378 Ω), σ_z is the bunch length and Γ is the gamma function. The conductivity of copper, stainless steel and NEG material are summarized in Table 2.

Table 2: Conductivity of materials

Material	Conductivity /(Ωm)$^{-1}$
copper	58.0 x 10^6
steel	1.5 x 10^6
NEG	0.31 x 10^6
Enamel	~ 0

The loss parameter can be used to calculate the transient power loss, according to the formula:

$$P_{loss} = N_{bunches}\ f_0\ q_b^{\,2}\ k_{loss}, \qquad (5)$$

where $N_{bunches}$ is the total number of bunches, f_0 the revolution frequency (see table 1) and q_b the single bunch charge.

The threshold for the transverse mode coupling instability can be calculated from the betratron tune shift [16]:

$$\Delta Q_{\beta} = \frac{I_B \langle\beta\rangle T_0}{4\pi E/e} k_{\perp}, \qquad (6)$$

which depends on the kick parameter. In formula (6) I_B is the single bunch current, <β> is the average beta function, T_0 is revolution time and E is the energy of the beam.

MODE COUPLING INSTABILITIES

Using the parameters from table 1 for the ILC damping ring design and assuming a vacuum pipe radius of 20 mm the kick parameter has been calculated for copper and NEG material. The results are show in Table 3:

Table 3: tune shift and kick parameters for the ILC DR

Material	$\Delta Q/Q_s$	$k_{\perp}$ (V/pC/m/m)
copper	0.017	0.13
NEG	0.23	1.79

An average beta function of 25 m and a single bunch current of 0.143 mA have been used to calculate the tune shift due to the wall resistivity. The tune shift has been normalized with respect to the synchrotron tune Q_s. The tune shift for copper is very small. But even the larger tune shift for NEG material is still acceptable. It should be mentioned that the calculated kick parameter for NEG material is based on a rather pessimistic model assuming that all wall losses occur in the NEG material. But the NEG layer is usually much thinner than the skin depth, which can be calculated from the following formula:

$$\delta(\sigma_{cond.},\omega) = \sqrt{\frac{2}{\mu_0\ \sigma_{cond.}|\omega|}} \qquad (7)$$

For the rms frequency of the bunch spectrum, $\omega = c/\sigma_z = 2\pi\cdot 5.3\ \mathrm{GHz}$, one obtains a skin depth of 12.64 μm for NEG material and 0.9 μm for copper. The typical thickness of a NEG layer is only 1 μm.

A smaller pipe radius will give a significantly larger tune shift since the kick parameter scales with the third power of the inverse radius.

HEATING OF CLEARING ELECTRODES

The total power loss in the clearing electrode can be calculated from the total loss parameter, formula (3) and (5), or from the longitudinal resistive wall impedance:

$$P_{loss} = \Gamma(\tfrac{3}{4})\frac{\sigma_z}{c}\frac{N_{bunches}}{T_0}\ \hat{I}^2\ \mathrm{Re}(Z_{\parallel}(\omega = \tfrac{c}{\sigma_z})) \qquad (8)$$

where $\mathrm{Re}(Z_{\parallel}(\omega))$ is the real part of the resistive wall impedance and $\hat{I}$ the peak beam current. The resistive wall impedance of a clearing electrode with length L and an angular extension ϕ (see Fig.3) is

$$Z_{\parallel}(\omega) = (1\mp i)\frac{\phi}{2\pi}L\sqrt{\frac{|\omega|\mu_0}{2\sigma_{cond.}}} = (1\mp i)\frac{\phi}{2\pi}\frac{L}{\delta(\sigma_{cond.},\omega)}\frac{1}{\sigma_{cond.}}. \qquad (9)$$

The total power loss and the loss parameter per meter for a pipe radius of 20 mm and $\phi = 2\ \pi$ is summarized in Table 4.

Table 4: power loss and loss parameter per meter

Material	P_{loss}(W/m)	$k_{\parallel}$ (V/nC/m)
copper	1.18	0.98
NEG	16.2	13.4

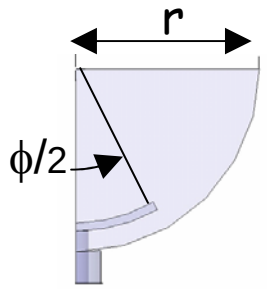

Figure 3: Cross section of a clearing electrode (schematic)

The temperature T of the clearing electrode can be estimated from the Stefan-Boltzmann Law:

$$T = \sqrt[4]{\frac{P_{loss}}{\varepsilon_{th}\,\phi\, r\, L\ \ c_{StB}} + T_E{}^4}, \qquad (10)$$

$$c_{StB} = 5.67 \cdot 10^{-8} \frac{\mathrm{W}}{\mathrm{m}^2\,\mathrm{K}^4},$$

where T_E is the environment temperature (beam pipe), ϕ r L is the radiating area of the electrode and ε_{th} is the thermal emission constant of the electrode, which is equal to one for black body radiation. It is assumed that the clearing electrode is in poor thermal contact with the environment via the feed-throughs. The temperature increase:

$$\Delta T = T - T_E \qquad (11)$$

has been calculated for copper and NEG material:

Table 5: Temperature increase of the clearing electrode

Material	ΔT / K $\varepsilon_{th} = 1$	ΔT / K $\varepsilon_{th} = 0.5$
copper	1.4	2.7
NEG	17.5	32.6

These results do not depend on the angular extension of the electrode since:

$$\hat{I}^2 \sim \phi^2, \quad Z_{\parallel} \sim \phi, \quad P_{loss} \sim \phi. \qquad (12)$$

CONCLUSION

The loss and kick parameters for a resitive wall have been calculated for the ILC damping ring for different materials. The betatron tune shifts seems to be tolerable even if the whole vacuum system is coated with NEG material. Therefore no transverse mode coupling instability due to the resistive wall is expected. The dissipated power in the chamber wall is about 1 W/m for a copper chamber and 16 W/m for chamber made from NEG material. The heating of an isolated clearing electrode is small if the electrode is made from copper.

REFERENCES

[1] "International Linear Collider Reference Design Report 2007", ILC-REPORT-2007-001

[2] K. Ohmi, F. Zimmermann "Head-tail instability caused by electron cloud in positron storage rings", Phys.Rev.Lett.85:3821-3824, 2000.

[3] M. Pivi et al., "Single- Bunch Instability Driven by the Electron Cloud Effect in the Positron Damping Ring of the International Linear Collider", PAC05, Knoxville, Tennessee, May 2005

[4] M. Pivi et al., "Simulation of the Electron Cloud for Various Configurations of a Damping Ring for the ILC", EPAC'96, Edinburgh, Scotland, June 2006.

[5] F. Zimmermann, "Beam Sizes in Collision and Electron-Cloud Suppression by Clearing Electrodes for KEKB," CERN-SL-Note-2001-022, May 2001.

[6] P. McIntyre, A. Sattarov, "Killing the electron cloud effect in the LHC arcs", PAC05 Knoxville, May 2005

[7] B. Henrist, N. Hilleret, C. Scheuerlein, M. Taborelli, "The Secondary Electron Yield of TiZr and TiZrV Non-Evaporable Getter Thin Film Coatings", Applied Surface Science 172, 95 (2001)

[8] J. Wendel, "Vitreous enamel - an efficient material component", these proceedings

[9] F.-H. Behler, "Vitreous enamel - foundations, production, applications and CERN tests", these proceedings

[10] T. Kroyer, F. Caspers et al., "Impedance of clearing electrodes with HFSS" , these proceedings

[11] A. Chao, "Physics of Collective Beam Instabilities in High Energy Accelerators", Wiley, New York 1993

[12] A. Piwinski, "Wake Fields and Ohmic Losses in Round Vacuum Chambers", DESY HERA 92-11, May 1992

[13] A. Piwinski, "Wake Fields and Ohmic Losses in Flat Vacuum Chambers", DESY HERA 92-04, Jan 1992

[14] A. Piwinski, "Impedances in Lossy Elliptical Vacuum Chambers", DESY 94-068, April 1994

[15] O. Henry, O. Napoly, "The Resistive-Pipe Wake Potentials for Short Bunches", Part Acc. 1991, (35), 235-247

[16] K. Balewski, "Analyse der transversalen Moden-Kopplungsinstabilitaet fuer lokalisierte HF-Strukturen und ihre Kompensierbarkeit durch Rueckkopplungssystemen, DESY 89-108, Aug. 1989

ELECTRON CLOUD STUDIES AT CESR-C AND CESR-TA*

M.A. Palmer# for the CESR-TA Working Group, Cornell Laboratory for Accelerator-Based Sciences and Education, Ithaca, NY 14853, U.S.A.

Abstract

A program to characterize electron cloud build-up in the Cornell Electron Storage Ring (CESR) has recently begun. This paper provides a brief overview of the work that has been done to date and describes future plans to use CESR as a test accelerator (CESR-TA) for the International Linear Collider (ILC) Damping Rings. As part of this program we plan to study the impact of the electron cloud on ultra low emittance beams and will undertake measurements of electron cloud growth and suppression in the CESR-c wigglers which were selected for the baseline ILC design.

INTRODUCTION

The ILC Reference Design Report (RDR) specifies single electron and positron damping rings (DR), each wih a circumference of 6.7 km [1]. A significant concern for the positron ring is the build-up of the electron cloud (EC) and the potential for EC induced instabilities which can limit the performance of the ring and ultimately the luminosity performance of the collider. Studies carried out for the RDR indicate that the positron DR is likely to operate above the EC instability threshold unless satisfactory mitigation techniques can be demonstrated in the wiggler and dipole chambers. Thus one of the highest R&D priorities for the ILC DR group over the next few years is demonstrating technical solutions in these chambers. In addition, the large extrapolation from conditions in any currently operating positron ring to those of the ILC damping rings requires that we carefully benchmark simulations of the EC growth and its impact on the beam. Thus experimental studies with parameters more closely approximating the DR parameters are highly desirable. One option for obtaining additional data in a regime that closely approaches the ILC DR parameters is to carry out an experimental program at CESR at the conclusion of the CLEO-c/CESR-c colliding beam physics program in early 2008.

THE PROPOSED CESR-TA PROGRAM

The CESR-TA program offers several unique opportunities for carrying out ILC DR R&D. The CESR-c damping wigglers are the baseline technology choice for the ILC damping rings due to their large physical aperture, which is critical for the acceptance of the positron DR, and their excellent field quality, which ensures that the dynamic aperture of both rings is acceptable [2-3]. In its low energy configuration (beam energies between 1.5 and 2.5 GeV) with 12 damping wigglers, CESR operates as a wiggler-dominated storage ring. By placing the 12 wigglers in zero dispersion regions, CESR will be capable of reaching ultra low emittances in this mode. The full energy range of the ring is 1.5 – 5.5 GeV. This flexible energy range will allow key system tests at the ILC DR operating energy as well the ability to characterize and differentiate beam dynamics issues through their energy dependence. Finally, the ability to store both positrons and electrons in the same ring will allow us to clearly distinguish species-dependent effects.

The goal of the CESR-TA program will be to support key R&D on the timescale of the ILC Engineering Design Report (EDR) which is targeted for publication in 2010. We intend to offer a program complementary to the ongoing research program at the KEK-ATF. Such a program will help satisfy the needs for ILC DR experimental studies as research at ATF begins to focus more heavily on beam delivery system studies as part of ATF-II [4]. By offering dedicated experimental runs along with flexible shutdown periods to install experimental hardware, we hope to provide a flexible venue for research by our ILC DR collaborators.

Specific experimental plans include the study of EC growth and suppression in wiggler, dipole and quadrupole vacuum chambers and instrumenting key sections of the ring with EC diagnostics. We intend to explore a range of EC mitigation techniques including clearing electrodes, coatings and, possibly, grooved chambers. The ability to operate the ring with positrons and electrons will permit the exploration of ion-related issues for the electron DR. By configuring CESR for ultra low emittance operation, we will be able to explore the onset of EC induced instabilities and the sources of emittance growth for beams with parameters in the same regime as those in an ILC DR. Correction algorithms to achieve ultra low emittance and tuning methods to maintain these conditions will be studied along with developing instrumentation to characterize these extreme beams.

ELECTRON CLOUD MEASUREMENTS AT CESR

A series of measurements have recently been undertaken to characterize the electron cloud generated around CESR. Table 1 summarizes several key parameters of the ring. Our measurements rely heavily on a set of multi-bunch beam instrumentation that has been recently implemented [5-6]. This instrumentation includes beam position monitor (BPM) readout

*Work supported by the U.S. National Science Foundation and the U.S. Departument of Energy
#map36@cornell.edu

electronics that can digitize the position of all bunches in the ring in parallel on a turn-by-turn basis. It also includes vertical beam size monitors (BSM) based on the Hamamatsu H7260K linear photomultiplier (PMT) array (1mm x 32). This PMT provides sub-nanosecond rise times which allows for digitization of the beam profiles for individual bunches in the machine. As with the BPM readout system, data from all bunches can be digitized in parallel on a turn-by-turn basis.

Table 1: Some CESR Parameters

Parameter	**Value**
Circumference	768.44 m
Revolution Frequency	390.13 kHz
RF Frequency	499.76 MHz
Harmonic Number	1281
Total bunches	183 (=1281/7)
Bunch Spacing	14 ns

For our initial characterization of EC effects, we have typically employed 45 bunch trains with a bunch spacing of 14 ns, the standard CESR bunch spacing. We have used our multi-bunch BPM system to digitize 1024 turn-by-turn position samples in parallel from all bunches in the machine. In order to clearly observe the tunes for each bunch, a set of pulsed magnets are used to excite the beam and then the beam position for all bunches are digitized in parallel as the transverse motion freely damps. Early attempts to sequentially collect data on multiple bunches with a single bunch readout system did not yield reliable differential tune data because of their sensitivity to slow variations in the global tune over the course of the measurements. These issues were resolved with the installation of the fully parallel readout.

Figure 1 shows the results from a series of bunch-by-bunch tune measurements where a 10-bunch train of positrons was used to generate the EC and then witness bunches were placed at various distances behind the train. The data was taken during 1.9 GeV operations in a lattice with 12 active wigglers. In this case, all bunches were filled to the same bunch current of 0.75 mA corresponding approximately 1.2×10^{10} particles/bunch. The tunes of all bunches are plotted relative to the tune of the leading bunch in the train. In a simple model of the interaction between the EC and the beam, the cloud density required to produce the vertical tune shift along the train is $\rho_e \sim 10^{11}/m^3/kHz$ [7]. We note that the vertical tune data is consistent with the witness bunches seeing a cloud density that decays with a nominal time constant of roughly 170 ns. In contrast with the vertical tune shifts, the horizontal tune shifts show very little variation down the length of the train.

For comparison with the positron data, the same series of measurements was carried out for an electron beam.

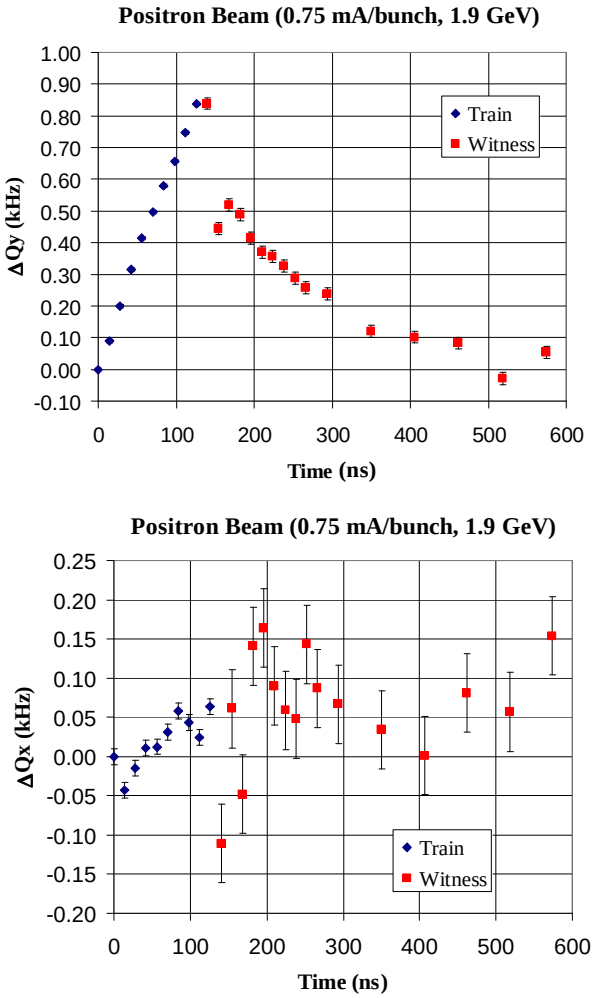

Figure 1: Results of a series of witness bunch studies using a positron beam. An initial train of 10 bunches is employed as a generator of the EC. Tune measurements were made for bunches in the leading train as well as a witness bunch located some distance behind the train. The top plot shows the shift in vertical tune of each bunch relative to the leading bunch. The bottom plot shows the same information for the horizontal tune. The nominal first bunch tunes were f_x=202.7 kHz and f_y=239.3 kHz.

Figure 2 shows the observed tune shifts. The first thing to note is that the sign of the tune shift is consistent with the EC acting on an electron beam. A separate set of measurements with 45 bunch trains has shown that, in these conditions, the tune shift for the electron beam saturates at approximately 1/5th the saturation level observed for the positron beam. The magnitude of the slope of the tune shift versus bunch for bunches in the leading train is approximately 26% of that observed for the positron train. For the later witness bunches, the vertical tune shift decays with a time constant in excess of 100 ns in a similar fashion as observed for the positron beam.

Another point to note is that the tune shift of the first few witness bunches after the leading train continues to

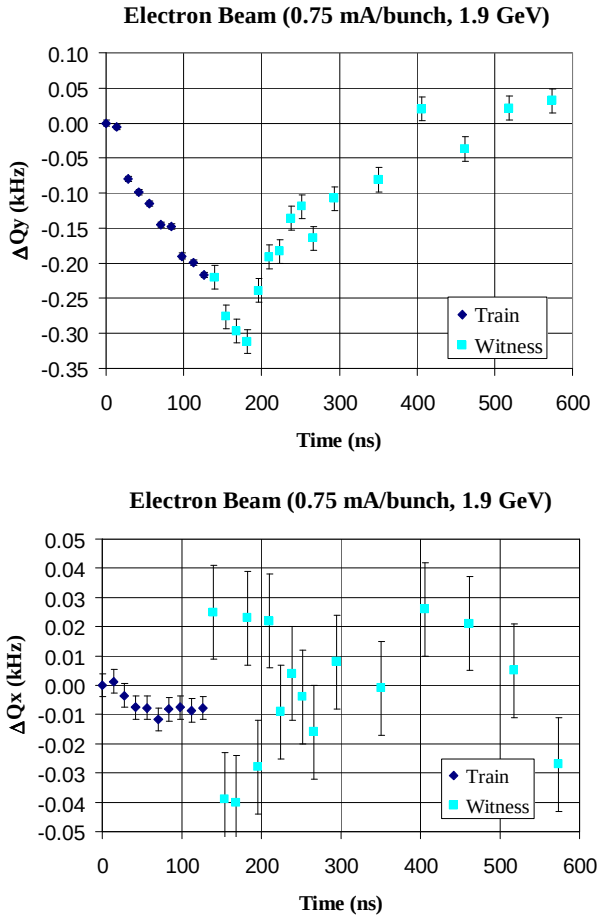

Figure 2: Results of a series of witness bunch studies using an electron beam. An initial train of 10 bunches is employed as a generator of the EC. Tune measurements were made for bunches in the leading train as well as a witness bunch located some distance behind the train. The top plot shows the shift in vertical tune of each bunch relative to the leading bunch. The bottom plot shows the same information for the horizontal tune. The nominal first bunch tunes were f_x=203.7 kHz and f_y=241.4 kHz.

grow. We hypothesize that this may be due to the electron cloud equilibrating to higher densities near the beam axis after the end of the train has passed. We are starting to investigate this behavior in simulation to help understand this observation in detail.

Our preliminary conclusion from the above tune measurements is that we are seeing evidence for the electron cloud affecting the dynamics of both electron and positron beams.

Figure 3 shows plots of a series of measurements of the vertical beam size along 45 bunch trains of positrons for a range of bunch currents. Each point consists of the average of 200 50-turn samples. A Gaussian fit to each 50-turn sample provides profile information. The 50-turn averaging of the PMT signals mixes the effects of centroid motion and incoherent beam blowup. Subsequent measurements have demonstrated that both effects are present after the onset of the instability. The onset of the instability in each case occurs when approximately 1.5×10^{11} beam particles have preceded the first bunch exhibiting the instability.

PREPARATION FOR THE CESR-TA PROGRAM

Design studies have been carried out to characterize our ability to utilize CESR as a test bed for key ILC damping rings R&D [8]. Table 2 summarizes CESR-TA operating parameters for the 2.0 GeV baseline lattice intended for ultra low emittance operation. Studies of the alignment sensitivities for the CESR-TA lattice indicate that, with a careful program of magnet alignment, we should be able to correct the ring to give a vertical emittance of a few to several pm (< 8 pm at 95% C.L.). In order to characterize these ultra low emittance beams, we are developing a fast x-ray camera based on GaAs diode technology. Such a device offers the possibility of measuring beam sizes of individual bunches with micron resolution. With a suitable x-ray optics system, this type of device has the potential to make turn-by-turn profile measurements of all bunches in a train.

Table 1: CESR-TA Baseline Lattice Parameters

Parameter	Value
No. of Wigglers	12
Wiggler Field	2.1 T
Beam Energy	2.0 GeV
Energy Spread ($\Delta E/E$)	8.6×10^{-4}
Vertical Emittance	5 – 10 pm
Horizontal Emittance	2.25 nm
Transverse Damping Time	47 ms
Q_x	14.57
Q_y	9.62
Q_z	0.075
Total RF Voltage	8.5 MV
Bunch Length	9 mm
Momentum Compaction	6.4×10^{-3}

In May 2007, the first retarding field analyzers to characterize local EC build-up in the CESR ring will be installed. Development is also underway on a vacuum chamber with collectors that can be employed to characterize EC growth in the CESR-c damping wigglers. We are collaborating with colleagues at SLAC and LBNL to build wiggler chambers in which EC mitigation techniques are implemented for installation and testing in the middle of 2008. Initial tests are planned for a chamber coated with NEG and a chamber with a clearing electrode. Between now and the start of CESR-TA operations in the spring of 2008, we intend to pursue a preparatory program of machine studies to explore EC issues and lattices for low emittance operation in CESR.

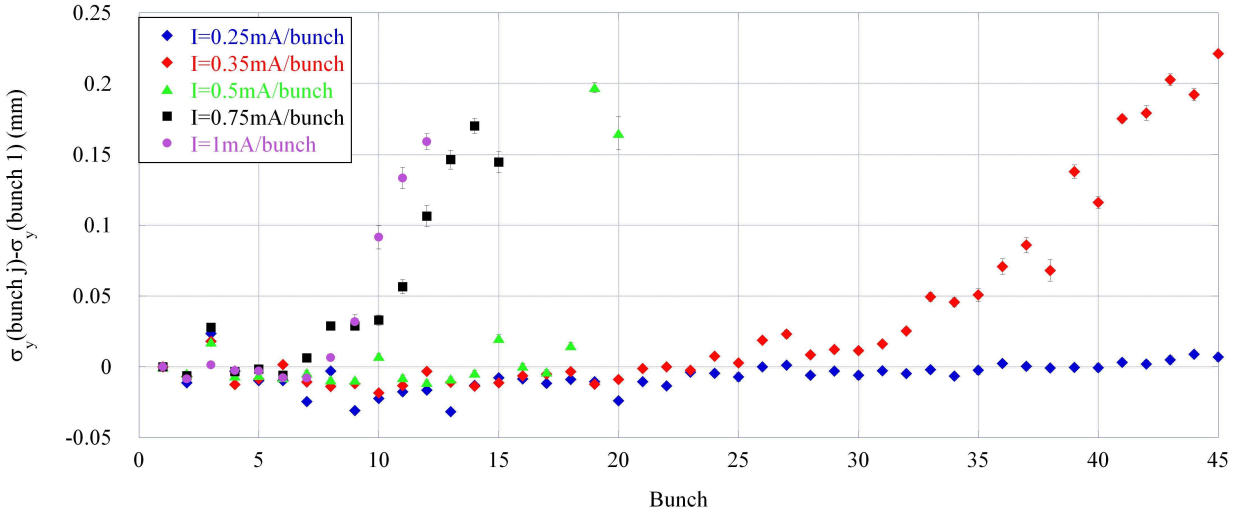

Figure 3: Onset of a vertical beam size instability for trains of 45 positron bunches as a function of bunch current. For the measurements shown, each point corresponds to the average of 200 single bunch beam size fits where each fit was carried out on a 50-turn average of the PMT array signals.

CONCLUSIONS

Beam measurements at CESR show evidence for generation of an EC along a train of positron bunches and the development of an EC-induced instability for bunches at the end of sufficiently intense trains. Similar measurements with trains of electron bunches show tune shifts along the trains which are also consistent with the presence of the EC, but with smaller magnitude than seen for positron beams. Work is underway to understand these observations in greater detail via simulation.

Starting in 2008, we hope to begin a dedicated program to study the EC with ultra low emittance beams and to help validate suitable EC mitigation techniques for the ILC damping rings. A proposal to support this effort has recently been submitted jointly to the U.S. NSF and the U.S. DOE.

ACKNOWLEDGMENTS

This overview draws heavily on work from members of the CESR operations group and the CESR-TA working group. This includes: J. Alexander, M. Billing, G. Codner, J. Crttenden, M. Ehrlichman, M. Forster, D. Hartill, R. Helms, D. Rice, D. Rubin, D. Sagan, L. Schachter, J. Shanks (MSU), E. Tanke, M. Tigner and J. Urban. In addition, the work has benefited from discussions and visits by several collaborators including: J. Flanagan (KEKB), K. Harkay (ANL), R. Holtzapple and J. Kern (Alfred University), A. Molvik (LLNL), and M. Pivi (SLAC).

REFERENCES

[1] G. Aarons, et al., "International Linear Collider Reference Design Report," ILC-REPORT-2007-01, p. 2.4-1, http://ilcdoc.linearcollider.org/getfile.py?docid=125&name=ILC_RDR_2007-04-03&format=pdf&version=1.

[2] "Configuration Studies and Recommendations for the ILC Damping Rings," A. Wolski, J. Gao, S. Guiducci (*eds.*), LBNL-59449 (2006), https://wiki.lepp.cornell.edu/ilc/pub/Public/DampingRings/ConfigStudy/DRConfigRecommend.pdf.

[3] J. Urban and G. Dugan, "CESR-c Wiggler Studies in the Context of the International Linear Collider Damping Rings," Proc. of the 2005 PAC, Knoxville, TN, pp. 1880-1882, and references therein.

[4] S. Araki, et al., "Proposal of the Next Incarnation of Accelerator Test Facility at KEK for the International Linear Collider," Proc. of the 2005 PAC, Knoxville, TN, pp. 874-876.

[5] M.A. Palmer, et al., "A Bunch-by-Bunch and Turn-by-Turn Instrumentation Hardware Upgrade for CESR-c," Proc. of the 2005 PAC, Knoxville, Tennessee, pp. 3597-3599.

[6] G.W. Codner, et al., "Diagnostics of Interaction Point Properties and Bunch-by-Bunch Tune Measurements at CESR," AIP Conf. Proc., 868:252-261, 2006.

[7] K. Ohmi, et al., "Study of Coherent Tune Shift Caused by Electron Cloud in Positron Storage Rings," Proc. of the 2nd APAC, Beijing, China, 2001.

[8] M.A. Palmer, et al., "The Proposed Conversion of CESR to an ILC Damping Ring Test Facility," Proc. of EPAC 2006, Edinburgh, Scotland, pp. 891-893.

Traveling Waves Resonant Ring for Electron Cloud Studies

U. Iriso[1], F. Caspers[2], J-M. Laurent[2], and A. Mostacci[3]
[1]CELLS, PO Box 68, 08193 - Bellaterra (Spain)
[2]CERN, CH-1211, Geneva 23 (Switzerland)
[3]Università di Roma "La Sapienza", Rome (Italy)

Abstract

This article is a summary of the work presented in Refs. [1]. In the following, we present the main topics discussed on it. For more information, see the aforementioned article and references therein.

SUMMARY

Within the framework of the CERN program on electron cloud effects in accelerators, a coaxial multipacting test stand was built. In order to simulate bunched beam, the test stand is subjected to short rf pulses. The field strength in a traveling wave mode is sufficient to trigger multipacting in "as received" surfaces, but not in chambers treated to reduce the secondary emission yield.

A number of upgrades in the bench setup have been pursued, mainly in two directions:

- general reduction in mismatching (i.e., electrical losses) amongst the different parts of the setup.
- instead of dumping the pulsed power into a load, it is recirculated by means of a broadband working regime resonant ring.

Reference [1] shows the steps required to build this traveling waves resonant ring: improvements on the chamber and implementation of the coupler.

CONCLUSIONS

The traveling waves resonant ring was finally built through the:

- electrical and mechanical improvements on the setup. The system attenuation was reduced to less than 0.5 dB.
- the "ad-hoc" $\lambda/4$ symmetric 9-sections wideband directional coupler was successfully designed and built. Its coupling factor is measured to be $C \sim 9$ dB, with a reasonably ripple.

The total power enhancement was finnally 9 dB (factor 3 in voltage). This allows for larger multipacting electron energies: from energies of about 75 eV using the original setup, we managed to obtain electron energies of about 200 eV. This allows to trigger multipacting in chambers with low SEY, to study the scrubbing effect, and test surface coatings: for instance the new enamel solutions [2, 3].

REFERENCES

[1] U. Iriso, F. Caspers, J-M. Laurent, and A. Mostacci. *Traveling wave resonant ring for electron cloud studies*, Phys. Rev. ST Accel. Beams 7, 073501 (2004).

[2] P. Hellmold and J. Wendel, *Vitreous enamel - an efficient material component*, in these Proceedings.

[3] F-J. Behler, *Vitreous enamel - foundations, production, applications and CERN tests*, in these Proceedings.

SUMMARY OF THE ECL2 WORKSHOP

F. Caspers and F. Zimmermann, CERN, 1211 Geneva 23, Switzerland
W. Fischer, BNL, Upton, NY11973, USA

Abstract

We summarize the ECL2 workshop on electron cloud clearing, which was held at CERN in early March 2007, and highlight a number of novel ideas for electron-cloud suppression, such as continuous clearing electrodes based on enamel, slotted structures, and electrete inserts.

INTRODUCTION

The ECL2 workshop was held at CERN, 1-2 March, 2007 [1]. It addressed all methods for suppressing the electron build up, such as reducing the primary or secondary electron yields, modifying the electron dynamics, and changing some beam parameters. The workshop did not discuss beam instabilities or beam stabilization in presence of an electron cloud.

The organizers dedicated the workshop to the memory of Francesco Ruggiero (1957-2007), who had been instrumental in setting up and directing the electron cloud research program at CERN.

The workshop was sponsored by the three European accelerator networks CARE-HHH-APD, CARE-ELAN, and EUROTEV-WP3. It was attended by 35 participants from 16 institutions in Europe, Asia, and America, including 3 representatives from the German enamel industry.

The workshop started with a tour of the CERN NEG coating facility, and was structured in eight sessions spanning over the full two days. A primary topic of the ECL2 workshop was the quasi-continuous electron cloud clearing electrode, based on an insulating enamel layer [2, 3]. Further topics discussed were other types of clearing electrodes, NEG coating, grooved surfaces, slotted surfaces, clearing efficiencies, beam measurements, and impedance issues.

MOTIVATION

The main motivation for the ECL2 workshop was the recent realization, which fully crystallized at CARE-HHH LUMI'06 [4], that the electron cloud may constitute a serious limitation for upgraded LHC injectors (namely, for the PS2 and the SPS operated with PS2 beams). The potential problem was revealed in instability and build-up simulations by G. Rumolo and M. Furman, respectively. The actual experience at RHIC [5] and at the present SPS and PS appear to corroborate the predictions. In response to this challenge, an "electron-cloud killer" based on enamel coating was proposed by Fritz Caspers in the fall of 2006, and contacts with German industry were established. An earlier "electron-cloud killer" proposal, which had been put forward by Peter McIntyre for the LHC proper, involved a microscope cover glass insulating layer attached in-situ on the beam screen [6]. In parallel to the LHC upgrade studies, the electron-cloud task force in work package 3 of the EUROTeV linear-collider network is developing solutions against electron cloud build up for ILC and CLIC. A new simulation code, Faktor2, was written for this purpose by Warner Bruns, who, by means of this new code, conceived a different solution for suppressing the electron cloud: a slotted or gridded beam pipe [7].

When comparing the potential of different solutions, a number of aspects need to be considered, such as modeling, prototypes, and beam experiments, suppression efficiency, impedance, vacuum issues, implications and cost. An attempt was made to cover all these points at the ECL2 workshop.

SOLUTIONS

While the installation of continuous clearing electrodes can be challenging in existing machines, they can be an interesting option for new machines with anticipated electron cloud problems, such as the new LHC injectors, or the ILC positron damping ring. Continuous clearing electrodes can be produced by generating an insulating enamel layer on the inside of the beam pipe, above which the electrode is deposited. This electrode can either be made from a low-resistive metal, or it can itself be based on a (now non-insulating but highly resistive) second layer of enamel.

Enamel is a special inorganic glass with a thermal expansion coefficient which can precisely be adapted to its substrate. It may have very high resistance, good adherence to metals, excellent mechanical stability, no electrical charging, very low interaction with organic material, good cleaning properties, and practically no aging. Within bounds, its mechanical and electrical properties can be designed to fit a certain application. Enamel can be applied by dipping, pouring, or spraying. It is dried at 100 °C, and then fired at 850°C. For test purposes, several prototype enamel coated beam pipe sections were produced for CERN by a German company.

The optimum configuration of clearing electrodes was investigated, their impedances for two different layouts estimated by two independent programs, GdfidL [8] and HFSS [9], respectively, and the clearing efficiencies explored in simulations. A traveling-wave resonant ring for testing an enamel chamber equipped with an electrode is

clearing electrode	NEG coating
+ install once	- regular activation needed
- never demonstrated (?)	+ demonstrated in several rings
+ for ions clearing and shaking was helpful	+ good for vacuum
+ efficient for ISR coasting beam	- long-term stability?
- impedance	+ impedance

Table 1: Pros and cons of quasi-continuous electrodes and NEG coating.

presently assembled at CERN. This coaxial multipacting test stand with recirculating pulsed power can model beam-induced multipacting without an actual beam in a controlled laboratory environment [10]. The goal is to demonstrate the mitigating effect of the enamel-based clearing electrode with regard to the electron cloud. Some of the relevant enamel properties, such as SEY and PEY, still need to be measured, but so far no fundamental problem has been found.

Experience with other types of clearing electrodes at operating accelerator is mixed. Clearing electrodes were successfully used for ion and dust clearing in the CERN Antiproton Accumulator and EPA [11]. In the DAΦNE electron ring, the ion clearing electrodes were a significant source of impedance and had to be removed from the ring [12]. Some analytical impedance estimates were presented during the workshop [13]. At the CERN SPS, electron-induced sparking of the electrostatic extraction septum has been observed even with a significant bias voltage [14]. The damper pick ups in the SPS were also affected by electron cloud and subjected to different cures including clearing voltages [15].

The slotted chamber structure is intriguing. Electrons passing through the slots, as well as any secondaries they produce, are shielded from the beam field and do no longer contribute to multipacting. In simulations, the slotted chamber is highly efficient in preventing electron build up. A similar structure is actually installed in ISIS, which may explain why ISIS has never observed any electron cloud effect. A disadvantage of this solution is that it requires additional transverse aperture, so that this structure cannot easily be retrofitted in an existing accelerator with given magnet gaps. For a new machine, however, it is an attractive scheme.

Another novel idea, which was suggested by Fritz Caspers during the workshop, is the use of electretes. These are permanently charged materials, e.g. Teflon subjected to electron bombardment during production. Either they provide a permanent electric field which is sustained over several years, or they are self-charged by the beam field. Electretes might allow for an in-situ upgrade of the LHC and the SPS.

More "classical" techniques, previously proposed for suppressing electron build up, include coating with a thin TiZrV NEG layer [16] or with TiN, and grooved surfaces. Some or all of these techniques are being vigorously tested experimentally with beam at SLAC [17], KEK [18], Cornell [19], ESRF [20], and CERN [21]. Results and further plans from all these studies were presented. The simulated beneficial effect of grooves was also discussed [7,22]. An interesting observation was reported from ANKA at FZ Karlsruhe, where the measured heat load in a cold superconducting in-vacuum undulator and the coincident pressure rise indicate the possible presence of an electron cloud at cold temperature and with an electron beam [23]. Some signals for an electron cloud occurring with an electron beam are also seen at CESR [19].

The discussion session focused on a number of open questions:

- Modeling of the electron cloud: the effect of the beam field on secondary and primary emission, the effect of the magnetic field, and the role of ions; numerous issues related to grooves and their correct modeling; the validity of the assumed surface parameters, e.g. difference in rediffused electron component between copper and stainless-steel surfaces.
- Enamel: its secondary and primary emission yields; impedance; stability; detailed study of suppression efficiency; possibility of fitting the enamel coating in the SPS vacuum chamber;
- Other schemes: air-baked copper, radical injection, permanent electric fields (electretes);
- Grooves: in-situ grooving (for SPS);
- NEG vs TiN: long-term stability; self-activation; heat.

Table 1 compares arguments in favor of, or against, clearing electrodes and NEG coating. Table 2 compiles possible attractive solutions for existing and new storage rings, which emerged from the workshop discussions.

new ring	old ring
slotted chamber	NEG coating
enamel electrodes	in-situ grooves
electrete insert	electrete insert
NEG coating	

Table 2: Possible means of electron-cloud suppression for a new ring (e.g. PS2) and existing accelerator (e.g. SPS).

Not all the ECL2 presentations have been mentioned in detail for this short summary. In addition to the ones discussed above, noteworthy are also the contributions by T. Demma [24], A. Markovik, G. Poplau [25], O. Malyshev [26], G. Rumolo [27], and two further talks by U. Iriso [28, 29], addressing items such as simplified electron-cloud simulations, predictions of electron-instability simulations for an LHC injector upgrade, and the vacuum design of the ILC damping ring.

REFERENCES

[1] Workshop web site http://care-hhh.web.cern.ch/care-hhh/ECL2/

[2] F.-J. Behler et al., "Industrial Enamel — Foundations, Production, Applications, and CERN Tests," ECL2 proceedings.

[3] J. Wendel, P. Hellmold, "Vitreous Enamel - An Efficient Material Compound," presentation at ECL2 workshop.

[4] Workshop web site http://care-hhh.web.cern.ch/CARE-HHH/LUMI-06/

[5] W. Fischer et al., "Electron Cloud Observations and Cures in RHIC," ECL2 proceedings.

[6] P.M. McIntyre, A. Sattarov, Killing the Electron Cloud Effect in the LHC Arcs, Proc. PAC2005 Knoxville, p. 2971 (2005).

[7] W. Bruns, "Simulations of Grooves, Slots and Build Up with Faktor2," ECL2 proceedings.

[8] W. Bruns, "Inpedance of Clearing Electrodes with GdfidL," ECL2 proceedings.

[9] T. Kroyer, F. Caspers, "Impedance of Clearing Electrode with HFSS," ECL2 proceedings.

[10] U. Iriso, F. Caspers, J.-M. Laurent, A, Mostacci, "Traveling Waves Resonant Ring for Electron Cloud Studies," ECL2 proceedings and references threin.

[11] A. Poncet, "Experience with Ion and Dust Clearing in the CERN AA and EPA," ECL2 proceedings.

[12] M. Zobov et al., "Impact of Ion Clearing Electrodes on Beam Dynamics in DAΦNE," ECL2 proceedings.

[13] R. Wanzenberg, "Resistive Wall Wakes and Clearing Electrodes," ECL2 proceedings.

[14] K. Cornelis, "Sparking of SPS Electrostatic Septa in Presence of Electron Cloud," presentation at ECL2 workshop.

[15] W. Hofle, "Clearing Voltages and Solenoids at SPS Damper Pick Ups," presentation at ECL2 workshop.

[16] P. Chiggiato, "NEG Coating," presentation at ECL2 workshop.

[17] M. Pivi, "E-Cloud Suppression for the ILC Damping Ring and Tests in PPE-II," presentation at ECL2 workshop.

[18] Y. Suetsugu, "SEY and Clearing Studies at KEKB," ECL2 proceedings.

[19] M. Palmer, "Electron Cloud Studies at CESR-c and CesrTA," presentation at ECL2 workshop.

[20] T. Perron, "Attempt to Measure the Influence of NEG Coating on Impedance," presentation at ECL2 workshop.

[21] A. Rossi, "Experimental Results with NEG Coating in the SPS," presentation at ECL2 workshop.

[22] M. Venturini, "E-Cloud Build Up in Grooved Chambers," ECL2 proceedings.

[23] S. Casalbuoni et al., "Beam Heat Load in the ANA Superconducting Undulator," ECL2 proceedings.

[24] T. Demma et al., "Maps for Electron Cloud in LHC Dipoles," ECL2 proceedings.

[25] G. Poeplau, A. Markovik, "Simulation Progress and Plans at Rostock/DESY," to be submitted to ECL2 proceedings.

[26] O. Malyshev, "How the Electron Multipacting May Affect the ILC Vacuum Design," presentation at ECL2 workshop.

[27] G. Rumolo. "Electron Cloud Instability in the SPS and SPS+," presentation at ECL2 workshop.

[28] U. Iriso, "Extracting the Electron-Induced Molecular Desorption Coefficient Using an Electron Detector," ECL2 proceedings.

[29] U. Iriso, S. Peggs, "Results Using Coupled Maps for Electron and Ion Clouds in Accelerators," ECL2 proceedings.

List of ECL2 Participants

Behler	Franz-Josef	Eisenwerke F.W. Dueker
Benedetto	Elena	CERN
Bruns	Warner	CERN
Casalbuoni	Sara	FZ Karlsruhe, ANKA
Caspers	Fritz	CERN
Chiggiato	Paolo	CERN
Cimino	Roberto	LNF-INFN
Cornelis	Karel	CERN
Demma	Theo	LNF-INFN
Fischer	Wolfram	BNL
Hellmold	Peter	U. Clausthal-Zellerfeld
Höfle	Wolfgang	CERN
Iriso	Ubaldo	CELLS-ALBA
Jensen	Erk	CERN
Kroyer	Tom	CERN
Mahner	Edgar	CERN
Malyshev	Oleg	ASTeC Daresbury
Markovic	Aleksander	Rostock University
Palmer	Mark	Cornell U., CLASSE
Perron	Thomas	ESRF
Pöplau	Gisela	Rostock University
Rossi	Adriana	CERN
Rossmanith	Robert	FZ Karlsruhe, ANKA
Rumolo	Giovanni	CERN
Schulte	Daniel	CERN
Shaposhnikova	Elena	CERN
Suetsugu	Yusuke	KEK
Taborelli	Mauro	CERN
Tuckmantel	Joachim	CERN
Venturini	Marco	LBNL
Wanzenberg	Rainer	DESY
Wendel	Jörg	Wendel Email
Xia	Guoxing	DESY
Zimmermann	Frank	CERN
Zobov	Mikhail	LNF-INFN